A panchromatic study of the stellar population and dust content of nearby galaxies

Susan Linda Hutton

A thesis submitted for the degree of Doctor of Philosophy (PhD) of University College London

Mullard Space Science Laboratory

Department of Space and Climate Physics

University College London

January 12, 2016

I, Susan Linda Hutton, confirm that the work presented in this thesis is my own. Where information has been derived from other sources, I confirm that this has been indicated in the thesis.

Abstract

This thesis mainly focuses on the dust content in nearby galaxies, whilst also probing the underlying stellar populations. Our main target is the nearby starburst galaxy M82. Five additional nearby galaxies are included in the final chapter. Using NUV and optical photometry, along with FUV, Hα and 8μ data, we explore the radial dependence of the dust properties. We model the dust attenuation law using a prescription that parameterises the total-to-selective extinction ratio (R_V) and NUV bump strength (B). We also include the colour excess as a parameter describing the amount of dust. By comparing with stellar population synthesis models, we show that it is possible to marginalise over nuisance parameters such as the age or metallicity of the populations. We find a significant radial trend of the dust-related properties both in M82 and the other galaxies, although there is a large variance of this trend among them. Remarkably, we find that M82s data does not match the "Calzetti" attenuation law (applied to starburst galaxies). In fact the analysis favours a law with a significant NUV bump. As a function of radius, we find that B and R_V decrease outwards, with a Milky-Way like behaviour in the central region and a steeper (lower R_V) wavelength dependence in the outer regions. We explore this trend in the other five galaxies, finding a large variation in the radial trends from galaxy to galaxy, revealing the complexity of the dust properties.

Acknowledgements

It is a pleasure to thank my supervisor Dr. Ignacio Ferreras to whom I am greatly indebted for his inexhaustible support during my PhD studies. His unwavering teaching and patience has enabled me to complete my studies culminating in this thesis. Thanks to Prof. Kinwah Wu for his support as a second supervisor and also for his challenging questions during panel meetings, also to Dr. Lidia van Driel-Gesztelyi for her support on the panel and her positive words of encouragement. Thanks to the *Swift* team for their enormous help with the UVOT data reduction, Prof. Mat Page, Dr Vladimir Yershov, Dr Alice Breeveld, Dr Martin Still, Dr Paul Kuin and Prof. Mark Cropper. I can not go without thanking the students I have worked alongside for making MSSL a place I looked forward to coming to for so many years. A special mention to Dr Jason Hunt for his help with de-bugging my latex files and Dr Myrto Symeonidis for being a good friend. Finally I need to say a huge thanks to my family. My husband Rob for supporting me when I left a well paid job in London to follow my heart pursuing my PhD, and to my fantastic children Amelia and Samuel who have been so proud of their mum studying the stars. Thanks to my extended family for their patience when I have been short tempered during my years studying and especially during the thesis write-up. I could not have done it without their unquestionable support, thank you!

Contents

List of Figures

List of Tables

Chapter 1

Introduction

1.1 Galaxy Formation

Studying the rate at which stars form in galaxies and how they evolve is key to understanding the evolution of the Universe. By studying galaxies of different ages we can improve our knowledge on how galaxies change over time. To do this we can use detailed observations from all types of galaxies at various stages of evolution. Integrated light measurements from galaxies provide us with a wealth of information about their star formation histories.

If we want to understand in detail the processes that drive star formation in galaxies, it is necessary to achieve enough spatial resolution to resolve pc-scaled regions. It is challenging to follow this approach in distant galaxies because of their comparatively fainter magnitudes, and because of their smaller apparent sizes. For instance, even at the highest spatial resolutions available in optical light (the Hubble Space Telescope) a galaxy at redshift z≈1 is viewed with a resolution measured in physical units of ≈1kpc. For this reason, we focus in this thesis on nearby galax-

ies.

A key question in galaxy evolution is how the formation of stars is regulated. Many aspects of a galaxy's star formation history impacts their morphology such as mergers/interactions with other galaxies and the existence of bars and winds. These play an important part in galaxy evolution and hence star formation. The connection between morphology and properties such as mass and environment reveal the complexity of the processes underlying galaxy formation, including the merger and gas accretion history. It's believed that galaxy structures are made by a mix of mergers with other galaxies and smooth accretion, therefore supporting the long-held view that the Hubble sequence can be understood in terms of these processes and that galaxy morphology changes in the lifetime of a galaxy (Steinmetz & Navarro, 2002).

Mergers are considered important for providing new gas to galaxies as they create tidal interactions that trigger star formation. Indeed evidence for this process is often seen as warps or streams around galaxies, for example around galaxy M82 (NGC 3034, cigar galaxy). M82 has interacted with other galaxies in the the M81 Group (Steinmetz & Navarro, 2002). The HI cloud around M81 and M82 has a disturbed morphology and is dominated by filamentary structures, loops and twists suggesting that they have gone through several close encounters (Yun et al., 1994). The evolution of larger galaxies (e.g. giant ellipticals) is believed to have been due to these types of interactions (Toomre & Toomre, 1972).

As well as mergers, galactic winds (GW) also influence the structure of galaxies therefore impacting the chemical enrichment of galaxies and the intergalactic medium (IGM). Large-scale outflows of gas are believed to be present among active starburst galaxies at all redshifts (Lehnert & Heckman, 1996). Winds are now routinely incorporated into theoretical models of galaxy evolution, however there is much about the underlying physics that is still poorly understood. As M82 appears edge-on its GW can be clearly seen. See Fig.1.1 of the nearby M82 starburst galaxy showing the GW protruding above and below the galaxy.

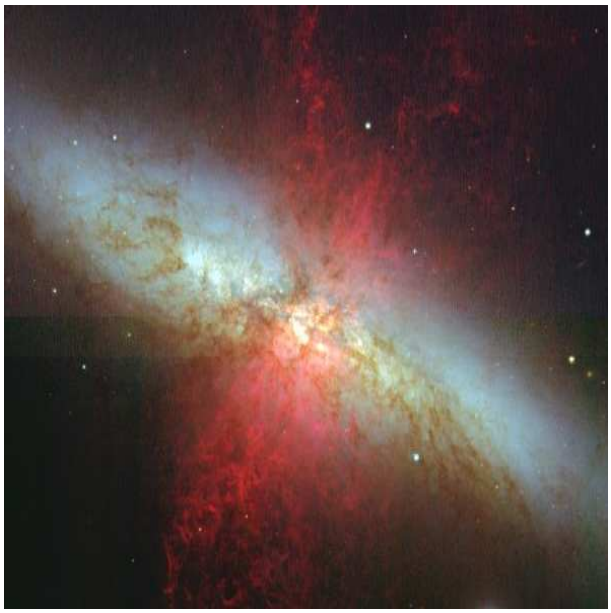

Figure 1.1: Image from FOCAS, Subaru 8.3m telescope, NAOJ of M82. Notice the prominent galactic wind, as seen in the ionised hydrogen gas (red). The filaments extend for over 11kpc above the disc (Lehnert et al., 1999).

1.2 Super-winds and Feedback

Starburst driven GWs originate from the intense stellar radiation (radiation pressure) and SNe shock waves that exist in star forming regions. Bursty rather than continuous star formation history (SFH) is most likely the progenitor (Tremonti et al., 2004). GWs remove gas from the disk and halo and therefore is believed to be one of the dominant mechanisms for regulating star formation especially in lower mass galaxies (Tremonti et al., 2004). These winds are believed to suppress star formation (SF) locally and trigger it on a larger scale helping to dispose of newly made metals into the interstellar medium (ISM) (Heckman et al., 1990). As well as removing gas, GWs are believed to also send energy and momentum into the ISM to form a negative stellar feedback.

The central question of what powers a galactic wind dates back 40 years to the discovery of the wind in M82 (Lynds & Sandage, 1963). Stellar winds are dominated by SNe explosions by the time they turn into GWs therefore only appearing in galaxies that produce lots of high mass stars i.e. $M>10M_{\odot}$. We still do not know what happens to the GW material, if it escapes the galaxy or rains back down and whether there is a mass limit for a galaxy to produce a GW (Tremonti et al., 2004; Strickland et al., 2004). Radiative feedback is also an important form of feedback in galaxies but even here outflows are likely to play a key role in clearing a path for the escaping radiation (Veilleux et al., 2005).

1.3 Metallicity

Metallicity Z is defined as the mass ratio of all matter made up of chemical elements other than hydrogen and helium "Heavy Elements". It's usual to define metallicity as Fe or O abundances or by the amount of metals locked in the stars or the gas. Solar metallicity $Z_{\odot}$=0.02. SNe explosions originate from massive stars and they disperse their materials throughout the universe to be incorporated into the later generations of stars that are observed today. Therefore older stars tend to have lower metallicities than younger stars such as our Sun, although this is dependent on the star formation history of the star forming region. For instance elliptical galaxies have a dominant population of old, metal-rich stars (e.g. de La Rosa et al., 2011).

In a simplified way, the process of galaxy formation involves a gradual transformation from gas into stars. As cosmic time evolves, the amount of gas gradually decreases as more stars are being formed (cosmic star formation history Madau et al. 1998). We can therefore use this fraction to help us quantify the degree of evolution of a galaxy. A tight correlation has been found between stellar mass and metallicity hence showing that the mass of a galaxy also plays an important part in the chemical evolution of a galaxy. However the origins of the mass-metallicity correlation are still ambiguous (Tremonti et al., 2004).

Metal-rich GW outflows will effectively lower the Z of the galaxy and decrease the gas to stellar mass fraction. If we believe in the GW also escaping the potential well then this outflow will increase the IGM (Inter galactic medium) with heavy

elements. So it's clear that galaxy evolution is not simply a closed box (Tremonti et al., 2004). Therefore metallicity helps us to understand how much gas is being exchanged between the galaxy and the IGM and also how much the stars are re-processing. Knowing this relationship will move us closer to understanding galaxy evolution.

1.4 UV and Optical stellar light

As we are not able to obtain resolved star images for most nearby galaxies then we must rely on integrated light measurements to do our studies. The UV and optical spectrum of a nearby galaxy can be used as a probe of its past star formation history and its metallicity at different times (fossil record). The UV light we see from galaxies is affected by dust (see next section) and so this light needs to be disentangled from the scattering and absorption effects of the dust before we can use it to estimate the stellar population ages and their metal content.

Hot O type and early B type stars are hot enough to emit ionising ultraviolet continuum and the later type B stars emit in the non ionising ultraviolet continuum. Therefore high mass stars dominate UV luminosity and this UV light is visible if it is not shrouded in dust. Therefore UV light is a good monitor of moderate to strong SFRs and is also useful to observe high redshift galaxies as UV is shifted into the optical. UV is however sensitive to the initial mass function (IMF see Kroupa 2001) which is important if it is used in modelling stellar populations. Other sources in a galaxy also emit UV light such as white dwarfs and evolved horizontal branch

stars, but for those late type galaxies such as M82 we can assume that the UV light will be dominated by the OB stars because of its strong star formation rate and in the case of white dwarfs, the age of the galaxies are too young for white dwarfs to have had time to develop in enough numbers.

1.5 Dust

1.5.1 The Effects of Dust

Understanding the effect of dust on the light from galaxies not only helps our understanding of stellar formation but also other aspects of galaxy evolution such as the relationship between star formation and AGN (active galactic nuclei). Dust forms during stellar evolution processes and it can also be made directly in the ISM. Dust is prevalent in molecular clouds and it's here where these grains will be included in the chemistry and synthesis of more complex molecules. As these clouds collapse to form stars, these molecules are dispersed into the ISM. At the end of the stars life they expand and die (and some eventually explode as a SNe) and the stars material (with a higher metallicity) is once again emitted into the ISM and so the cycle starts again. Hence for the ISM to be replenished with metals, stars need to be born (and hence die).

In preference to longer wavelengths UV light is scattered or absorbed (and re-radiated in the far infrared) by dust and how light is scattered depends on the ratio between the wavelength and the size of the scattering particles. Light in our atmosphere scatters at $\approx\lambda^{-4}$ (Rayleigh scattering). Rayleigh scattering is the elastic

scattering of electromagnetic radiation by particles that are much smaller than the wavelength of the radiation (Strutt, 1871).

As active star forming regions emit most of their light in UV, this light will be attenuated by the dust in the galaxy (and in line of sight of our MW). As dust absorbs UV light and subsequently heats up and re-emits in the FIR. The UV light not obscured by dust will be invisible in FIR. Hence, the net energy output from star formation is shared between the FIR light from dust absorption and the NUV from un-attenuated light. We can also use spectral features caused by the dust to understand the type of dust and hence how it was formed. For example silicate dust such as the feature around 10μm is prominent in more luminous stars and with later spectral type (Humphreys et al., 1972).

1.5.2 Dust Modelling

Light is affected (attenuated) by dust depending on its wavelength, so when we correct for dust we need to take the wavelength into account. Below shows two different forms of the standard dust law. We use these to calculate the increase in flux when the effects of the dust is removed. The $k(\lambda)$ function is specific to the dust model adopted.

$$F_o(\lambda) = F_i(\lambda)10^{-0.4E_s(B-V)k(\lambda)} \tag{1.1}$$

$$F_o(\lambda) = F_i(\lambda)10^{-0.4A(\lambda)} \tag{1.2}$$

$F_o(\lambda)$ and $F_i(\lambda)$ are the dust-obscured and intrinsic stellar flux densities respectively. $A(\lambda)$ is the dust obscuration, E_s(B-V) is the colour excess of the stellar continuum and $k(\lambda)$ is the dust extinction. Using equation 1.1 we vary $k(\lambda)$ depending on which dust model is to be used such as "Calzetti" (Calzetti, 2001a), "Fitzpatrick" (Fitzpatrick, 1999a) or "Conroy" (Conroy et al., 2010a) models. The "Calzetti" model is known as a starburst model and shows a smooth attenuation curve following a set of power laws and the "Fitzpatrick" model is used for Milky Way (MW) type galaxies and has a resonant feature at 2175$\mathring{A}$. Comparison of these two dust laws can be seen in Fig.1.2.

This UV dust "bump" was first observed by Stecher (1965) where they looked at the magnitude difference between two stars in the MW to calculate the interstellar extinction. This bump is strong in sight-lines probing the ISM of the MW galaxy. One such explanation of the "bump" by Bradley et al. (2005) suggests that the carriers are organic carbon and amorphous silicates that are very common in the interstellar medium.

For equation 1.2 the extinction curves are often measured using R_V which is defined as the ratio of total to selective extinction in the V band. Hence R_V = A(V)/E(B-V) and measures the total A(V) to selective E(B-V). E(B-V) = A(B)-A(V) and A(B) and A(V) are the total extinction at the B and V filter bands. In the diffuse interstellar medium of our MW R_V has been measured between 2.2 and 5.8 depending on line of sight but the average value of 3.1 is usually used (Schultz & Wiemer, 1975). The observed range of R_V is due to the large variation in the

steepness of the extinction curve in the optical region. It's also known to be correlated with the average size of the dust grains causing the extinction (Draine, 2011).

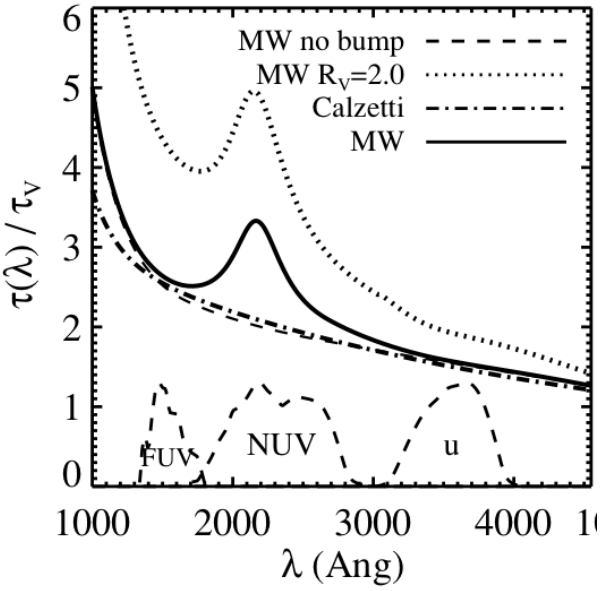

Figure 1.2: (Conroy et al., 2010b) UV attenuation curves normalised in the V band. The 'Fitzpatrick' MW curve with R_V =3.1 and B=1 (solid line) and without the UV bump B=0 (dashed line) are shown. They are compared to the 'Calzetti' starburst curve B=0 (dash-dotted line) and also a MW curve with R_V=2.0 (dotted line). The transmission curves for the FUV, NUV, and u-band filters are also shown in the bottom panel.

When investigating the effects of dust on the light we see from nearby galaxies we need to take into account that the redder light might either originate in the dust-reddened young massive stars or in the lower mass (typically older and cooler) stars. How do we distinguish between the two and account for this degeneracy? When investigating the amount of dust reddening FIR we can look at the "infra-red excess" by finding the ratio of TIR(total Infrared)/UV flux. This ratio is a good indicator of UV dust attenuation in a galaxy as it is the total UV light absorbed

and re-radiated by the dust in the infrared compared to the total UV stellar light observed (Lee et al., 2009).

1.6 Indicators of Star Formation (SF)

We can measure star formation by relying on direct measurements such as FIR or UV light. We can also use Radio luminosity as this results from synchrotron emission associated with SNe (see below). As massive stars emit flux that has enough energy to ionise the medium around it, we can also use recombination lines, such as Hα line emission as a SF indicator. However SFR calculations depend on the indicators used, for example UV tracks moderate SFR and FIR tracks moderate to high SFR. If we track high mass stars as these stars are short-lived we will be measuring recent star formation activity, but we can not forget the low mass stars though as they do dominate the mass of galaxies.

1.6.1 Radio

Radio waves can penetrate large clouds of interstellar cosmic dust which are opague to other forms of light. Radio waves can be created in the following ways;

1. Ionising photons from newly formed massive stars that dominate the HII regions (Kobulnicky & Johnson, 1999) ionise these regions to produce free-free emission. However this form of radio wave is weak and we have to rely on being able to resolve HII clouds, so we can only use it with the Milky Way and nearby galaxies.

2. Synchrotron radiation (radio emitting plasma) mainly from cosmic rays is produced in SNe shocks and this radiation diffuses into the galaxy. The lifetime of this emission is much shorter than the age of the older stars and so is relatively

uncontaminated by the light from these older stars. Synchroton radiation also has the advantage of being extinction free. Although this emission has an indirect link with SFR we may not be able to calibrate it directly due to uncertainties in SNe remnants and cosmic ray production. However it has been shown to be well correlated with other SFR indicators (Bell, 2003).

1.6.2 Infrared

As we know dust absorbs UV from hot new stars very efficiently and re-radiates in FIR, hence very luminous galaxies in the IR often have high star formation rates. Other processes can also heat up dust such as active galactic nuclei (AGN), however studies show that galaxies with AGN need starburst to account fully for their FIR emission (Hatziminaoglou et al., 2010). Cirrus λ=100μm is formed when dust is warmed by normal optical starlight, therefore this normally only dominates in early type galaxies. So FIR can be used as a good star formation rate indicator for late type starburst galaxies without AGN.

1.6.3 Hα

We use Hα to identify where very recent star formation has taken place in M82. Only ionising photons come from the most massive O and early type B stars (M>17M$_\odot$) which are young (only a few hundred million years old) and as this type of star has a very short lifetime, Hα is a good indicator of very recent star formation. This star formation ionises hydrogen atomic gas which exists in the inter galactic medium (IGM) and when the electron recombines with the ion the bright emission line (6563Å) is formed. However caution must be applied as not all the photons emitted from these stars will be ionising and we may be understating

the SFR as also some of these ionising photons will have leaked into the ISM or been absorbed by dust.

We can use Hα/UV as a time clock for nearby galaxies as we know that Hα traces stars that live for a few million years and UV traces stars over longer timescales $>10^8$ years. Once ionising stars are finished in galaxies the luminosity decreases and non ionising stars become dominant i.e.UV becomes dominant, so Hα/UV decreases. We can use this ratio to show how much stronger Hα is to UV revealing a recent change in the star formation rate. For example if Hα/UV>10 (Lee et al., 2009) it could indicate a very strong starburst episode.

When calculating Hα (and UV) luminosity, most studies assume a constant conversion factor using the equations below.

$$SFR(M_{\odot}yr^{-1}) = 7.9 \times 10^{-42} L(H\alpha)(ergs\, s^{-1}) = 1.08 \times 10^{-53} Q(H^0)(s^{-1}) \quad (1.3)$$

$$SFR(M_{\odot}yr^{-1}) = 1.4 \times 10^{-28} L_{uv}(ergs\, s^{-1} Hz^{-1}) \quad (1.4)$$

There are consistencies with these two SFRs when dust attenuation corrections have been applied. The conversion factors below are calculated using a Salpeter IMF (Salpeter, 1955) with mass limits from 0.1 to 100 $M_{\odot}$. The luminosities used in the equations above are calculated by multiplying the flux density F by a surface area $\pi\times$ d^2 $\times$ 4 where d(cm) is the distance to the galaxies. Q(H^0) is the ionising

photon luminosity and L_{uv} is UV luminosity. The SFR is then calculated using equations 1.3 and 1.4 (Kennicutt, 1998a). Metal poor stars produce more ionising flux so will have a greater Hα/FUV, however this effect is found to be negligible (Lee et al., 2009).

Other recombination lines can be used as star formation indicators such as the Brackett line (Brγ) as this traces hot and cold dust. This emission line will exist whilst bursts are happening but then after the starburst has finished FIR is the better SFR indicator as heated dust by longer lived stars dominate over emission lines.

1.7 Star Forming Regions

1.7.1 The Birth of HI and HII Regions

In the highest density regions of the interstellar medium (ISM) atomic hydrogen HI is transformed into H_2 (molecular hydrogen) under certain density and temperature conditions e.g. protected from UV radiation by dust. This giant molecular cloud (GMC) (containing H_2 gas) cools and the subsequent shock waves can then cause the cloud to collapse and upon the collapse stars are born. Therefore HI and H_2 can be indirect indicators of current star formation and also used to calculate SFRs.

The most massive stars in these GMCs will reach temperatures hot enough to ionise its surrounding gas and soon after the formation of this ionising radiation field, energetic photons create an ionisation front which sweeps through the surrounding gas at supersonic speeds. Eventually, the ionisation front slows to subsonic

speeds and so the shock front overtakes it, this is how the HII region is formed. Hence the HII region is a large, low-density cloud of partially ionised gas in which star formation has recently taken place. The distribution of gas and stars in HII regions is inhomogeneous and so it often appears clumpy and filamentary and may give birth to thousands of stars over several million years. Therefore the study of extragalactic HII regions is important in determining the chemical composition and hence the future star formation of galaxies.

The lifetime of a HII region is of the order of a few million years as the stars that ionise the hydrogen are short lived and the radiation pressure from the hot young stars and SNe eventually drive most of the gas away. Indeed this whole process tends to be very inefficient and less than 10% of the fraction of total interstellar mass is usually burned in 10^8yrs. Spiral and irregular galaxies contain a lot of these regions, while elliptical galaxies are almost devoid of them. In the spiral galaxies, including the Milky Way, HII regions are concentrated in the spiral arms, while in the irregular galaxies they are homogeneously distributed. Some galaxies contain huge HII regions, which may contain tens of thousands of stars.

1.7.2 Tracers of HI and HII regions

As well as using star formation indicators we can also use tracers of the star forming regions to estimate ongoing star formation rates. For example atomic and molecular hydrogen gas regions are the early breeding grounds of stars and so we can use these regions to detect star formation.

Most of the hydrogen in the ISM (far from hot O and B-type stars) is in the atomic form (HI). The 21cm (λ=21.1cm frequency=1420.4MHz) hydrogen emission line is a good tracer of HI regions. This line is emitted when the electron in the H atom changes its spin from parallel to anti-parallel spin against the proton spin (lowest energy state). The intensity of the line depends on the density of the HI along the line of sight and so is a good indicator of potential star formation. It is found that it is only in the regions of the outer galaxy where the SF scales with HI emission (Bigiel et al., 2011).

H_2 is an unusual molecule as there is no dipole because of its symmetry and so no light is absorbed or emitted hence it's mostly invisible.

As we can't see molecular hydrogen directly we can trace it by CO which is detected at λ=1.3mm & 2.6mm (radio band) and is abundant in regions with a high density of molecular hydrogen. More metallicity means a greater amount of CO molecules. Therefore an increase in metallicity would increase the CO line emission as this emission is caused by H_2 molecules colliding with CO molecules so more CO the more intense the emission line will be. However, there are challenges when using CO line emission as it's difficult to convert CO to reflect the amount of H_2 and also it's difficult to detect H_2 clouds outside of the Local Group (Bigiel et al., 2011).

1.8 Star Formation Efficiency (Schmidt Law)

Schmidt proposed that the star formation rate (SFR) should be proportional to the gas density in galaxies. He suggested a simple power law see eq.1.5 (Schmidt, 1959),

$$\sum {}_{SFR} = A \sum {}^{N}_{gas} \tag{1.5}$$

where $\sum_{SFR}$ and $\sum_{gas}^{N}$ are the observable surface densities of star formation and gas respectively.

This relationship was observed in a large number of starburst and normal galaxies (Kennicutt, 1998b), see Fig.1.3 for the "Kennicutt-Schmidt Law" with N=1.4. However a larger range of N (N=1 to 2) has been found in other studies. For example Bigiel et al. (2008) investigates how this Schmidt law varies between the H_2 dominated centres of spiral galaxies, their HI dominated outskirts and rich late-type/dwarf galaxies. They find that N = 1.0 $\pm$ 0.2 across their sample of spiral galaxies and that H_2 forms stars at a constant efficiency in spirals. This is different to Kennicutt (1998a) findings and one reason Bigiel et al. (2008) give for these different values of N is that starburst galaxies have average surface densities far in excess of a galactic GMC and therefore the value of N will depend on the sample population.

We know that galaxy morphology and hence Hubble classification affects SFR. It is clearly important to understand the reasons for the huge range in SFRs and why there seems to be a correlation amongst galaxies. Fig.1.3 shows SFR vs gas for

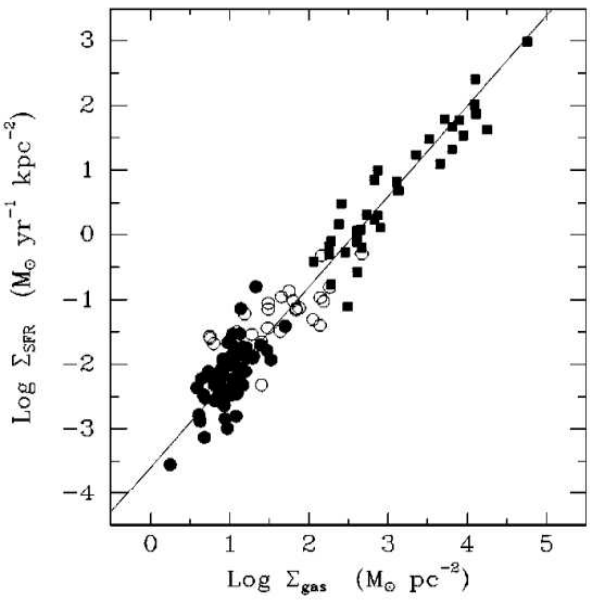

Figure 1.3: (Kennicutt, 1998b) The global Schmidt law in galaxies. Solid points denote normal spirals and squares denote circumnuclear starbursts. The open circles show the SFRs and gas densities of the central regions of the normal disks. You can see there is a clear trend for the SFR to increase with density.

normal galaxy disks over a range of Hubble types. As you can see the "Kennicutt-Schmidt" law holds as there is a clear trend for SFR to increase with surface gas density.

- Spiral Arms

In spiral galaxies the SFRs seen in the centre are largely decoupled from the SFRs seen in the disks and are thought to be influenced mainly by gas inflow into the circum-nuclear regions. The biggest variance in SFR was found in grand-design spirals where there were large patchy increases in star formation found in the spiral arms. However overall the SFR in spiral galaxies remains constant and it is thought to be due to spiral density waves (Kennicutt, 1998a) that constantly change which

stars, dust and gas make up the spiral arms.

- Bars

It has been found that the presence of a bar does not affect the large scale SF in the disc, see Fig.1.4. The vertical left axis shows the amount of recent star formation as per line emissions and the right vertical axis shows the corresponding SFRs. The horizontal axis shows the types of galaxies and as you can see there is no discernible pattern between the barred or normal categorisation.

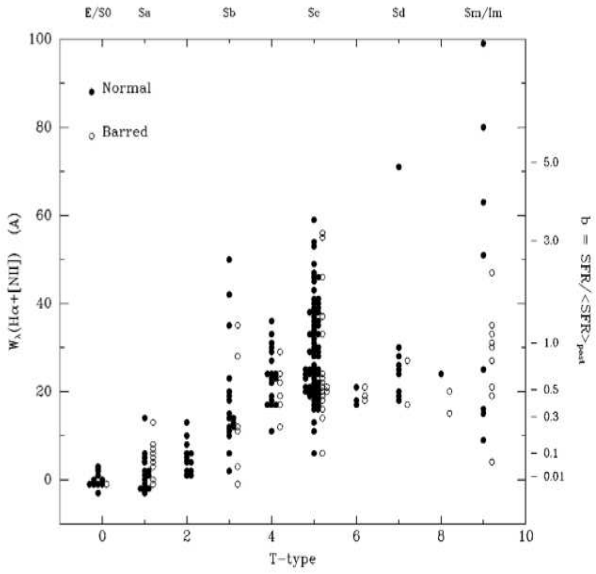

Figure 1.4: (Kennicutt, 1998a) Distribution of integrated Hα + [NII] emission-line equivalent widths for a large sample of nearby spiral galaxies, subdivided by Hubble type and bar morphology. The right axis scale shows corresponding values of the stellar birthrate parameter b, which is the ratio of the present SFR to that averaged over the past

- Tidal Interaction

Not surprisingly tidal interactions do impact SFR a lot compared to other internal disc structures as recent Hα and FIR studies have shown e.g. M82. The extent

at which SFR is affected depends on how gas rich the galaxy is. For example tidal interactions in gas poor galaxies do not enhance their SFR at all but gas rich galaxies can have their SFR enhanced between 10 - 100 times in extreme cases (Kennicutt, 1998a).

1.9 Constraining Stellar Populations in Nearby Galaxies

The star formation history of galaxies is imprinted in their integrated light. To interpret the light emitted from galaxies in terms of their stellar content we need to use the evolutionary population synthesis technique taking into account dust attenuation. So in order to constrain mass, age and metallicity in a nearby galaxy we need to use a model that evaluates the stellar evolutionary tracks of these variables. This stellar population synthesis (SPS) technique combines these evolutionary models with atmospheric models and spectral libraries. We use simple stellar populations (SSPs) such as Bruzual & Charlot 2003 (Bruzual & Charlot, 2003) and *Pickles* library (Pickles, 1998) (which is a library of over a hundred flux-calibrated spectra of all types of stars e.g. metal rich and with different masses). The SPS model maps a range of ages and metallicities using dust laws with varying SFHs (such as exponential decay and two burst models), with adjustable parameters SFR and chemical composition.

Once we have chosen a model we can then use χ^2-based analysis to find the best fit values of dust, age, metallicity and dust law with their galaxy photometry. From this, probability distributions and confidence limits can be calculated to see if these parameters can be constrained.

Fig.1.5 shows a NUV colour-colour diagram comparing the observations (black dot) with predictions from the SPS models of Bruzual & Charlot 2003 and Starburst99. SSP model showing all range of ages, metallicities and colour excess.

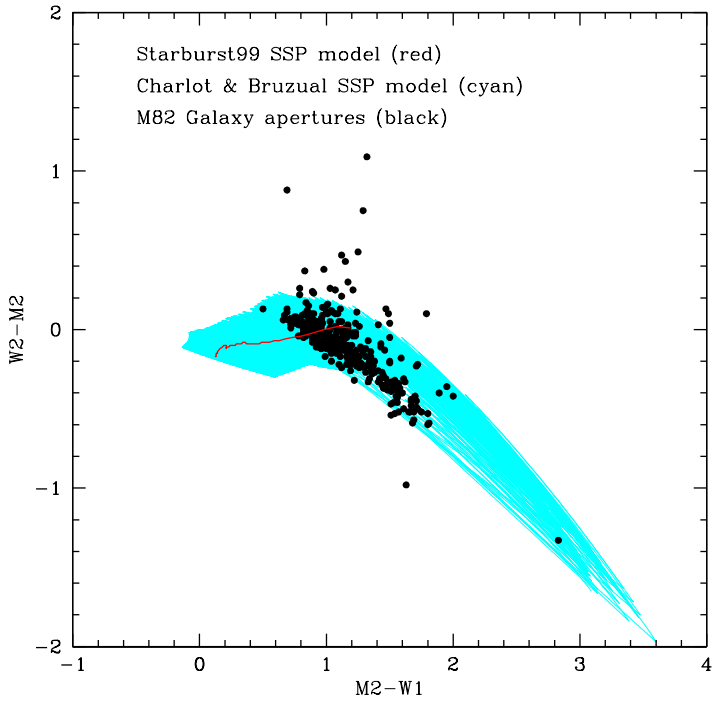

Figure 1.5: A UV colour plot showing an SSP (red) with a range of ages but one metallicity and a Bruzual & Charlot 2003 SSP model (blue) with galaxy (M82) photometry colours (black solid circles) for reference.

Several authors (Rieke et al., 1993; Doane & Mathews, 1993) have applied evolutionary synthesis modelling to understand the nature and evolution of starburst activity in nearby galaxies such as M82. However despite extensive studies crucial issues remain open such as the composition of the stellar populations and their spatial variations and what the initial mass function is of the stars formed in the

starburst, and also how the starburst evolved.

1.10 Galaxies Studied in this Thesis

1.10.1 M82 (NGC3034, Cigar Galaxy)

Figure 1.6: http://www.spacetelescope.org. To celebrate the Hubble Space Telescope's 16 years of success, the two space agencies involved in the project, NASA and the European Space Agency (ESA), released this image of M82.

Studying nearby starburst galaxies with galactic winds which have also had recent interactions with other galaxies provides an opportunity for us to improve our understanding of galaxy evolution. M82 is one such galaxy and is interesting to study in all areas of the electromagnetic spectrum. M82 is dominated by filamentary structures loops and twists suggesting that it may have gone through several close encounters with its neighbour M81 (Yun et al., 1994). Its recent interaction with M81 is evident by the filamentary dust streams joining it up with the other

galaxies in the M81 group. These interactions have caused M82's star formation to increase 10 fold to $10M_{\odot}$/yr. In infrared light M82 is the brightest in the sky and has an AB mag of 9.30[1] and exhibits a so-called infrared excess. It's also bright in the optical and UV. M82 appears as an edge on galaxy and the wind profile is clearly seen in Fig.1.6. Evidence indicates that the gas in the wind is being driven out by the combined emerging particle winds of many stars, together creating a galactic superwind (Heckman et al., 1990). It is located at a distance of 3.5 Mpc (Dalcanton et al., 2009) and has a dynamical mass of $\sim 10^{10}M_{\odot}$ (Greco et al., 2012).

1.10.2 M81 (NGC3031, Bodes Galaxy)

Figure 1.7: http://www.spacetelescope.org. This NASA/ESA Hubble Space Telescope image of M81was released in September 2014.

M81 has an AB magnitude of 7.89 mag and a distance of 3.71 Mpc and can be

[1]https://ned.ipac.caltech.edu

seen on rare occasions with the naked eye. It's the largest galaxy of the M81 group which means that during its recent interaction with M82 the tidal effects dominated M82. However you can see M81's spiral pattern was left more pronounced and there is also a dark linear feature in the lower left of the nuclear region.

1.10.3 M51 (NGC 5194, Whirlpool galaxy)

Figure 1.8: http://www.spacetelescope.org. This image of M51, taken in January 2005 with the Advanced Camera for Surveys aboard the NASA/ESA Hubble Space Telescope.

M51 is also known as the "Whirlpool" galaxy and is a grand design spiral with an active galactic nuclei (AGN) and black hole at its centre. It can be seen through binoculars in dark conditions as its AB mag is 8.6mag and its' distance is 7.845 Mpc. Overall the galaxy is about 1/3 size of the Milky Way. There is a dwarf galaxy (M51b) that can be seen to be interacting with M51 and its HII regions are visible in the spirals.

1.10.4 M100 (NGC 4321)

Figure 1.9: http://www.spacetelescope.org. This image shows the core of M100 as imaged by Hubble Space Telescope's Wide Field Planetary Camera 2 in its high resolution channel.

M100 is a grand design spiral galaxy and is in the Virgo cluster. Its face on orientation allows us to see its two spiral arms clearly. Its arms are very blue in colour implying they contain hot young stars. Its distance is 16.568 Mpc and AB mag is 9.84mag.

1.10.5 M101 (NGC 5457)

M101 is known as the "Pinwheel" galaxy and is a face on spiral. It is considered a large galaxy and is comparable in size to the Milky Way. It's known for its very large and bright HII regions. It is asymmetrical due to interactions with its companion galaxies. Its distance is 6.81 Mpc and AB mag is 8.31mag.

Figure 1.10: http://www.spacetelescope.org. This image of M101 is the largest and most detailed photo of a spiral galaxy ever taken with Hubble.

1.10.6 M77 (NGC 1068)

Figure 1.11: http://www.spacetelescope.org. The NASA/ESA Hubble Space Telescope captured this vivid image of spiral galaxy Messier 77.

M77 is a spiral galaxy and has a bright active galactic nuclei (AGN) in its centre. It's a type of Seyfert galaxy. It's at the same distance as the Virgo supercluster but it's in the opposite direction. Its distance is 12.65 Mpc and AB mag is 9.61mag.

Chapter 2

Data Reduction & Colour Analysis

2.1 Introduction

In this thesis we use FUV, NUV, optical, 8μm and Hα photometry to interpret the integrated light we see from M82 and we use just NUV and optical for the other galaxies. Massive hot new stars emit predominantly in UV and older cooler stars emit in optical. Hα is a sensitive indicator to ongoing star formation and 8μm maps the hot dust near the stars.

We take our near Ultraviolet (NUV) images from the Ultraviolet/Optical Telescope (UVOT) (Roming et al., 2005) onboard the *Swift* spacecraft (Gehrels & Swift, 2004) for our purposes of targeting the dust properties of nearby galaxies. The images are retrieved from the HEASARC/*swift* publicly available catalogue. UVOT has an optimal set of three broadband filters in the NUV, straddling the 2175$\mathring{A}$ bump (Poole et al., 2008). This 2175$\mathring{A}$ feature was first observed in the 1960s but its origin is still not fully understood. Several models have been presented to account for this bump, such as graphite grains with a mixture of PAH (poly-

aromatic-hydrocarbons) molecules.

Our optical passbands are from the Eigth Data Release (DR8) of the Sloan Digital Sky Survey (SDSS) (Aihara et al., 2011) and 8μm and Hα are from the 5th data release of the Spitzer Infrared Nearby Galaxies Survey (SINGS, Kennicutt et al., 2003). The FUV images were retrieved from the Galaxy Evolution Explorer (GALEX) via the "Atlas of Nearby Galaxies Survey" (Gil de Paz et al., 2007).

Telescopes based in space do not have the effects of atmospheric distortion to deal with (why stars seem to twinkle). Furthermore the atmosphere absorbs a lot of UV and so some UV light never reaches ground-based telescopes, hence we need to observe UV in the upper atmosphere or from space. There are several space based UV telescopes that are no longer active including the International Ultraviolet Explorer (IUE) and GALEX that were terminated in 1996 and 2013 respectively. We use the FUV data from GALEX to enhance our UV analysis for M82. As well at *Swift* there is only the Hubble Space Telescope in space that currently monitors galaxies in the UV, however the XMM-Optical Monitor is also still active and provides coverage in the optical (U, B, V) and NUV bands. The XMM-OM is very similar in design to *Swift* UVOT.

In order for us to gain a good understanding of UVOTs processes we compare the reduction techniques using IRAF software and also UVOT dedicated software. We found that there isn't much difference between the two approaches we use to obtain the final co-added images and so we decide to use the UVOT software as we

need to use this software to subsequently reduce our images.

We then calculate the magnitudes for each image and filter taking into account the calibration of the different instruments, the Milky Way (MW) Galactic Extinction and the diffuse galactic background effects. From these magnitudes we calculate the colours needed for our stellar population synthesis modelling.

This chapter is made up as follows: In this section we provide an introduction to the chapter and in §2.2 we describe UVOT. In §2.3 we discuss the UVOT reduction process we adopted. In §2.4 we introduce the galaxies in our survey. In §2.5 we describe the photometry we use in addition to the UV. §2.6 shows how we reduced our images. The next section shows further reduction steps we adopted (§2.7). We then calculate our magnitudes (§2.8) and finally calculate the galaxy colours (§2.9).

2.2 The UVOT Instrument

We use the NUV images from the Ultraviolet/Optical Telescope (UVOT) (Roming et al., 2005) that is onboard the *Swift* spacecraft (Gehrels & Swift, 2004) which was launched in November 2004. UVOT was designed and built at MSSL/UCL and the design is based on the XMM-Optical Monitor (OM) which is onboard the ESA XMM mission. *Swift* was designed to locate and then rapidly slew to position to observe Gamma Ray Bursts (GRB) and when it is not observing GRBs it continues to capture data from a proposals-based programme.

UVOT uses a 11 position filter wheel which includes UV and optical broadband filters with wavelength range 1600-6000 Å. It is a Ritchey-Chrétien telescope with a 30cm aperture, providing a 17 × 17 arcmin^2 field of view.

There is a photocathode that converts incoming photons to electrons and then the electrons are accelerated before they are captured, this allows the signal to be intensified. This "photon counting" technique enables the position and the time of the photon to be recorded and can detect very low photon counts up to a magnitude of 24[1]. UVOTs photon counting detectors are unlike typical optical telescopes because instead of transforming a photon flux into a charge (as in CCDs), they count photons individually, therefore, such an instrument is more sensitive than any other type.

The three UV galaxy imaging telescopes – UVOT *Swift*, Hubble Space Telescope (HST) and GALEX – have NUV wavebands that have a similar wavelength coverage but there are differences in their FOV (field of view), PSF (point spread function) and sensitivity. UVOTs FOV of 17' x 17' is larger than HSTs, hence a single pointing can map nearby galaxies. UVOT sampling is 2048 × 2048 pixels. Its pixel size of 0.5 arcsec also provides good spatial resolution (e.g. 50 pc at the position of M82) of star forming regions within our local galaxies. The resolution (PSF) of UVOT is between 2.4 and 2.9 arcsec (full width half maximum FWHM) in the NUV filters (Breeveld et al., 2010) which is smaller than GALEX FUV resolution and so is also better for our stellar population analysis. UVOT being space-based

[1]https://www.swift.psu.edu/uvot/

rather than ground-based, benefits from no atmospheric extinction and background noise and with its optimally placed set of three NUV broadband filters it is an ideal instrument for the analysis of dust in nearby galaxies. Fig.2.1 shows the UVOT passbands from the three NUV filters UVW2, UVM2 and UVW1 illustrating how the NUV bandpasses straddle the 2175$\mathring{A}$ dust bump.

2.3 UVOT Data Reduction

Onboard UVOT, NUV data are taken in 3 modes, Image mode, Event mode and Image & Event mode[2]. The "Image" observations are binned in 2 × 2 pixel binning whereas the GRB "Event" modes are always 1 × 1 binning. The 2 × 2 binning is used in order to reduce the telemetry required from UVOT for non GRB observations and effectively puts 4 pixels into 1 in the final image. Therefore when UVOT is not reacting to a GRB in "event" mode it is taking photometry of the sky in "image" mode. UVOT reduces the image/event extensions into a smaller number of files. Before summing the images using the UVOT software they are aspect corrected automatically by the instrument before archiving. Equatorial coordinates were applied to each exposure and these exposures were then rotated so that north is up and east to the left.

UVOT Data Corrections: Before calculating the magnitudes using the flux obtained from our photometry we need to apply the corrections below to our UVOT data. Some are standard telescopic corrections but others are because UVOT is a

[2]https://www.swift.psu.edu/uvot/

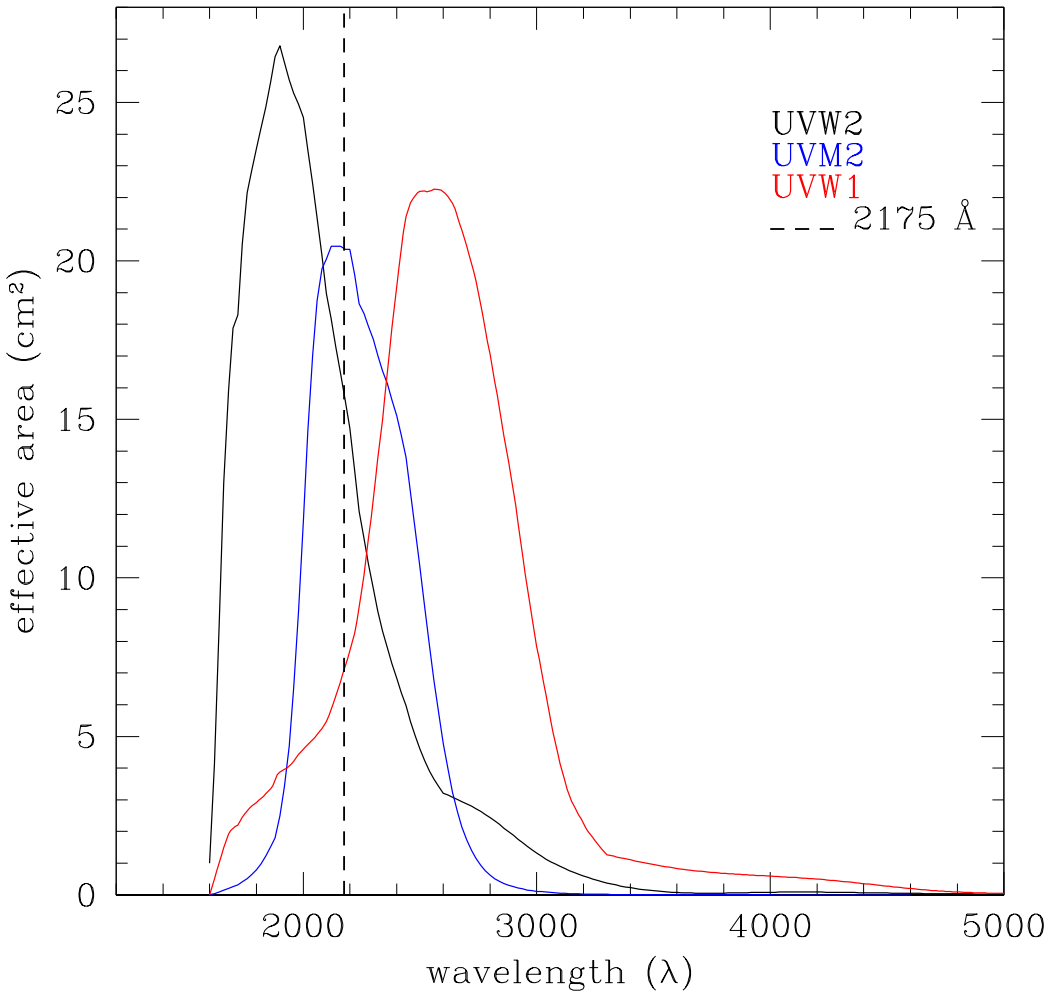

Figure 2.1: UVOT NUV Filter bands UVW2, UVM2 and UVW1. The vertical black dotted line shows the position of the 2175Å dust bump. Notice the UVM2 filter bandpass straddles this "bump". Notice the red leak at the tails of the filters heading into the optical wavelength.

photon counting device.

1. *Red Leak*

UVW2 and UVW1 have a red leak, which is an extension of their filter tail causing larger wavelengths than UV to be included in the filter wavebands, as you can see in the effective area curves in Fig.2.1. The models we use in our study take this red leak into account, see Chapter 3 for more details.

2. *Bad Pixels*

On each CCD there are always a few pixels that are not working correctly and consistently give very low values ("cold pixels") or very high values ("hot pixels"). UVOT images are automatically corrected for bad pixels during the UVOT system processing from RAW to SKY images (Page et al., 2015). A bad pixel map is created for each exposure and then this is used to exclude bad pixels from further analysis.

3. *Cosmic Rays*

When a cosmic ray particle hits a CCD pixel it dumps a lot of charge on it, these electrons are indistinguishable from those released by photons. However the UVOT system ignores cosmic rays when in Image Mode as it can discriminate between a cosmic ray hitting the CCD and a photon hitting the photo-sensitive area. Notice that the CCD itself is not the photo-sensitive area, but a secondary device used to collect the amplified charge (see point 4 below).

4. *Read Noise*

Read noise is the electronic noise generated in the CCD camera when the data is read out from the camera to the computer. However as the CCD in UVOT has a micro-channel plate intensified charged couple device (MIC) the electron photon charge is amplified a million fold, hence making the read noise insignificant in comparison.

5. *Large Scale Sensitivity (LSS) adjustment*

Due to instrument deterioration the large scale sensitivity (LSS) needs to be accounted for. When the co-added images are combined their data is taken at different raw positions on the detector (due to spacecraft drift and roll) and so there is no unique LSS factor that can we can apply to a pixel in a co-added image. Therefore standard corrections for Large Scale Sensitivity (Breeveld et al., 2011) are applied to our images (Hutton et al., 2014) during co-adding as the images are co-added with a LSS map that was created for each exposure.

6. *Zero-Point Drift*

The gradual deterioration of the CCDs also causes the zero point to change slightly over time. Therefore standard corrections for the slow drift in zero point[3] are applied to our images (Hutton et al., 2014) taking into account the dates when the exposures were taken.

7. *Coincidence Loss*

[3]http://heasarc.gsfc.nasa.gov/docs/heasarc/caldb/swift/docs/uvot

As UVOT operates in a photon counting mode the detectors will suffer from coincidence losses at high count-rate. These losses happen when more than one photon hits the same place on the detector within the same time period. As only one photon will be recorded there will be a loss of photon detection. Coincidence losses are mostly important for observations of central galaxy and star forming regions where the count rate is the highest. However we do not use the UVOT optical filters for our photometry as the coincidence loss is so high for these wavebands it can not be accurately accounted for. We include the UV coincidence loss corrections(Poole et al., 2008) in our magnitude equations, more details below.

8. *Dead Time*

Dead time is the time when the instrument is downloading its image information and so will not be detecting photons. This dead time is included in our coincidence loss corrections.

2.4 The Galaxy Sample

In this thesis we model how dust behaves in six nearby "local" galaxies (M51, M81, M82, M77, M100, M101 Messier object numbers). We chose these galaxies because they have varying degrees of star formation, different morphologies and readily available data from the archives over the range of band passes we require for our modelling. Table.2.1 lists the positions and dimensions of these galaxies. We study M82 in the most detail as it is an interesting starburst galaxy with an observable galactic wind (GW) due to its edge-on orientation and as well as modelling its dust

profile we try to characterise its star formation using the light coming from the GW. We make use of the panchromatic data available for this galaxy.

Table 2.1: Position & dimensions of the six galaxies in our survey (http://ned.ipac.caltech.edu/).

	M82	M100	M81	M101	M51a	M77
NGC	3034	4321	3031	5457	5194	1068
Name	"Cigar"	-	"Bodes"	"Pinwheel"	"Whirlpool"	-
RA (s)	09:55:52.725	12:22:54.8	09:55:33.1730	14:03:12.5	13:29:52.7s	02:42:40.7
Dec (s)	+69°40'45.78"	+15°49'19"	+69°03'55.061"	+54°20'56"	+47°11'43"	-00°00'48"
Mag (B_{AB})	9.30	9.84	7.89	8.31	8.96	9.61
Maj Dia (arcmin)	11.2	7.4	26.9	28.8	9	7.1
Min Dia (arcmin)	4.3	6.3	14.1	26.9	8.0	6.0

2.5 Ancillary Data

2.5.1 Optical Data

UVOT provides UV and optical coverage at wavelength range 170-650 nm (1600Å-8000Å) with seven filters. However, we do not use UVOTs optical data as the count rates are much higher (> 0.96/s) than the NUV filters and so the coincidence loss will be higher and can not be corrected accurately (Poole et al., 2008). Therefore we retrieve optical images in the u(ultraviolet), g(green), r(red), i(NIR), and z(infrared) bands from the DR8 version of the Sloan Digital Sky Survey (SDSS) (Aihara et al., 2011) with the waveband range 3048Å to 10833Å.

The SDSS uses a dedicated 2.5 metre telescope which is based at the Apache Point Observatory (APO) in New Mexico. Its 120 megapixel camera images 1.5 square degrees of sky which is $\approx 8 \times$ the area of the full moon. There is also a pair of fibre-fed spectrographs that take the spectra of more than 600 galaxies and quasars in a single observation[4]. The SDSS also uses a Ritchey-Chrétien telescope like UVOT. There are 30 CCDs in the camera each with 2048×2048 pixels. These CCDs are arranged in five columns with six CCDs in each column. Each column is one particular filter and therefore each row represents r, i, u, z and g respectively. Every time the image of the object moves along the columns the data is read. The readings are then reduced to count/sec by the instrument.

[4]http://www.sdss.org

Table 2.2: Properties of the passbands and zero-point values for our eleven filters as per instrument handbooks.

Filter	$\langle\lambda\rangle$	FWHM	Zeropoint (zp)
	Å	Å	mag
UVW2	2033	657	19.11
UVM2	2229	498	18.54
UVW1	2591	693	18.9
FUV	1539	230	20.08
SDSSu	3551	599	22.5
SDSSg	4686	1379	22.5
SDSSr	6165	1382	22.5
SDSSi	7481	1535	22.5
SDSSz	8931	1370	22.5
Hα	6573	67	3733.0
8μm	79274	28427	64.9

2.5.2 Optical PSF

As we will be using both UV and Optical data to do integrated stellar population synthesis modelling of the dust in our galaxies we need to convolve our optical SDSS images to match the larger PSF of the NUV images, using our deepest NUV (UVW2) image as reference, bringing the spatial resolution of the SDSS images (PSF FWHM $\lesssim$ 1.5 arcsec) in line with the UVOTs PSF (FWHM $\lesssim$ 2.5 arcsec). To do this we extract an isolated stellar image from the UVOT UVW2 frame, and use a rescaled version of this frame as a convolution kernel for the SDSS images, changing the scale factor until the PSF of the optical images matches the NUV. A convolution performs a "weighted average" of all the pixels i.e. it multiplies the value of each nearby pixel by the amount given in the kernel, then adds all those values together to produce the final result. Fig.2.2 shows the SDSS image before and after convolution and the UVOT reference image for comparison.

Finally, we rescale and register the SDSS convolved frames to match the UVOT images. The images are rescaled to a pixel size of 0.5 arcsec as the original SDSS images have a pixel size of 0.4 arcsec.

2.5.3 Hα & 8μm & FUV Data

For the purposes of our study of M82 we also retrieve and process Hα, 8μm & FUV Data. The Hα-subtracted image (continuum already removed) of M82 is from the 5th data release of the Spitzer Infrared Nearby Galaxies Survey (SINGS, Kennicutt et al., 2003). We process the Hα images in the same way as we do with our optical images to match the pixel size and resolution of our UVOT images. The 8μm

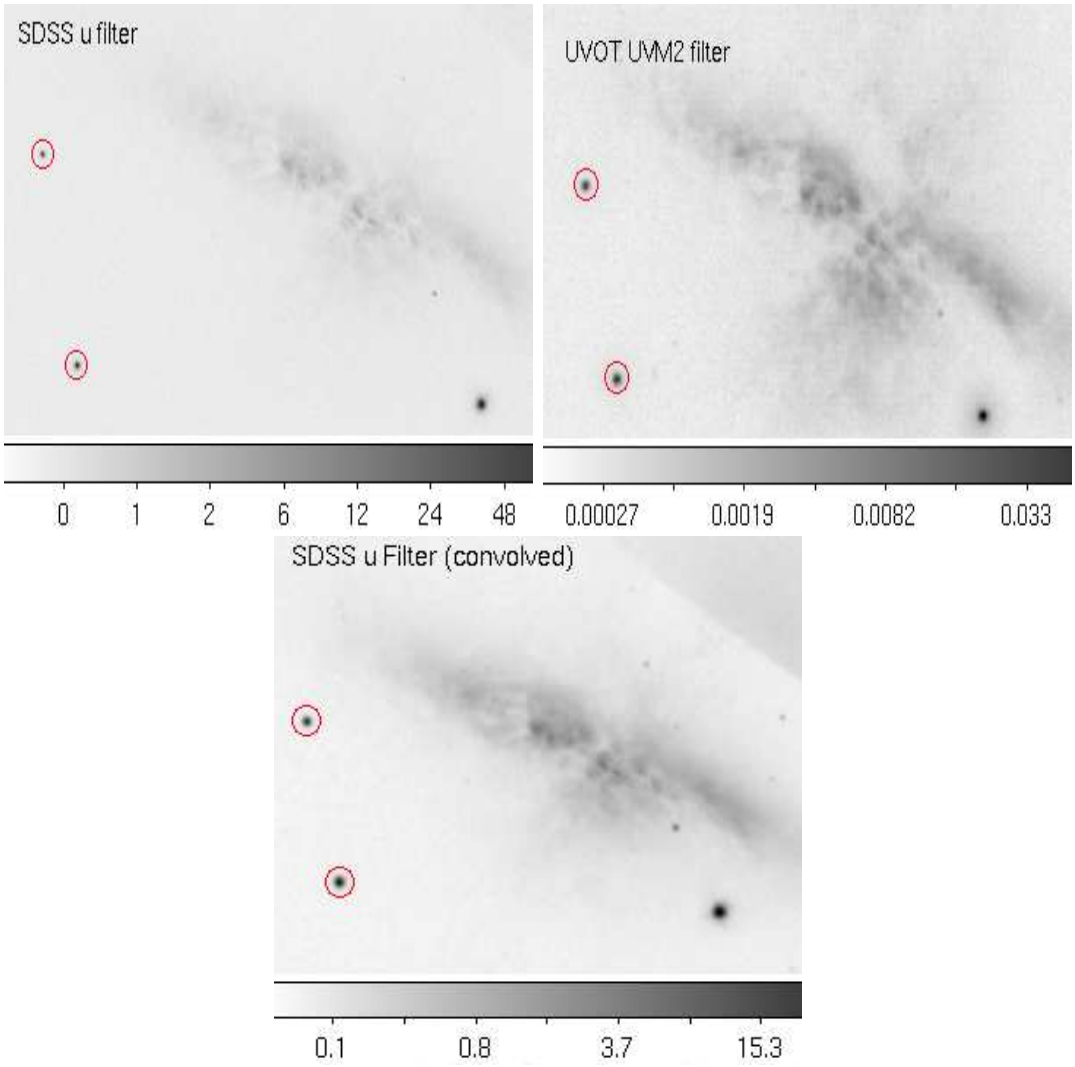

Figure 2.2: SDSS u filter image before convolution (*top left*) and after convolution (*bottom*) is compared to the UVOT UVM2 filter image (*top right*) . You can see the differences between the PSFs of the two instruments especially from the two same point sources (red circles) before and after the SDSS image is convolved. It is evident that the SDSS PSF (1.5 arcsec) is smaller than UVOTs (2.5 arcsec).

data is from the InfraRed Array Camera (IRAC) which is one of three instruments on the Spitzer Space Telescope. IRAC is a powerful survey instrument because of its high sensitivity, large field of view, mapping capabilities and simultaneous four colour imaging. It provides simultaneous imaging at 3.6, 4.5 and 5.8μm and 8μm. The arrays in the camera are 256^2 pixels and each pixel has a size of $\approx$1.2 arcsec. IRAC automatically puts its data products into units of MJy/sr during processing. We then use calibration data from (SINGS, Kennicutt et al., 2003) to calculate the fluxes in erg s^{-1} / cm^2. We retrieve the 8μm images from the same *SINGS* data release as we use for Hα. Given the resolution of the 8μm images and that we won't be using this waveband in our stellar population synthesis analysis we decided only to register and rescale the 8μm images and not to convolve them.

The FUV GALEX images were retrieved from the "Atlas of Nearby Galaxies Survey" (Gil de Paz et al., 2007). We use only the FUV data from GALEX as the NUV bandpass is already covered by UVOT filter bandpasses as you can see in Fig.2.3. GALEX is small by space telescope standards and is a 50 cm modified Ritchey-Chrétien design optimised for 1.2 degree wide field of view. GALEX is so sensitive that it can only look at faint sources and so can not look at any stars we can see from the earth with the naked eye. The GALEX PSF FWHM is 5 - 6 arcsec and the pixel size is 1.5 arcsec and so as GALEX PSF is the largest we convolve our UVW2 image to equal this PSF. As we are using UVW2 as the normalisation filter for our colours, we convolve UVW2 only for colour $UVW2_{conv}$-FUV as we do not want to degrade our other images unnecessarily.

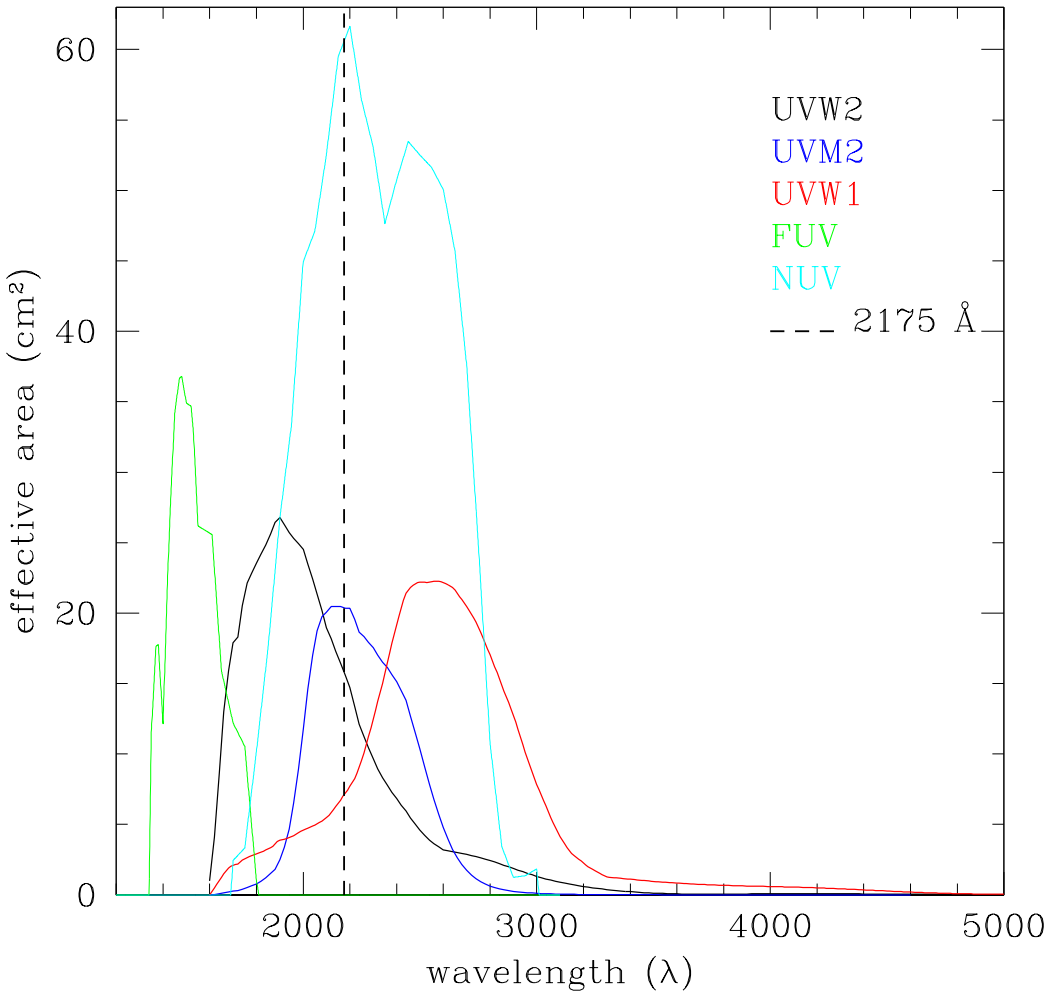

Figure 2.3: Effective area curves for UVOT (NUV) and GALEX (FUV and NUV). The GALEX NUV filter straddles the three UVOT narrower band filters and therefore we use UVOTs filter bands for our photometry.

2.6 Photometry

2.6.1 Comparison of UVOT software & IRAF

We look at the most effective way to reduce UVOT imaging data by comparing two reduction techniques i.e. using the dedicated UVOT software and the more generic IRAF software[5] data reduction package . We do this as we want to understand the UVOT reduction process and its routines.

Because the image files are not mixed with respect to binning we are able to sum up the images for each filter using the UVOT software as the UVOT system can not break down the files to a lower level unlike IRAF. In fact, in order to create a list of images required for summing in IRAF we need to break the files into their individual exposures. We co-add then stack the observations using UVOT's command UVOTIMSUM and we also do this with the IRAF software command IMCOMBINE for comparison.UVOT system parameters automatically trim and align images before summing when using the UVOTIMSUM command hence reducing vignetting. Vignetting happens in all images to some degree and it is a reduction of the pixel saturation at the image borders compared to the centre of the image. We need to trim and align when co-adding using IMCOMBINE.

In order to compare two different sets of images, we need to trim and align one set of images to match the other as both the rotation and the pointing will be slightly different for each exposure, requiring us to shift and re-bin the images before co-adding. We align them so they contain the same positional pixels. To do

[5]http://iraf.noao.edu/docs/spectra.html

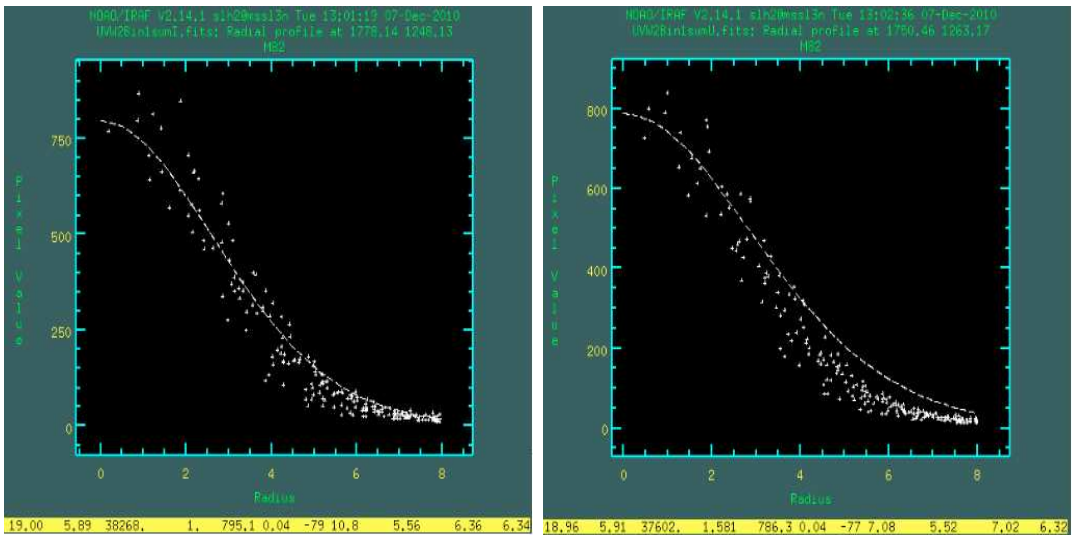

Figure 2.4: *Left:* Radial aperture plot of a star in M82 using the UVW2 image and IRAF data reduction software. *Right* Same as left plot but using UVOT data reduction software. Vertical axis is the number of counts (brightness) and the horizontal axis is the radius in pixels. There is a best-fit gaussian curve drawn using the data points. The numbers at the bottom of the plot from left to right represent (http://casa.colorado.edu/ keeney/classes/astr3520): Radius of the aperture used to fit the profile: The magnitude of the star calculated using equation 2.7 where $\text{mag}_{zero} = 25$ by default but as we are comparing magnitudes it does not matter: The flux of the star: The mean sky counts per pixel in the aperture: The central brightness as per the gaussian profile: Contour ellipticity as IRAF assumes elliptical rather than a circular star: Contour position angle where 0^{o} is along the x-axis of image: FWHM with enclosed flux profile fitted as gaussian: FWHM with individual pixels fitted as gaussian: FWHM not assuming a specific profile. The values are very similar for both plots, hence implying that the two image adding techniques (IRAF & UVOT) do not have a noticeable difference in the binned pixel values and the overall depth and resolution of their images.

this we create a co-ordinate file for a number of stars in the reference image and a shift file containing the appropriate shifts required with respect to the comparison image to match the reference. We use IRAFs "IMALIGN" procedure to do this. The images are then automatically trimmed in order to get the same pixel dimensions.

The corresponding exposure maps are also stacked and aligned using the same process. We then divide the final images by the final exposure files to obtain our counts/second image for each of the filters using the IRAF command "IMARITH". We also use the exposure maps to help when trimming.

We do this comparison for M82 only and we find that the final image quality is similar for both techniques. We sum the images and create our final counts/sec files (using the same exposure files) to see which software package has a more effective reduction process. We conclude that the image combining techniques of IRAF are comparable to UVOT's dedicated software. Hereafter, we use the latter to reduce all our images. See Fig.2.4 for the summed images using both systems, there is little difference between the two images.

2.6.2 Drizzling

Drizzling is a technique that improves the quality of the co-added image by slightly increasing the spatial resolution and S/N ratio. M82's individual exposures were registered and co-added using a standard drizzle algorithm (Fruchter & Hook, 2002).

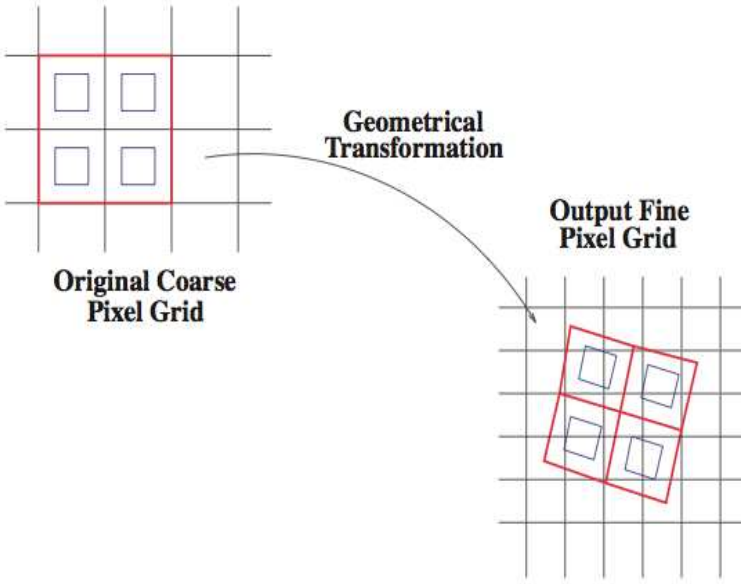

Figure 2.5: Schematic representation of Fruchter & Hooks' "drizzle" procedure (Fruchter & Hook, 2002). The pixel grid corresponding to the input image (*left*) is mapped on to the output grid (*right*) which has smaller pixel sizes. At the same time it corrects for shift, rotation, and geometric distortion in each image. Hence the output image pixels are only affected if the input image pixels overlay them for example the central output pixel receives no information for this sample input image.

The input image pixels are mapped on to an output image grid. The value of the output image pixel is the average of the input pixel with the weight being proportional to the area that the input pixel overlaps the output pixel, see the schematic in Fig.2.5. For the other galaxies in our survey we use IRAFs *SWarp* software [6]. However there isn't much difference between the two procedures.

2.7 Further Reduction Steps

We now have eight count/s images for filters NUV (UVW2, UVM2, UVW1) and optical (u g r i z) for each galaxy and an additional three for M82 (FUV, 8μm

[6] http://www.astromatic.net/software/swarp

and Hα). The spacial sampling of our NUV images (& reference image for our colours) is 0.5 arcsec per pixel therefore to calculate the flux we use a 5 arcsec aperture which is the optimum aperture size for these filters (Poole et al., 2008). We note this aperture is accurately calibrated (Poole et al., 2008; Breeveld et al., 2010) as the 5 arcsec aperture radius is large enough to fully contain the point sources without losing too much flux to neighbouring pixels or taking in too much of the surrounding background flux. We chose a range of apertures for each galaxy to fully encompass the galaxy area that we want to study including the wind in M82. See subsequent chapters for further information on our aperture selection for each galaxy.

2.7.1 Background Removal

When calculating our flux $flux$ we need to remove the effects of the background from the galaxy. We initially tried a full image background analysis by taking a 5 arcsec aperture for every pixel in the M82 image and found the median pixel value for each of these apertures. These median values are shown in the residual background image in Fig. 2.6 for the UVM2 filter. Notice the background image still contains noise especially in areas of high count rates. Therefore we decided not to use this full galaxy method to calculate our background fluxes.

We need to select apertures in the background of the image away from the light contamination of the galaxy and foreground/background sources. Therefore the apertures we select depend on the galaxy morphology. The background annulus'

we use for M81 and M100 are shown for examples. The groups of red apertures in Fig.2.7 and Fig.2.8 show the data sets used for M81 and M100 respectively. Within each aperture measured inside the annulus, we determine the median value of the flux in a pixel, and create a distribution from all the values measured in the apertures located within this annulus. Then we use the median value from this distribution as our background flux $flux_{back}$. We do this for each filter for each galaxy except for Hα as this image has already had its background removed. $flux_{back}$ is then subtracted from each of our pixel values in our image before summing these values in each aperture to obtain the underlying stellar fluxes $flux$. See Table.2.3 for these background pixel values.

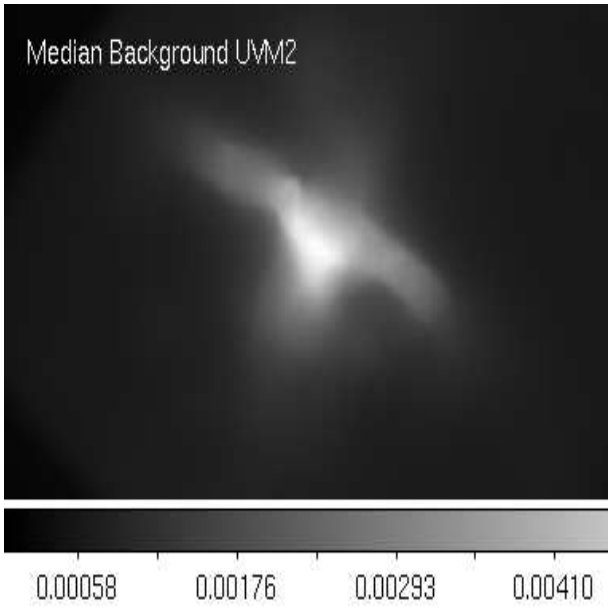

Figure 2.6: UVM2 filter image for M82 showing the median count per aperture for all pixels showing a residual background image. Note the background measurement eventually used in the analysis is taken in an external region, unaffected by the light from the galaxy.

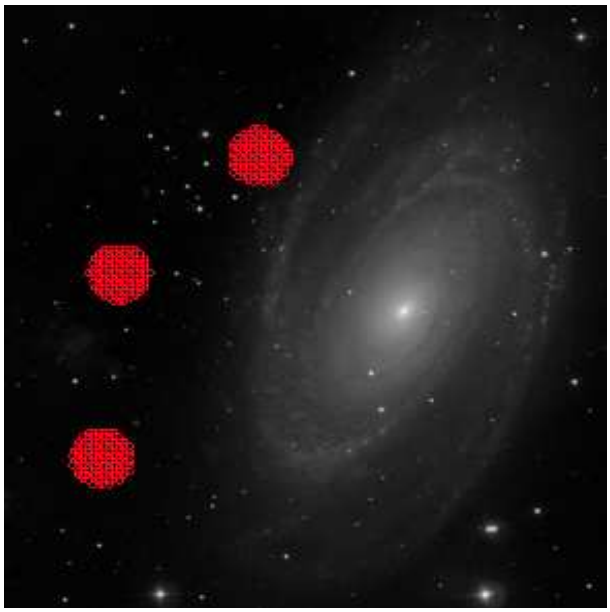

Figure 2.7: UVM2 filter image for M81. The red apertures away from galactic light contamination and foreground/background point sources shows the 5 arcsec apertures we use to calculate the background fluxes. The median pixel value from each of the apertures is added to a distribution. Then the median value from this distribution is used to calculate $flux_{back}$.The median background flux from the pixels in these apertures is used in order to remove the background ($flux_{back}$).

2.7.2 Milky Way Galactic Extinction

We have our background adjusted fluxes for each image so we now need to remove the Milky Way (MW) Galactic Extinction effects. The dusty MW galaxy lies between us the observer and the galaxy we are observing. Dust in the MW will preferentially scatter and absorb shorter wavelengths of light and will subsequently redden the light we see. Therefore we need to remove this reddening effect of the MW in order to disentangle the dust from the stars. To do this we calculate the attenuation of light (*mag*) using a simple stellar population (SSP) model with and without dust and remove this *mag* value in order to obtain the corrected magnitudes without MW extinction effects.

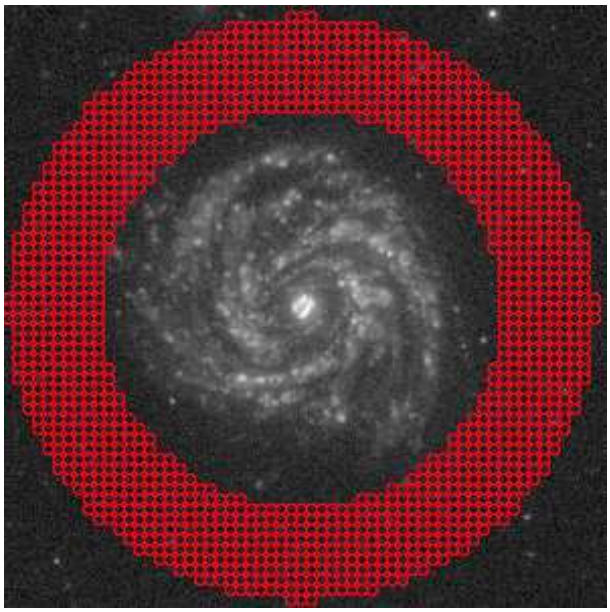

Figure 2.8: UVM2 filter image for M100. The large red aperture is used to calculate $flux_{back}$ as in Fig. 2.7 as it is away from galactic light contamination and foreground/background sources.

The dust model we apply is the standard R_V=3.1 Milky Way attenuation law (Fitzpatrick, 1999b). We run a large set of synthetic population models using "starburst99" stellar models[7] with solar metallicity $Z_\odot$ and age range of 0.001 Gyr to 0.900 Gyr for each filter. We calculate the magnitudes with and without dust. When doing this we take the revised value of reddening E(B-V) from the NED database based on the recalibration (Schlafly & Finkbeiner, 2011) of the Schlegel et al. (1998) dust maps. Note: We use 0.140 for M82 in Chapter 3 and the updated value of 0.054 in subsequent chapters. See Table.2.4 for these E(B-V) values. We then find the difference between these two magnitudes and use the median point of this distribution as the magnitude reduction required to remove the Milky Way extinction from our flux ($flux$) values.

[7] www.stscu.edu/science/starburst99/figs/fig1.html

Table 2.3: Background Removal (count/s)

Filter	M82	M81	M100	M101	M51	M77
UVW2	3.09860e-4	3.23e-4	2.62e-4	2.80e-4	2.56e-4	3.93e-4
UVM2	1.63561e-4	1.55e-4	1.43e-4	3.16e-5	1.45e-4	2.19e-4
UVW1	5.82e-4	7.37e-4	6.40e-4	5.30e-4	6.09e-4	8.70e-4
u	6.18 e-3	2.31e-3	6.33e-3	8.96e-4	5.27e-3	3.45e-3
g	7.48e-3	9.59e-4	1.51e-2	2.69e-4	3.87e-3	6.42e-3
r	1.47e-2	1.37e-2	2.28e-2	1.01e-3	7.71e-3	1.09e-2
i	1.45e-2	2.24e-2	3.41e-2	1.76e-3	7.72e-3	4.36e-3
z	2.71e-2	1.94e-2	3.59e-2	5.20e-3	1.75e-2	1.66e-2
8μm	1.207	–	–	–	–	–
Hα	8.882055e-2	–	–	–	–	–

The foreground Galactic Extinction values quoted in the NED database[8] are also based on the recalibration (Schlafly & Finkbeiner, 2011) of the Schlegel et al. (1998) dust maps assuming a Fitzpatrick reddening law (Fitzpatrick, 1999b) with R_V=3.1. This database contains MW galactic de-reddening values for the SDSS filters and as our values compared well with them we use these NED values in our analysis.

[8]http://ned.ipac.caltech.edu/

Table 2.4: Milky Way galactic reddening (http://ned.ipac.caltech.edu/).

Galaxy	E(B-V)
M82	0.054
M81	0.071
M100	0.023
M101	0.008
M51	0.031
M77	0.030

2.7.3 Limiting Magnitudes

Signal to noise ratio (S/N) is the strength of the signal relative to the noise. In order to confidently detect a signal it is usual to require a S/N≈3 i.e. a $3\,\sigma$ detection. We therefore test the S/N of each of our filters using M82 as our reference galaxy. We calculate the limiting magnitudes for each filter and compare them to the distribution of the magnitudes in our corresponding images. We obtain our limiting magnitudes by taking 1000 measurements within the same-sized circular apertures, in the blank outer regions away from the galaxy or other contaminating sources. We use the median of these values as our magnitude limit. We find that the limiting magnitudes are at least 2 mag fainter than the faintest galaxy and wind photometry aperture measurements for M82 and so we can conclude that our images are deep enough. More details are given in Chapter 3.

2.8 Apparent magnitude Calculations

2.8.1 NUV

Now we have the count/s for each image and filter we first need to calculate the flux for each 5 arcsec radius aperture in order to obtain the magnitude and luminosity values.

1. We divide each of the pixels in the apertures into 25 equal bins (x,y) in order to smooth the corners of the aperture and therefore improve the accuracy of our flux calculation.

2. From each of our pixel x,y values we remove the "Galactic Background" (flux_{back}).

$$flux = flux_{(x,y,0)} - flux_{back} \tag{2.1}$$

3. We then sum up all the pixels in each aperture (0.5 arcsec radius) to get our flux per aperture (*sum*). We then must reduce the *sum* back to the 10 pixel radius size again by dividing by 25 i.e. the number of sub-pixels.

$$sum = (\sum flux)/25 \tag{2.2}$$

4. Now we correct for coincidence loss (Poole et al., 2008). Where C_{theory} is the theoretical coincidence loss count rate. C_{raw} is the raw observed count rate and f_t is the frame time in seconds (ft = 0.0110329s). α is the dead time correction factor. a are the coefficients as per Poole et al. (2008).

$$C = C_{\text{theory}} \times f(\text{x}) \tag{2.3}$$

where;

$$C_{\text{theory}} = \frac{-\ln(1 - \alpha C_{\text{raw}} f_t)}{\alpha f_t} \tag{2.4}$$

$$f(x) = 1 + a_1 x + a_2 x^2 + a_3 x^3 + a_4 x^4 \tag{2.5}$$

$$x = C_{\text{raw}} \times f_{\text{t}} \tag{2.6}$$

5. Using the standard magnitude equation 2.7 we calculate our AB magnitudes for each filter band;

$$mag = mag_{zero} - 2.5 \times log_{10} flux \tag{2.7}$$

mag is the apparent magnitude which is a measure of the brightness of the pixel aperture adjusted to the value it would have in the absence of the atmosphere. mag_{zero} is the zero point in magnitudes and is the single scaling factor for an astronomical imaging system. The mag_{zero} (zeropoints) for each filter are shown in Table.2.2.

6. We use equation 2.7 and substitute for mag_{zero} and $flux$ and remove the Galactic Extinction A_{uv} to get equation 2.8.

$$mag = zp - 2.5 \times log_{10} flux - A_{uv} \tag{2.8}$$

The zero-points *zp* are from the *Swift* archive at HEASARC[9] on the AB magnitude table.

2.8.2 Optical, FUV, 8μm and Hα

The optical, Hα, 8μm & GALEX magnitudes are calculated in a similar manner to the NUV without the need to remove coincidence losses as the instruments are not photon counting. The standard magnitude equation 2.7 has been adapted for our other wavebands ($Optical = SDSS, FUV = GALEX$). We also calculate H$\alpha$ and 8μm luminosity (using calibrations provided for each instrument).

$$mag_{SDSS} = zp - 2.5 \times log_{10} flux - A_{SDSS} \tag{2.9}$$

$$mag_{GALEX} = -2.5 \times log_{10}(flux) + zp - A_{GALEX} \tag{2.10}$$

$$mag_{8\mu m} = -2.5 \times (log_{10}(flux \times B) - log_{10}(zp)) \tag{2.11}$$

$$lum_{H\alpha,8\mu m} = (flux_{erg} \times C) \times 4 \times \pi \times D \times D \tag{2.12}$$

The labels in the above equations relate to;

1. The zero-points *zp* for 8μm and Hα are given in the *SINGS* data release information. For GALEX the zero-point is found in the NASA website[10].

[9] `http://heasarc.gsfc.nasa.gov/docs/swift/`

[10] http://galexgi.gsfc.nasa.gov/docs/galex/

2. We calculate the "Galactic extinction" in magnitudes (denoted A in the equations above).

3. B=1.003 and is the value we use to remove the effects of Milky Way attenuation from our flux.

4. We calculate C as the conversion factor required to obtain the luminosity from the flux.

5. D is the distance of the galaxy to the observer in cm derived from the NED database.

6. flux_{erg} is the flux we calculated through the filters in erg $\text{s}^{-1}/\text{cm}^{-2}$.

2.9 Galaxy Colours

Finally, by calculating the variation in brightness between two wavebands by subtracting the apparent magnitudes of one (usually the longer waveband) from another (usually the shorter waveband) we calculate the colours. In this thesis we use the UVW2 filter as the "shorter waveband" in all our colours except for the colour including FUV (GALEX) used only for M82. The more negative the value the "bluer" the colour and the more positive the "redder" the colour. Bluer can imply hotter stellar populations (younger) than the redder cooler stellar populations (older). However it is never quite that simple, other factors can affect the colour of the light we see from galaxies for example dust reduces the amount of blue light and increases the amount of red light (reddening) hence making the colours redder. Also if the instrument PSF is too large with respect to pixel size then the pixels will not contain all the flux from the object source and so the colour (from

one band with respect to the other) will be redder than it is due to the lack of flux. Also metallicity affects colours as the more metal rich a star is the redder it appears.

Chapter 3

Characterisation of the Stellar Population and Wind Ejecta of M82 with special emphasis on the NUV light.

3.1 Introduction

Nearby star-forming galaxies provide the opportunity to probe our knowledge of the mechanisms controlling star formation. Located at a distance of 3.5 Mpc (Dalcanton et al., 2009), and with a dynamical mass of $\sim 10^{10} M_{\odot}$ (Greco et al., 2012), M82 (NGC 3034) is our closest starburst galaxy. It is part of the M81 group. As M82 is orientated edge-on we are able to see its impressive outflow (Galactic Wind) rising to 10kpc above and below the galactic plane. The power driving this prominent outflow is believed to come from SNe ejecting energy into the inter stellar medium

(ISM) (see, e.g. Mac Low & Ferrara, 1999).

In this chapter we use a panchromatic approach to explore the stellar populations in M82 and the wavelength dependence of the light we see from the wind region. We also study the dust in the galaxy and entrained in the galactic wind (hereafter GW). The light from the wind is believed to be light originated in the galaxy, and scattered away by dust entrained in the gas outflows (Hoopes et al., 2005). To re-cap, starburst galaxies are very dusty and as dust affects the wavelength of light we need to disentangle the dust from the underlying illumination source.

We take advantage of *Swift*/UVOT NUV passbands to help us to understand the properties of the dust in M82. As well as the NUV bands from *Swift* we also include optical, infrared (IR) and Hα imaging for our study using the photometry we resolved and calibrated in Chapter 2 to make estimates of ages, metallicity and dust content. We use stellar population synthesis modelling to do a likelihood analysis of these parameters. We also investigate different star formation histories (SFH) to see how changing these affects the results from the comparison with population synthesis models. We find the effect of changing the SFH is minimal and so adopt the simple one burst scenario (1SSP) for our model.

We then fit an exponential to the wavelength dependence of dust scattering of the light and suggest an upper and lower dust grain size.

This chapter is based on the paper Hutton et al. (2014) and the structure is: We discuss why we chose M82 in §3.2. Reduction of data techniques are shown in §3.3. Our aperture selection is described in §3.4. The background and noise is presented in §3.5 followed by the main section "Stellar Population Synthesis" modelling §3.6. The energy balance is represented in §3.8. Then we discuss dust in the superwind in §3.9 and then suggest a dust scattering model §3.10 before presenting our conclusions in §3.11.

3.2 Why M82?

M82 is an interesting galaxy to study in all areas of the electromagnetic spectrum as it is a bright starburst galaxy with a GW. It also has filamentary dust streams and a bar (Larkin et al., 1994; Telesco et al., 1991) located in its centre, both believed to be due to its recent interaction with the other galaxies in the M81 Group. Interactions can cause gravity related tidal forces and these will have deformed M82, causing its star formation to increase 10 times to $10M_{\odot}$/yr and giving M82 a dynamical mass of $\sim 10^{10}M_{\odot}$ (Greco et al., 2012). "Non Starburst" galaxies have star formation rates of $\approx 1M_{\odot}$/yr like the Milky Way.

Numerous observations have been made in previous studies of M82 over a range of wavebands from X-ray to radio. However, not surprisingly, most previous studies only focus on the central few parsecs of M82 which is the region of intense star formation activity (Hoversten & Glazebrook, 2008) and as this region is shrouded in dust the focus was on the areas that had lower dust content. We however study the whole of the galaxy including the nucleus, disc and also the GW as we are interested

in wavelength dependence of the dust as well as the stellar populations hidden by it. We use stellar population synthesis (SPS) models as a tool for understanding the integrated light that we observe. We use this modelling to determine what mix of stars give rise to the observations.

As M82 appears as an "edge on" galaxy there is a large amount of light obscuration due to dust in the galactic plane in the direction of the observer but less so in the direction of the wind from the galaxy centre. We compare the UV light from the GW with light from the galaxy to test the hypothesis that UV light from the wind is the reflected UV light from the galaxy centre (Hoopes et al., 2005).

We also use UV as a star formation indicator in the galaxy's central regions, with optical to trace evolved stars and Hα for new massive stars. We use 8μm in the mid infrared to map the extent of "hot" dust in the galaxy which is caused by the dust warmed by the starlight. M82 is known to display an "infrared excess" as it is much brighter at infrared wavelengths than in the visible.

3.3 Data Reduction for M82

For our NUV images we use 51 event "extensions" for M82 taken in the UVM2, UVW1 and UVW2 filters. We also use an additional 10 image "extensions" taken in UVW2 and UVM2 filters only. Image observations are binned in 2×2 pixel binning to reduce telemetry whereas the gamma ray burst (GRB) "Event" observations are always 1×1 binning. UVOT reduces these 61 image/event extensions into 10 files,

each having between 3 to 11 image/event extensions. Each image/event extension has one image/event exposure. The reduction method we use is described in detail in Chapter 2. We end up with a single co-added FITS image for each filter for each galaxy.

We convolve the PSF of the optical FITS images to match the larger PSF of the NUV. We also convolve the UVW2 filter image to match the larger PSF of the FUV and we use this convolved image only when calculating the Mag_{FUV}-Mag_{NUV} colours, as the FUV has a larger PSF than the NUV. We do not convolve the Hα and 8μm images as we do not use this photometry to calculate colours. Again more detail can be found in Chapter 2.

We produce red, green, blue (RGB) colour composites of our FITS images so we can see the extent of the optical, UV and Hα light in the galaxy and wind. In Fig 3.1 (*left*) shows the blue, green, and red channels of the RGB image corresponding to UVW2, (SDSS)g and Hα FITS images respectively. We can see that the bulk of the galaxy is mostly blue-green which implies that it is dominated by stars of intermediate ages. Whereas in the central region you can see red (Hα) and blue (UV) emission dominating which indicates a predominance of young massive stars in this area. When we look at the wind in the outer regions (perpendicular to the disc plane) we see blue (UV) emission which could be the reflection of the central UV light scattered by dust in the GW (see §3.9).

3.4 Aperture Selection

At distances of the M81 group of galaxies 1 arcsec in the sky will span a distance of 19 pc. Therefore as UVOT has a FOV of 17 arcmin × 17 arcmin and M82 has an angular size of 9 arcmin × 4 arcmin the UVOT telescope will be large enough to observe these galaxies without the need for mosaics.

As discussed in Chapter 2 the M82 UVOT images are 0.5 arcsec/pixel and we use a 5 arcsec aperture as this is the optimum aperture for the detection of point sources (Poole et al., 2008). Therefore we choose a number of 5 arcsec (radius) apertures for our photometry of M82, as shown in the right panel in Fig 3.1. We remove apertures in areas that are contaminated by foreground stars. Removing contaminated apertures is especially important in the wind region as the flux here is generally lower than in the galaxy as there are no stars and so bright foreground sources would create outliers when looking at the photometry. Our data set consists of 351 (695) apertures in the galaxy (wind) footprint.

From these apertures using our photometry we calculate the magnitudes and hence the galaxy and galactic wind (GW) colours. We compare these colours with our SPS model colours and find the best fits using a χ^2-based analysis. Details of how we calculate the magnitudes for each of our filters can be found in Chapter 2.

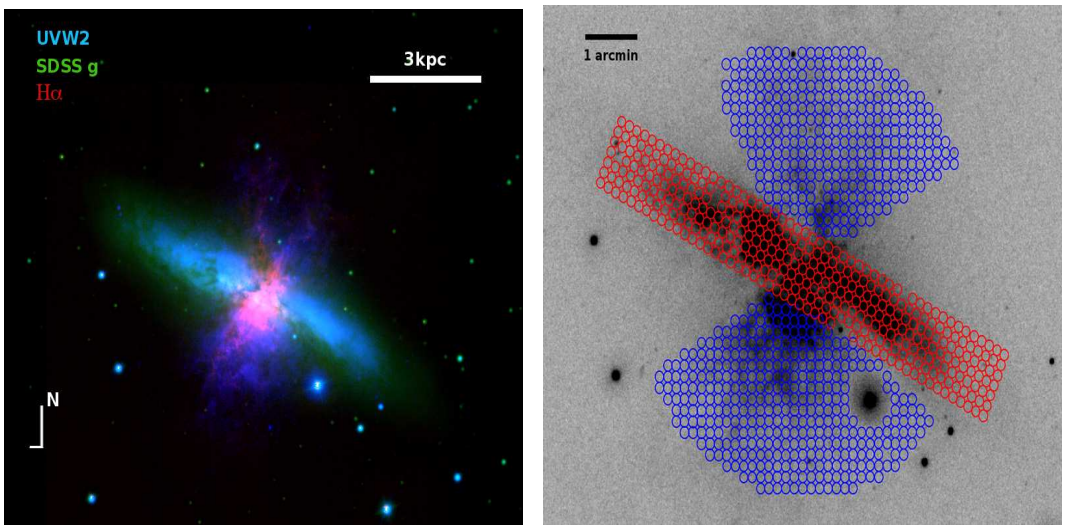

Figure 3.1: *Left:* RGB colour composite of M82 using UVOT/UVW2 (blue), SDSS/g (green) and narrow band Hα (red) images. You can see the extent of the NUV light in the wind and central regions, Hα in the central region and optical in the bulk of the galaxy. *Right:* The 5 arcsec apertures used for our analysis of the galaxy and the wind region are shown in red and blue respectively. The greyscale background image shown here is from the UVW2 filter.

3.5 Background and Noise

3.5.1 Milky Way Attenuation

All the light from M82 has to travel through dusty regions in the Milky Way galaxy along the line of sight before we can observe it and is therefore reddened. So we need to remove this reddening effect by finding how the light is attenuated using a simple stellar population (SSP) and a dust model similar to that in the Milky Way. How we did this is detailed in Chapter 2.

3.5.2 Diffuse Background

We want to study the light from the stellar populations in the galaxy and so we have to remove the diffuse background light of the galaxy in order to do this. In

Chapter 2 we discuss how we remove this background light by finding the median value of all the pixels in the background regions and then using the median value of that distribution as our diffuse galactic background. We choose these regions to be away from the galaxy light and point sources to avoid over-estimating the background flux. We then remove this value from each pixel value before calculating the corresponding flux.

3.5.3 Signal/Noise

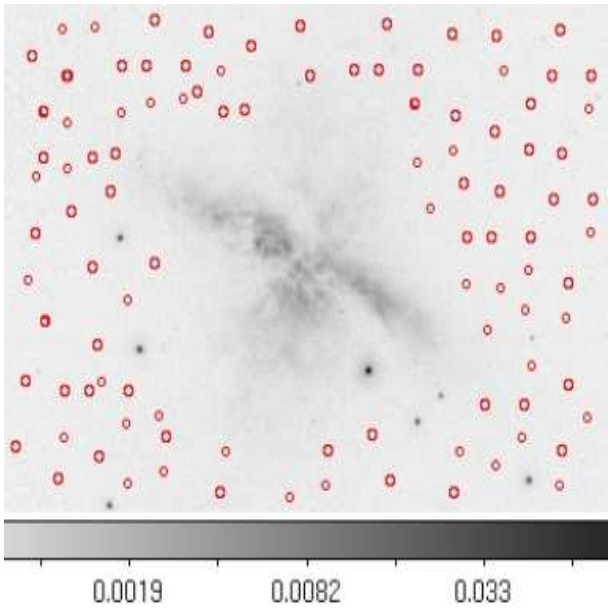

Figure 3.2: UVW2 filter image showing how the 3σ limiting magnitudes were calculated using 1000 apertures in the background image away from galaxy light contamination and foreground/background point sources. The red apertures show a representation of the 1000 apertures used.

As discussed in Chapter 2. in order to confidently detect a signal it is usual to require a S/N>3 i.e. a $3\,\sigma$ detection. Therefore we calculate the limiting magnitudes for each filter and compare them to the distribution of the magnitudes

in our corresponding images. Fig.3.2 shows a representation of the 1000 aperture measurements we take for M82, as you can see they are taken in the regions of the galaxy away from light contamination and point sources.

We plot histograms of the magnitudes we calculated for M82 for each aperture and filter and compare these to our limiting magnitudes, see Fig.3.3. For the NUV photometry we find that the limiting magnitudes are at least 2 mag greater than the galaxy and wind photometry. We conclude that our M82 NUV images are deep enough to be used in a robust analysis. We also found that the data from the other filters are deep enough for our purposes, except for part of the wind region in the shallower SDSSu band. Nevertheless, even in this case, only 11% of the data points fall below this limit, all of them at a projected galactocentric distance $R > 2.6\,\mathrm{kpc}$.

3.6 Stellar Population Synthesis (SPS) Modelling

3.6.1 Nuisance parameters

SPS modelling is used to interpret the light from galaxies by disentangling the dust from the stars. The effect of stellar evolution on the parameters used in these models are known. The standard parameters within these models are the chemical composition (metallicity) and the star formation histories. We use the SSPs of Bruzual & Charlot (2003) in addition to variables controlling the age distribution and the metallicity. We also include an additional parameter that describes the amount of reddening, via a colour excess E(B-V), following our chosen extinction law such as Fitzpatrick (1999b) or Calzetti (2001b). Then for each aperture, we

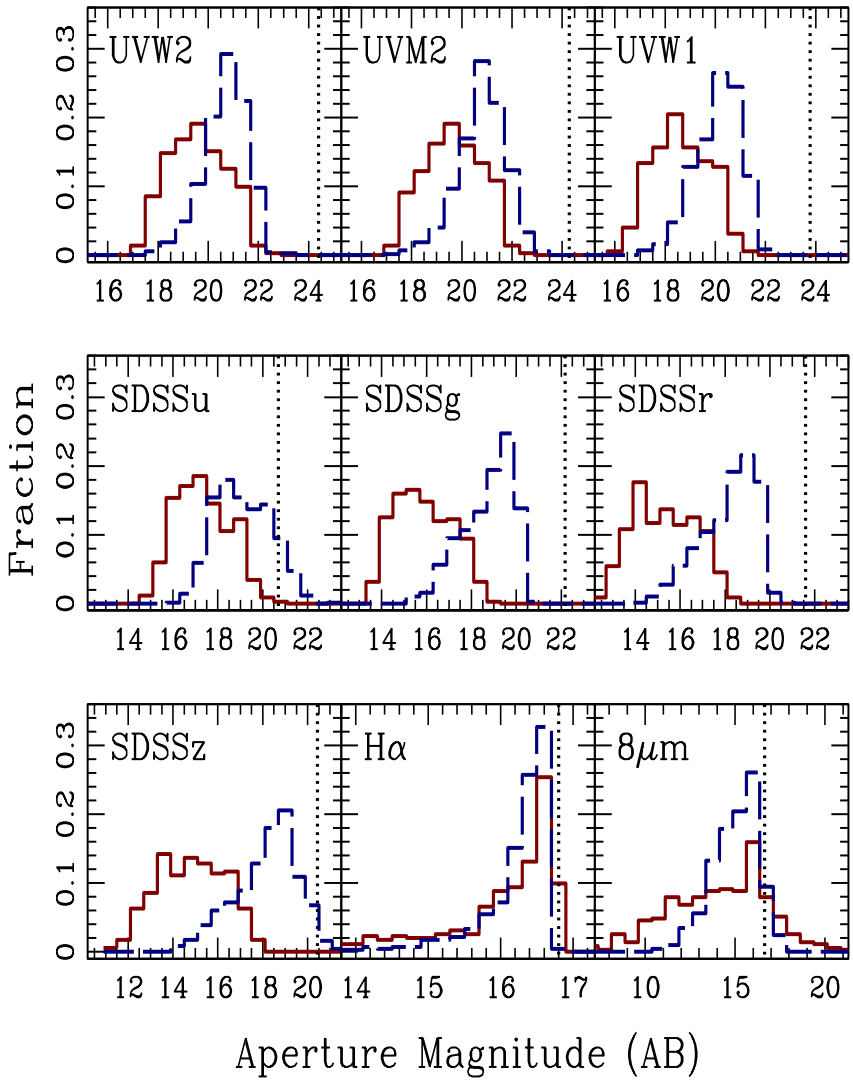

Figure 3.3: Distribution of the aperture magnitudes in the M82 galaxy (solid red histograms) and the wind region (blue dashed). In each panel, the limiting magnitudes are derived from the distribution of fluxes measured in 1000 random apertures in the background (vertical dotted line). Note the histograms of the GALEX/FUV and SDSS-i photometry are not included in this figure to avoid overcrowding.

define a χ^2 in the usual manner, by comparing model and measured data. We then marginalise these parameter values to constrain the data. We also vary the star formation history in the SPS models and see how changing these profiles changes the fit with our observed data. However, we know that age, metallicity and dust

all affect the spectra in similar ways and so the outcome of this modelling needs to be fully understood.

We use the publicly available Bruzual and Charlot (Bruzual & Charlot, 2003) theoretical spectral energy distributions (hereafter SEDs) for our modelling. This model assumes a Chabrier 2003 IMF (Chabrier, 2003a) as derived in the Galactic disc, with the lower and upper mass cut-offs 0.1 $M_{\odot}$ and 100 $M_{\odot}$ respectively. The SEDs are normalised to a total mass of 1 $M_{\odot}$ in stars at age t=0, and the spectra are computed at 221 unequally spaced time-steps from 0 to 20 Gyr. Each spectrum covers the wavelength range from 91$\mathring{A}$ to 160 μm, with a resolution that depends on the spectral library employed.

Choosing metallicities ([Z/H]) from -2 to 0.3, age range from 0.01 Gyr to 10 Gyr and colour excess E(B-V) range from 0 to 0.5 and using 16, 64 and 32 bins respectively. For each of the three parameters we obtain an SPS model with a total of 32,768 different SSP to fit against our observed galaxy colours. Fig.3.4 shows how the NUV and optical colours change with age in our SPS model for three different metallicities for NUV (*top*) and optical (*bottom*) colours. You can see how changing metallicity in the stellar regions changes its colours (Bruzual & Charlot, 2003).

The more negative the colour the bluer it is and the more positive the colour the redder it is. Fig.3.5 shows how the SPS model colours change when varying the age, metallicity and colour excess. On the *left* the older ages are in red and younger

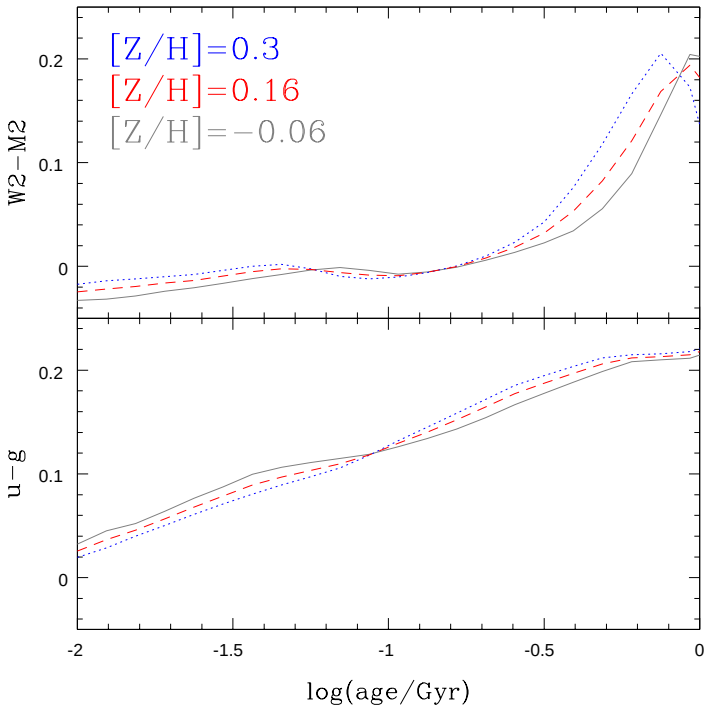

Figure 3.4: Evolution of the NUV (UVW2-UVM2) and optical (u-g) colours of simple stellar populations for different metallicities ([Z/H]), [Z/H]=-0.06 (black solid line), [Z/H]= 0.16 (red dashed line) and [Z/H]= 0.3 (blue dotted line). All models have the Chabrier 2003 IMF truncated at 0.1 and 100 $M_{\odot}$. We use a single star formation model.

ages are in blue. The *right* panels shows the higher the metallicity the redder the colours with the higher metallicity in red and lower in blue. We also show how the increase in colour excess of +0.5 moves the data to the right and hence makes it redder but only for (UVM2-UVW1) and not with (UVW2-UVM2) as shown by the near horizontal black line. This is due to the red leak in the UVW2 and UVW1 filters. As expected you can see that the older ages, higher metallicities and higher colour excess all show redder colours than the younger ages, lower metallicities and lower colour excess respectively.

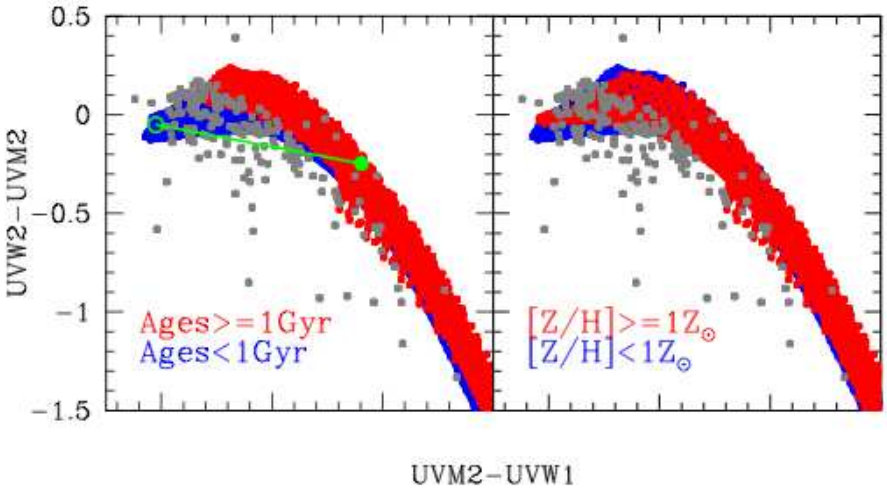

Figure 3.5: NUV colour plots for our SPS model (using our favoured Fitzpatrick dust model). NUV filters showing how the changes in the models ages, metallicity and colour excess effects their colours. *Left:* panel the older ages are in red and younger ages are in blue. We also show how the increase in colour excess of +0.5 (green line from the green open circle to the green filled circle) moves the data to the right and hence makes it redder. *Right:* panel shows the higher the metallicity the redder the colours with red being higher metallicities than blue. The grey dots are M82s galaxy colours for reference.

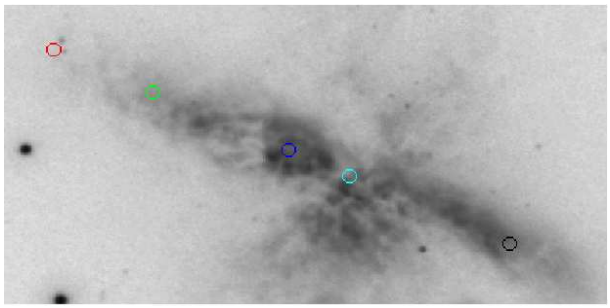

Figure 3.6: Coloured apertures showing where in the galaxy the corresponding cumulative probability curves are from in Fig.3.7.

3.6.2 Degeneracy

Changing the parameters in the model cause changes in the spectra. However, age, metallicity and colour excess E(B-V) can change the spectra in similar ways as they all cause reddening of the light, this behavioural similarity is called degeneracy. In order to illustrate that we are still able to constrain age and dust content using our SPS modelling technique, we calculate the 90% confidence limits for 5 different apertures in the centre of the galaxy.

To do this we fit the observed colours for M82 against our theoretical SEDs (SPS). We compared the colours of the five apertures to all 32,768 different SPS model parameters (64 $\times$ AGE, 32 $\times$ E(B-V), 16 $\times$ Z/H). The χ^2-based method was used to find the best fit. By normalising and then marginalising metallicity and E(B-V) we create the cumulative probability distributions for age. Therefore, by normalising and then marginalising age and metallicity we create similar distributions for E(B-V). Fig.3.6 indicates the galaxy apertures represented in Fig. 3.7, showing age and E(B-V) can be constrained in M82 although with significant uncertainties.

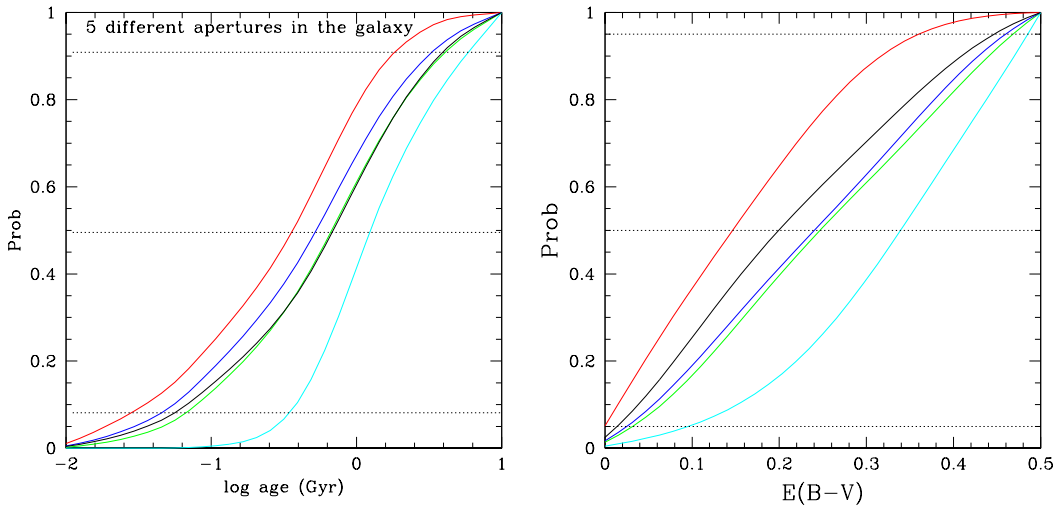

Figure 3.7: M82 galaxy cumulative probability plots showing that we are able to constrain *left* age and *right* E(B-V) over a range of metallicities within a 90% confidence limit.

3.7 NUV photometry and dust extinction

3.7.1 Fitting the Dust Model

Given the passband response curves of the UVOT NUV filters (see, e.g., Breeveld et al., 2011), a colour-colour diagram using these filters is a powerful discriminant of the dust extinction spectral properties of nearby galaxies, especially in the region around the 2175 Å bump. Although the origin of the bump is not clear, it matches a resonance in transitions involving C-ring structures such as graphite, or PAH compounds (see, e.g., Duley & Seahra, 1998). Even though this bump is strong in sight-lines probing the ISM of the Milky Way galaxy (Fitzpatrick & Massa, 1986a), it seems to be absent in starburst galaxies (Calzetti, 2001b). The lack of a strong bump could be indicative of changes in the dust properties (Gordon et al., 1997). However, an age-dependent attenuation law from an otherwise identical dust component can also give rise to different bump strengths (Panuzzo et al., 2007).

We want to test two common dust models, the typical Milky Way "Fitzpatrick" dust model (Fitzpatrick, 1999b) against the standard "Calzetti" starburst dust model (Calzetti, 2001b) and how they fit with M82. Fig.3.8 shows a NUV colour-colour diagram with the three UVOT filters. All four panels show the same photometric data, and each panel overlays a different set of models. We use a set of different SSP models fixing the metallicity and colour excess for each model line leaving the age as a free parameter. Each red line tracks an age sequence corresponding to a simple stellar population from the models of Bruzual & Charlot (2003), at either solar metallicity $Z_{\odot}$ (*top*) or $Z_{\odot}/10$ (*bottom*). The lines span a wide range of ages, from 0.1 Gyr to 10 Gyr (all models run with age increasing from left to right). Within each panel, the different lines probe a range of reddening values, from a colour excess of E(B-V)=0 i.e. no dust (in the top of each panel) to 1 mag, in steps of 0.25 mag. Since these models only explore the evolution of a synthetic stellar population, these tracks should be compared with the photometry in the galaxy region (grey points) and not the wind as stellar populations are not found here.

Even though the models cannot be compared with the photometric data in the wind (blue crosses) this figure illustrates the significantly bluer colours in this region. The photometry in the wind region reveals the presence of dust entrained in the gas ejected from a SNe driven wind (Hoopes et al., 2005) as this dust scatters light from the central starburst. A detailed photometric analysis allowing us to constrain the properties of the dust follows. Finally, the models are also divided with respect to the extinction law, the "Starburst" in the left-hand panels, and a

"Milky-Way" extinction law on the right-hand panels.

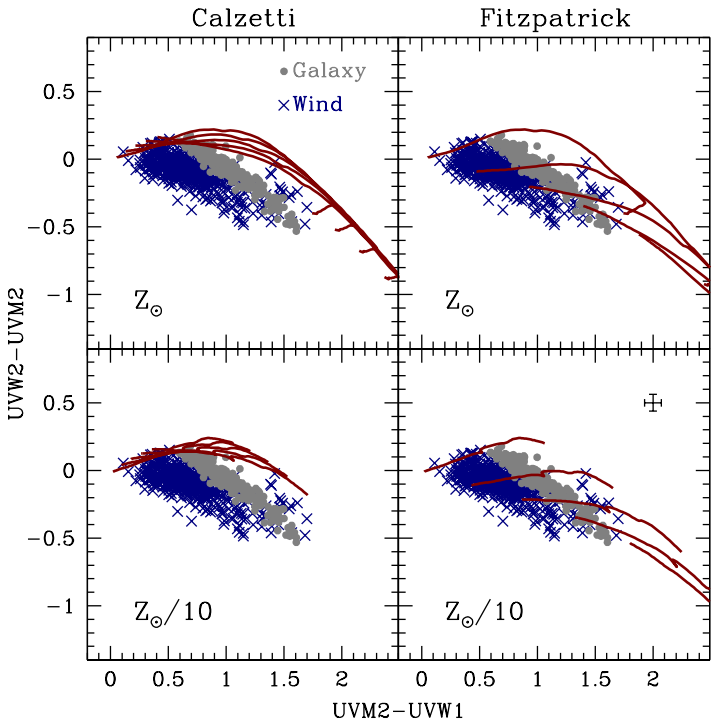

Figure 3.8: NUV colour-colour plots for photometric measurements in the galaxy shown by the grey filled circles within a projected galactocentric distance of 3 kpc *left* central galaxy and *right* outer galaxy. This figure compares the model predictions for two different extinction laws: Calzetti (*top*) and Fitzpatrick (*bottom*). Each line represents an age sequence from 0.1 to 10 Gyr for a simple stellar population from Bruzual & Charlot (2003) at solar metallicity. The lines in each panel correspond to different values of the colour excess, from top to bottom, E(B-V)={0,0.25, 0.50, 0.75, 1} *mag*.

Notice that although the models span a wide range of age, metallicity and colour excess, the Calzetti extinction law (*left*) can not account for the observations. A "Fitzpatrick" extinction law (*right*) however covers all the data points, suggesting that the extinction law of M82 shows a prominent NUV bump. The UVM2 filter straddles the 2175 Å bump feature, so this diagram is especially constraining with

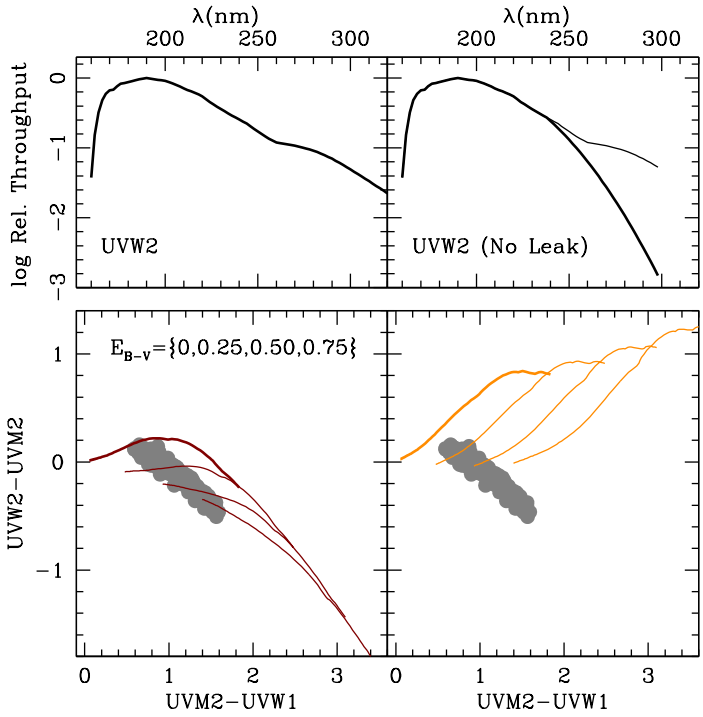

Figure 3.9: NUV colour plots of M82 showing the SSP model tracks with the Fitzpatrick extinction law. The top panel shows the UVW2 filter throughput without a cut-off λ applied (*left panels*) and with a λ cut-off effectively removing the red leak (*right panels*). The bottom panels show the corresponding SPS models with the "Fitzpatrick" extinction law. The result showing "Fitzpatrick" in favour of the "Calzetti" law does not change as removing the red leak would also move the galaxy colours (grey filled circles) from aligning top left to bottom right to alignment bottom right to the top left.

respect to the presence of the bump. Notice the increasingly blue value of the UVW2−UVM2 colour with increasing age. This is caused by the presence of a red leak that introduces flux in the UVW2 filter for older populations. We emphasise that the models take into account the red leak. Fig.3.9 shows the effect of removing the red leak from the UVW2 filter in the model i.e. removing the longer wavelength.

Hence, our NUV colour-colour diagram strongly rules out a "bump-less" Calzetti-

type law, which can either reflect intrinsic changes in the dust properties or in the star formation history compared to starbursts well represented by such an attenuation law. We emphasise that it is mainly in the NUV region where a standard Milky-Way-type law is preferred over a Calzetti law.

3.7.2 Star Formation Histories (SFH)

We present here an extended analysis of the stellar populations, exploring a wide range of star formation histories to derive a more quantitative assessment of the extinction law. We run three grids of models corresponding to different star formation histories: single burst models (1SSP); two-burst models (2SSP) and exponentially decaying models (EXP). Table.3.1 shows the model parameters and the sampling used in the grids. We use the SSPs of Bruzual & Charlot (2003) to build the grids. In addition to the parameters controlling the age distribution and the metallicity, we include the amount of reddening shown by the colour excess E(B-V), following again either the extinction law of Fitzpatrick (Fitzpatrick, 1999b) or Calzetti (Calzetti, 2001b). We use all three SFHs in order to find the most favourable SFH using χ^2 without introducing selection effects into our data. For each aperture, we define a χ^2 in the usual manner, by comparing model (MOD) and measured (OBS) data, using the SDSS g band measurement as normalisation. Hence for each aperture, we define:

$$\chi^2 \equiv \sum_{i=1}^{8} \frac{(c_i^{\rm OBS} - c_i^{\rm MOD})^2}{\sigma^2(c_i^{\rm MOD})}, \tag{3.1}$$

where the $\{c_i\}$ represent the aperture colours, defined as

$$c_i = \begin{cases} g - X_i, & i < 8 \\ \mathrm{FUV} - \mathrm{UVW2}_c, & i = 8 \end{cases}$$

with X_i ={UVW2,UVM2,UVW1,u,r,i,z} ($i < 8$), and $\sigma(c_i^{\mathrm{OBS}})$ is the uncertainty of the i^{th} observed colour. The last term ($i = 8$) corresponds to the colour between the GALEX FUV band and UVW2, where the comparison requires the UVW2 image to be convolved to the (lower) resolution of the FUV passband, thus the notation $\mathrm{UVW2}_c$.

Therefore, we calculate the χ^2-based best fit i.e. ${\chi^2}_{min}$ for all apertures in the galaxy. In Fig. 3.10 we show a histogram of the corresponding NUV χ^2_{min} value to derive the statistic. We do this for both "Calzetti" and "Fitzpatrick" dust models. In order to determine whether there are differences between the dust extinction law in the central starburst or the periphery – where a more standard MW-type behaviour is expected – the figure is split between the central kpc and the outer regions.

As you can see from this figure the "Fitzpatrick" dust model is favoured in both the inner galaxy and in the galaxy as a whole but it's in the inner part of the galaxy where the preference to Fitzpatrick is the strongest. Therefore this figure provides a more quantitative confirmation of the preference of a Milky Way (hereafter MW) type of extinction law with respect to a "bump-less" (Calzetti, 2001b) extinction curve. One could expect that a projected measurement of an edge-on galaxy such

Table 3.1: Model parameters used for the grid of star formation histories. Each model is defined by the star formation rate, $\psi(t)$. In the EXP models, we define t_U as the age of the Universe at z=0.

Single Burst (SSP): $\psi(t) \propto \delta(t - t_0)$			
Observable	Parameter	Range	Steps
Age	$\log(t_0/\mathrm{Gyr})$	$-2 \cdots + 0.7$	64
Metallicity	$\log Z/Z_\odot$	$-2 \cdots + 0.3$	16
Dust	E(B-V)	$0 \cdots 1$	32
		Number of models	$32,768$
Two Bursts (2SSP): $\psi(t) \propto \Big[f_Y \delta(t - t_Y) + (1 - f_Y)\delta(t - t_O)\Big]$			
Observable	Parameter	Range	Steps
Age, Old	(t_O/Gyr)	$0.5 \cdots 12$	16
Age, Young	$\log(t_Y/\mathrm{Gyr})$	$-2 \cdots - 0.3$	16
Young Mass Fraction	f_Y	$0 \cdots 1$	16
Metallicity	$\log Z/Z_\odot$	$-2 \cdots + 0.3$	16
Dust	E(B-V)	$0 \cdots 1$	32
		Number of models	$2,097,152$
Exponentially decaying rate (EXP): $\psi(t) \propto \exp\Big[-(t - t_{FOR})/\tau\Big]$			
Observable	Parameter	Range	Steps
Formation Time	$\log t_S \equiv \log[(t_U - t_{FOR})/\mathrm{Gyr}]$	$-1 \cdots + 1$	32
Timescale	$\log(\tau/\mathrm{Gyr})$	$-1 \cdots + 1$	32
Metallicity	$\log Z/Z_\odot$	$-2 \cdots + 0.3$	16
Dust	E(B-V)	$0 \cdots 1$	32
		Number of models	$524,288$
		TOTAL	2.65×10^6

as M82 would introduce a MW-type extinction from the outer regions seen along the line of sight as we are seeing the normal interstellar medium. However, the fact that the ages and colour excess at R<1 kpc are clearly different from the rest would imply that the central burst makes a large contribution to the photometry in many of the R<1 kpc apertures. Therefore, we can tentatively conclude that a Calzetti law is not favoured in the starburst region of M82.

For a meaningful comparison, we consider only models that are acceptable, rejecting those results with a total reduced $\chi^2_r > 5$ in either the Calzetti or the Fitzpatrick cases. Only models with a best fit reddening E(B-V) > 0.1mag are included, since regions with low reddening will not be sufficiently informative for the discrimination between extinction laws.

Fig.3.11 illustrates the goodness of fit with three typical cases at different galacto-centric radii (as labelled). The error bars indicate the aperture photometry (the horizontal error bars span the FWHM of the filter). The blue line corresponds to the best fit spectrum in each case. The same apertures are shown for a Fitzpatrick (*left*) or a Calzetti (*right*) extinction law. Notice again the significant mismatch of the NUV photometry at shorter wavelengths when using the Calzetti function, revealing the presence of the NUV bump.

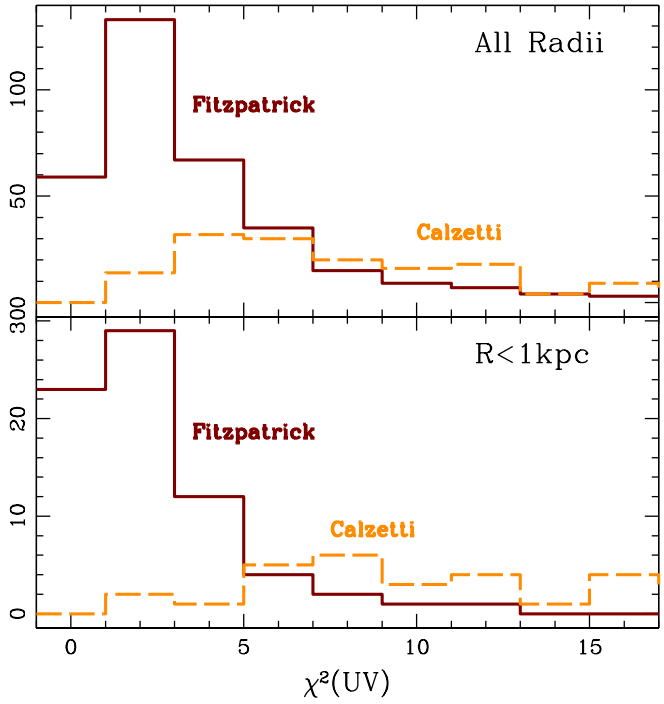

Figure 3.10: Comparison of the best fits between a Calzetti (dashed lines) and a Fitzpatrick (solid lines) extinction law. Both optical and NUV photometry is used to constrain the model parameters but in this case we use just the NUV photometry to define a new statistic, $\chi^2(UV)$. The results are restricted to models with an acceptable *total* reduced $\chi^2_r < 5$ for either the Calzetti, or the Fitzpatrick model, and with a corresponding colour excess of E(B-V) $> 0.1\,mag$. The distributions for the inner regions (R<1 kpc) are shown in the bottom panel. A wide range of star formation histories are explored, including simple stellar populations; exponentially decaying models and a two-burst superposition (see text for details).

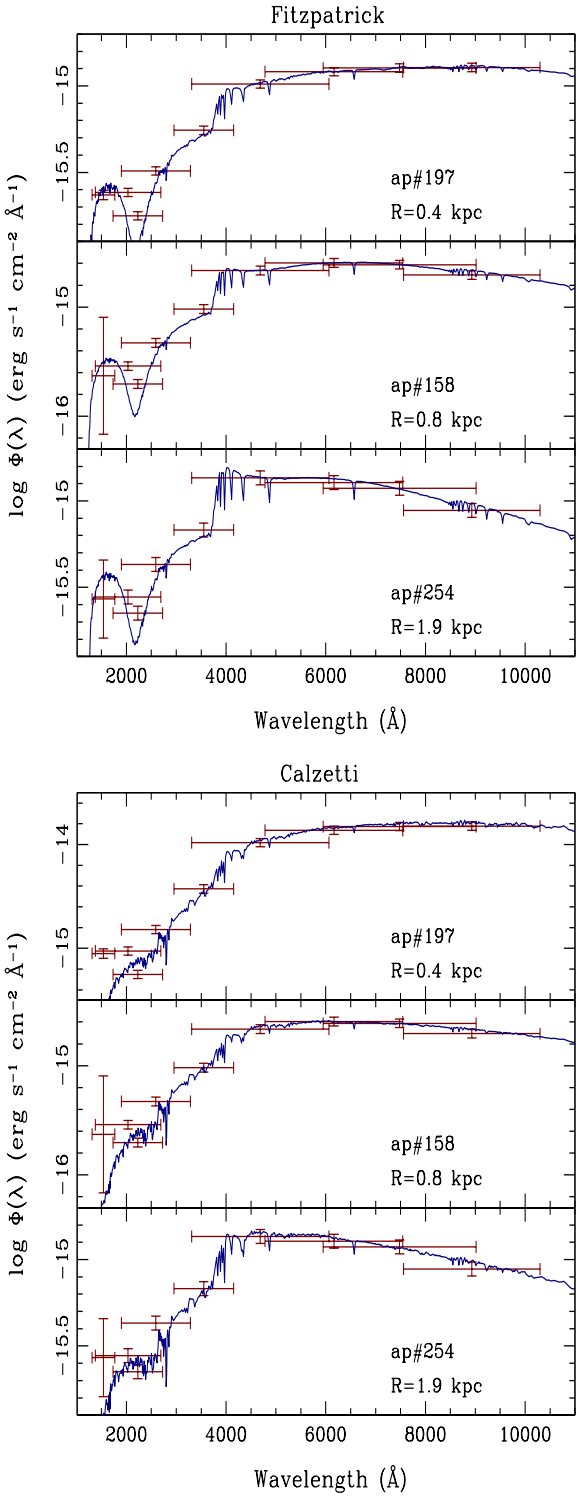

Figure 3.11: Comparison between observed NUV/Optical photometry (red error bars) and the best-fit models (blue) for three aperture measurements at different galacto-centric distances, as labelled. The best fits are shown assuming either a Fitzpatrick (*top*) or a Calzetti (*bottom*) dust extinction law. Note the significant difference between these two in the NUV region, where the bump creates a dip in the Fitzpatrick case.

3.7.3 Stellar Population Characteristics

In Fig.3.12, we extend the colour-colour diagrams to optical wavelengths to model the age and metallicity of the stellar populations in the galaxy. The sample is split between the inner (where the starburst is taking place) and the outer parts of the galaxy (not including the GW). We use an SSP model showing three tracks with an age sequence and an increasing colour excess, with the dust extinction profile following our favoured "Fitzpatrick" (Fitzpatrick, 1999b) extinction law. As you can see, the age and dust distribution of the stellar populations is consistent with the scenario of an encounter with M81 in the recent $\lesssim 400\,\mathrm{Myr}$.

Fig.3.13 (*left*) shows the probability-weighted age (*top*) and colour excess (*bottom*), for the Fitzpatrick (1999b) extinction law, corresponding to the single burst (1SSP) models. For reference, the age and dust reddening estimates from Rodríguez-Merino et al. (2011) are included as grey shaded regions, showing there is good agreement within the uncertainties. As we have seen in §3.6, the metallicity is treated in this thesis as a nuisance parameter. We emphasise that metallicity cannot be constrained with this type of photometric data alone. Therefore, our modelling considers a range of values for the metallicity, but the analysis then marginalises over this parameter. The distribution of reduced χ^2_r values has a median of 0.70, and ∼90% of the data points have $\chi^2_r < 3.0$ Hence, the reduced values of χ^2 stay around χ^2_r ∼1–3, showing that the fits are quite acceptable.

Fig. 3.13 (*right*) shows the parameters of the best fits for the composite population models: the top panels give the mass fraction in young stars ($\mathrm{f_Y}$) with respect

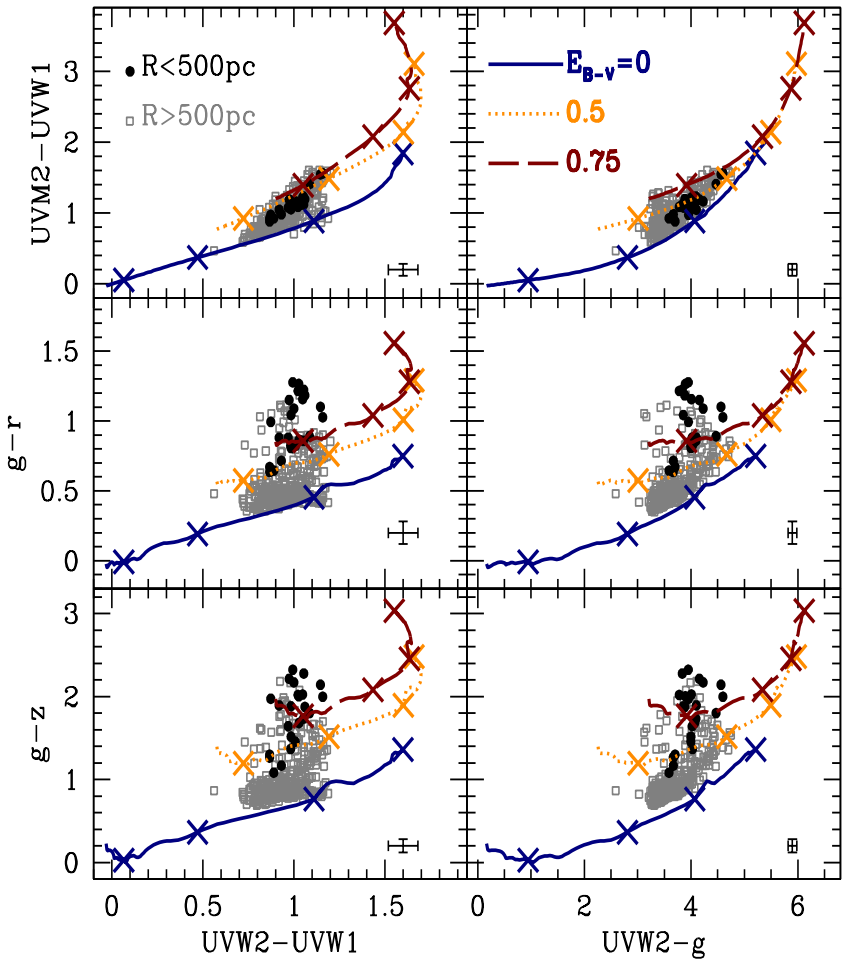

Figure 3.12: NUV and optical colour-colour diagrams of the photometric data in the galaxy region. The sample is split with respect to the projected galacto-centric distance (R), as labelled. For reference, an age sequence at solar metallicity is shown, from the models of Bruzual & Charlot (2003) assuming a dustless population (blue solid lines) and two dusty cases (orange dotted lines for E(B-V)=0.5; and red dashed lines for E(B-V)=0.75), following the chosen Fitzpatrick (1999b) extinction law. The crosses mark, from left to right, stellar ages of 0.1, 0.5, 1 and 5 Gyr. A typical error bar is shown in each panel.

to the age of the young component (t_Y) for a 2SSP model; whereas the bottom panels show the exponential timescale (τ), and the average stellar age for the EXP models. Here, we split the sample into two panels (*left/right*), with respect to the

projected galacto-centric distance, as labelled. Note that in the outer region, the populations are well described by a relatively homogeneous population with ages in the range $0.5 - 1.5$ Gyr, regardless of the model used. Within the central kpc, the populations are significantly younger than the outer regions. However the modelling is unable to distinguish whether the younger ages are caused by an extended period of star formation (i.e. EXP models) or after a recent burst (i.e. 2SSP models). For the general sample, the distribution $\Delta\chi^2 \equiv \chi^2_{\rm min,2SSP} - \chi^2_{\rm min,EXP}$ has a mean of -1.3 with an RMS of 2.9, hence slightly favouring a two-burst scenario.

3.8 Wavelength dependence of Dust Scattering (Energy Balance)

In order to probe the light scattered by dust in the wind, Fig.3.14 compares the radial profile in the galaxy and wind regions at different wavebands, UVW2, SDSSg, 8μm and Hα. There is a very sharp radial decrease of the 8μm data in the galaxy region, in contrast with a milder gradient in the wind region, reflecting an additional contribution at 8μm from intrinsic emission of the dust entrained in the wind material. In addition, the gradient at shorter wavelengths is shallower in the wind region, a consequence of the wavelength-dependent scattering of light from the dust component as dust scatters the shorter wavelengths of light in preference to longer wavelengths. This effect is easier to visualise in Fig.3.15 where we show the average value of the flux in several regions in the galaxy (*top left*) and the wind (*bottom left*). For reference, we include the integrated spectral energy distribution of M82 from the templates of Lonsdale et al. (2004). Notice the good agreement

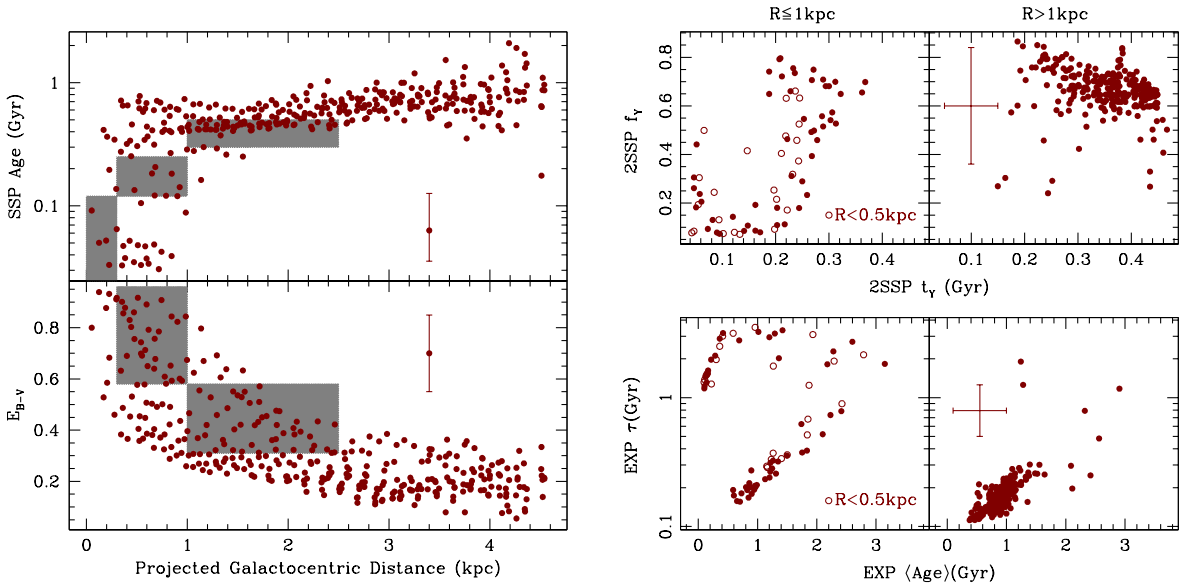

Figure 3.13: *Left* Best-fit SSP equivalent ages (*top*) and colour excess (*bottom*) of the data in the galaxy region, obtained by a comparison with a set of 32,768 simple stellar populations from the models of Bruzual & Charlot (2003) (see text for details). A characteristic $1\,\sigma$ error bar is shown in each case. The grey regions correspond to the range of ages and colour excess from Rodríguez-Merino et al. (2011). *Right* Best fits for composite models: the top panels show the values of the young component in age (t_Y) and stellar mass fraction (f_Y) for the 2SSP models; whereas the bottom panels correspond to the average age and timescale for the exponentially decaying SFHs. The data are split with respect to galactocentric distance, as labelled (top), and typical $1\,\sigma$ error bars are included in the rightmost panels.

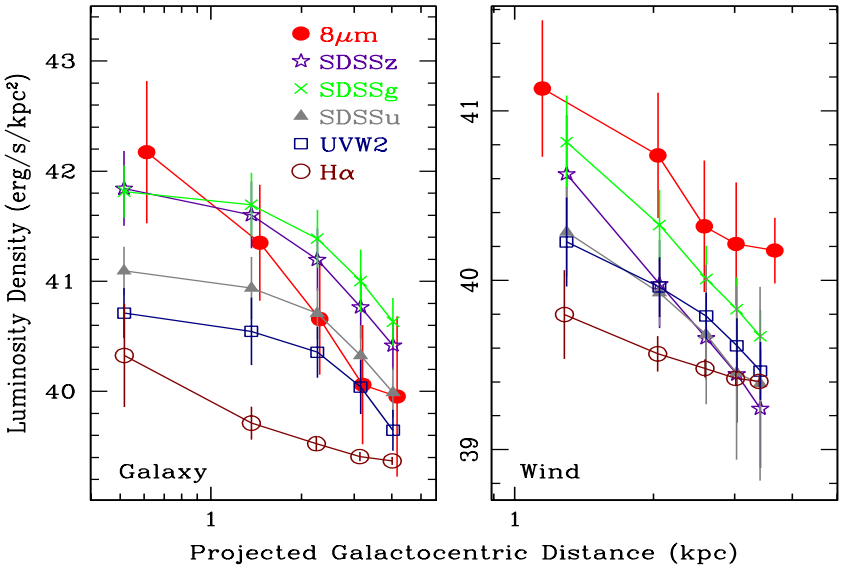

Figure 3.14: Radial profile of luminosity density in the wind (*left*) and galaxy region (*right*) of M82. The points correspond to the median value within bins in projected radial position (the binning is done at fixed number of data points per bin). The RMS scatter in each bin is shown as an error bar.

in the central part of the galaxy, where the starburst phase is taking place. As we move further out along the galaxy disc, the PAH-dominated emission at 8μm drops sharply. In contrast, the wind region shows a smaller decrease of the 8μm flux with radial distance, and the NUV-optical spectrum becomes significantly bluer. Previously we relate this trend with the properties of the dust entrained in the wind.

The comparison of the NUV/optical and FIR spectrum of M82 in Fig.3.15 (*left*) raises the issue of the energetic balance between the light "removed" by dust from the NUV/optical region, and the FIR emission which corresponds to energy re-radiated by the heated dust. We should see a correlation between the two. In other words, if there is starburst we can't see in the NUV due to it being shrouded in dust, the amount of FIR emission we do see should match this hidden NUV.

Fig.3.15 (*right*) shows the result for a simple model, where the original template of M82, shown in the leftmost panels, is de-reddened according to the colour excess, E(B-V), which is taken as a free parameter (horizontal axis). The vertical axis represents the ratio between the observed total IR luminosity (measured at $\lambda > 8\,\mu$m) and the difference in luminosity between the energy of the spectrum de-reddened and observed i.e. we subtract the observed energy in the UV-optical range ($0.1 < \lambda/\mu\mathrm{m} < 1$) from the one corresponding to the de-reddened spectrum for a given E(B-V), using the standard Fitzpatrick (solid line) or Calzetti (dashed line) extinction law. Note that the $\mathrm{L_{IR}}/\Delta\mathrm{L_{UV/Opt}} = 1$ case (horizontal dotted line) corresponds to the 1:1 balance between the UV/Optical light absorbed by dust and the dust emission at longer wavelengths. If there is a balance, our findings should fit this line. The histograms (*bottom*) are the distributions of best-fit E(B-V) obtained in the modelling of the stellar populations of the R<1 kpc apertures (see, e.g. Fig.3.13), confirming that the reddening obtained is consistent. Therefore, within uncertainties, all dust-enshrouded light is accounted for by the FIR energy distribution.

3.9 Dust in the superwind

In this section we test the hypothesis that the NUV light we see in the wind region is that scattered by dust. Fig.3.16 shows the UVW2$-X$ radial colour profiles in the wind region (blue crosses along with the RMS scatter as error bars), with X ranging from GALEX/FUV to the SDSS z band, as labelled. For reference, the flatter radial profiles of the colours in the galaxy region are shown in each panel as

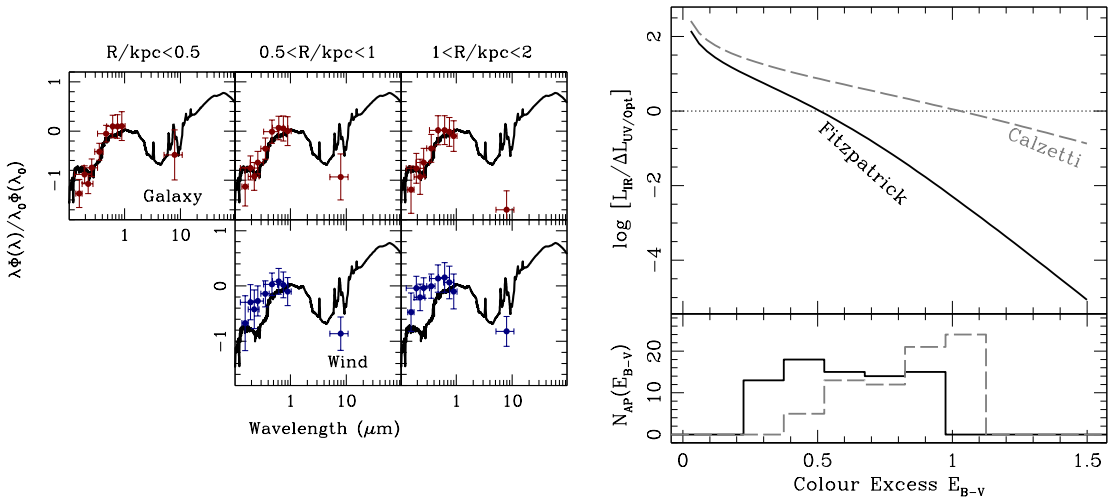

Figure 3.15: *Left*: Comparison of the UV to IR spectral energy distribution in the galaxy (red points; top) and wind (blue points; bottom) regions, with respect to projected radial distance to the centre. The data include GALEX/FUV; UVOT/UVW2, UVM2, UVW1; SDSS/u, g, r, i, z and IRAC 8μm. The horizontal error bars indicate the spectral coverage of each passband, while the vertical error bars show the RMS scatter within each radial bin. The black line is a template of the M82 spectrum (Lonsdale et al., 2004). All data are normalised to the flux at $\lambda_0 = 0.8\mu$m. Notice the sharp decrease at 8μm in the galaxy with increasing distance. In the wind region, the bluer SED is caused by starlight scattered from dust entrained in the wind, and the milder decrease in 8μm reveals intrinsic emission far from the galactic plane. *Right*: (top) The ratio between the observed IR luminosity ($\lambda > 8\,\mu$m) and UV/Optical excess luminosity (estimated between the observed and the unreddened spectra in $0.1 < \lambda/\mu\text{m} < 1$) is shown with respect to colour excess for the Fitzpatrick (black solid line) or Calzetti (grey dashed line) attenuation laws. (Bottom) The histograms represent the best-fit values from the SSP models for the R<1 kpc apertures (see Fig. 3.13).

a red line with a shaded area extending over the observed RMS scatter. The colour gradients in the galaxy increase slightly with wavelength, as expected from typical variations in stellar age, metallicity and dust reddening. However, the gradients in the wind region are significantly steeper. Extrapolations of the colour in the wind region at galactocentric distances of 0 and 3 kpc are shown as star symbols. Light from the wind region can be explained only by scattering, shocks or photoionisation. However, the recent analysis of Hoopes et al. (2005), using GALEX UV and Hα photometry reject the last two, leaving dust scattering as the main cause for the observed light.

As a reference, the error bars on the left-hand side of each panel in Fig.3.16 give the predicted colours of a model for all measurements at R<1 kpc, for which the dust screen from the best-fit result is removed, keeping the age and metallicity unchanged. The large scatter is a result of the wide range of values of E(B-V) in the central region of the galaxy (see Fig. 3.13, *left*). These colours are in most cases bluer than the photometric measurements in the wind, showing that the illumination source from the starburst must be significantly affected by dust.

We now explore how the colour varies between the light in the central part of the galaxy where the emission originates (R=0kpc) and the outer region of the wind where the contribution is almost exclusively caused by dust scattering (R=3kpc). The variation of the colours between R=0 and R=3kpc in the wind region are shown with respect to wavelength in Fig.3.17 (filled dots), where the error bars correspond

to the RMS scatter. For reference, a generic dust scattering law is assumed:

$$\sigma_{\rm scat} \propto \lambda^{-x} \tag{3.2}$$

The three lines in Fig.3.17 represent the expectation for three choices of x, as labelled. Assuming the incident light originates in the central starburst, we use simple stellar population models with the same age and reddening properties as in the central regions of the galaxy, and modify the spectrum according to equation 3.2. The inset gives the probability distribution function keeping x as a free parameter, where we find $x = 1.53 \pm 0.17$ (1σ error bar). We note that in the limit of small particle size (Rayleigh scattering), $x = 4$, whereas in the opposite regime of dust grains much larger than the incident wavelength, $x = 0$ is expected (Draine, 2011).

3.10 A simple dust scattering model

The radiation from the galactic wind cone of M82 is scattered light from the starburst in the central region by free electrons, molecules and dust entrenched in the wind outflows. Scattering by free electrons is practically Thomson scattering, whose cross-section is independent of the wavelength of the incident radiation.

When molecules scatter light the process depends on the relationship between the size of the dust molecule and the wavelength of the light. Scattering by molecules can be described as a Rayleigh scattering process given the smaller size of the molecules with respect to the wavelength of the optical/NUV radiation. The cross section of Rayleigh scattering scales as λ^{-4}, thus the process preferably

scatters the higher-frequency radiation away from the incident rays. Scattering by dust particles is more complicated. However, as an approximation, if we neglect the thermodynamics of the process, we may employ the Mie prescription, in which the scattering dust kernels are modelled by dielectric or metallic spheres and the incident radiation as waves. There are two distinctive regimes in this scattering process, depending on the ratio between the wavelength of the incident radiation and the size of the scattering spheres. The critical wavelength (λ_c) that divides the two regimes is therefore determined by the characteristic size of the scattering sphere (a_c). Radiation with $\lambda > \lambda_c$, will be scattered with the Rayleigh scaling. For $\lambda < \lambda_c$ if ignoring resonant features, the cross-section is practically independent of the wavelength of the incident radiation, and the process will be described by Thomson scattering. The size of the dust particle compared to the wavelength of the incident radiation and the geometry of the light source compared to the scattering substance e.g. in M82 the angle of the outflow to the galaxy major-axis. does affect the λ dependence of scattering. However considering M82's wind cone orientation with respect to the source we don't have to worry about it in weak scattering situations.

In centre panel of Fig.3.18, we show that the observed $\propto \lambda^{-1.53}$ dependence (Fig.3.17) can be obtained by a dust model for the wind cone with a size distribution $n(a) \propto a^{-2.5}$, where a is the dust grain radius. In addition, the particles must have upper and lower size limits such that the critical wavelengths corresponding to these size limits fall outside of the wavelength range covered (i.e. limited by the grey shaded regions in Fig.3.18). An almost perfect power-law is obtained, with

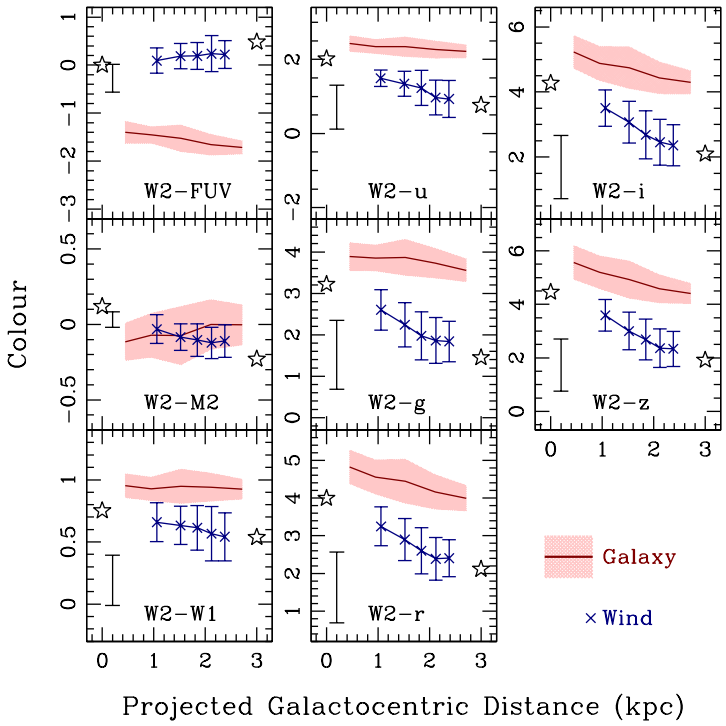

Figure 3.16: Radial plots of the measured colours in the wind (blue crosses) and galaxy areas (red line and shaded regions). The colours, UVW2−X, with X ranging from UVM2 to SDSS-z, are given as the the median values, binned at a fixed number of data points per bin. The error bars and the extent of the shaded regions give the RMS spread within each bin. The stars show the extrapolated colours in the wind region at R=0 and 3 kpc. The error bar on the left-hand side of each panel is the predicted best-fit SSP models at R<1 kpc when the dust screen is removed (see text for details).

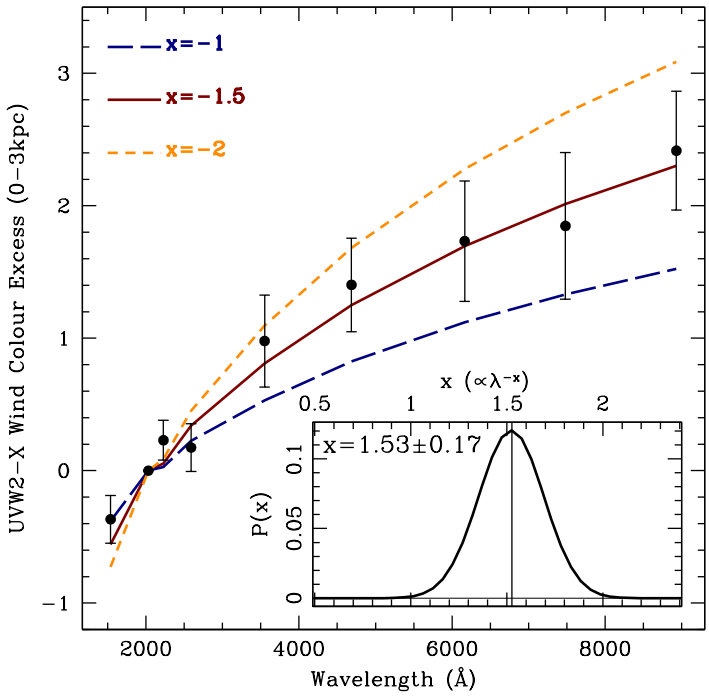

Figure 3.17: Colour variation between the galaxy and the wind against wavelength. The black filled circles are the observations, including the RMS scatter as error bars. The three lines correspond to different dust scattering laws, proportional to λ^{-x}. The inset shows the probability distribution function for the power law index x.

similar wavelength dependence to our results. Alternatively, the grain size distribution can be flatter, i.e. $n(a) \propto a^{-\gamma}$, where the power law index $\gamma < 2.5$, with an additional constraint on the maximum size of the dust particles. The critical wavelengths corresponding to the largest grains must lie within the wavelength range covered by the observations. In this case, we would not obtain a power law but the result would be compatible with the observed $\propto \lambda^{-1.53}$ behaviour. This dependence is due to the presence of a broad transition region between the Rayleigh scattering regime (with λ^{-4} dependence) and the Thomson scattering regime (practically independent of λ) within the spectral range covered. The bottom panel of Fig. 3.18 demonstrates that an acceptable fit can be generated for a dust size distribution $n(a) \propto a^{-1.8}$ with the additional constraint of an upper size limit ($a_{\rm MAX}$), that gives a critical wavelength $\lambda_c(a_{\rm MAX}) \simeq 1\mu$m.

Hutton et al. (2014) shows that the observed $\lambda^{-1.53}$ dependence of the radiation in the NUV/optical data can be explained by a simple dust scattering model. They assume an incident radiation originating from a point source in the core of the galaxy and as we have suggested the observed light in the wind region is due to the scattering of this radiation by the dust particles in the wind. Hutton et al. (2014) use the hypothesis that as sizes of dust particles are relative to the wavelength of radiation then the dependence would be "smeared" if there were lots of different sizes of dust grains present. The bottom panel of Fig.3.18 demonstrates that an acceptable fit can be generated for a dust size distribution $n(a) \propto a^{-1.8}$ with the additional constraint of an upper size limit ($a_{\rm MAX}$), that gives a critical wavelength $\lambda_c(a_{\rm MAX}) \simeq 1\mu$m. The conclusion is that an upper grain size limit is compatible

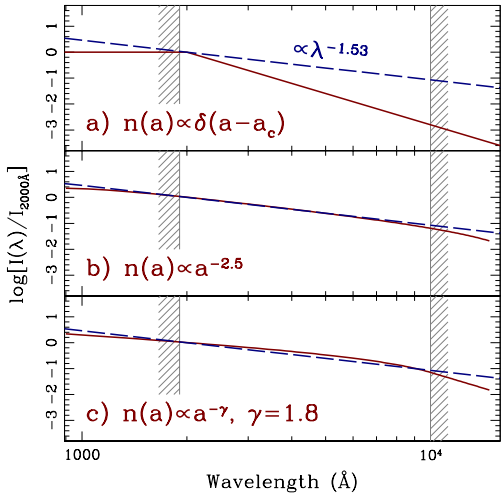

Figure 3.18: Predictions for the intensity of light scattered by the three simple dust models considered in §3.9. The grey shaded regions mark the ends of the observed wavelength coverage, and the blue dashed line in all three panels corresponds to a fiducial $\propto \lambda^{-1.53}$ behaviour, from the observational constraints (see Fig. 3.17). The $\propto \lambda^{-1.53}$ behaviour is due to the presence of a broad transition region between the Rayleigh scattering regime (with λ^{-4} dependence) and the Thomson scattering regime (practically independent of λ) within the spectral range covered and varying critical λ. The plots show how changing the critical λ result in different power laws.

with the photometric observations in the wind region.

3.11 Conclusions

M82 is the nearest starburst galaxy, allowing us to explore with a high level of detail the various processes of this important phase of galaxy evolution. We present here a study of deep NUV images taken by the UV/Optical Telescope on board the *Swift* observatory. We combine them with additional UV, optical and IR archival data, to explore the properties of the stellar populations in the galaxy, and the dust entrained in the SNe driven wind. The NUV colour-colour diagram – especially sensitive to the presence of the 2175 Å bump – reveals a strong rejection of traditional

extinction curves used for starburst galaxies (Calzetti, 2001b) which lack a bump. The standard Milky Way extinction (e.g. Fitzpatrick, 1999b) is favoured (Fig. 3.8). The stellar populations reveal a very young core, with luminosity-weighted ages around $\lesssim$ 100 Myr and large extinction (E(B-V)$\approx$0.5 mag at projected galactocentric distances R<1 kpc). In the outer regions, the galaxy has an overall homogeneous distribution of 0.7–1 Gyr old populations, with lower, but significant (E(B-V)$\approx$ 0.2 mag) colour excess (Fig. 3.13). In the wind region, the spectral energy distribution is bluer, and the PAH-dominated emission at 8μm does not decrease with galactocentric distance as sharply as along the disc (Fig. 3.14). These two trends reflect the contribution from dust scattering, and from intrinsic dust emission, respectively. In addition, the energy balance between the observed IR ($\lambda > 8\mu$m) emission and the UV/optical ($\lambda < 1\mu$m) energy absorbed by dust according to our best-fit models, suggests that there is no excess energy in the form of a heavily dust-enshrouded starburst (see Fig. 3.15, *right*).

It has also been shown in Hutton et al. (2014) that by comparing our colours in the wind region over a wide separation in galacto-centric distance, $\Delta R = 3$ kpc, a behaviour $\propto \lambda^{-1.5}$ (Fig 3.17), was found implying either a distribution of dust grain sizes as $n(a) \propto a^{-2.5}$, or a flatter distribution, e.g. $n(a) \propto a^{-1.8}$, along with an upper size limit that results in a critical wavelength within the spectral coverage of the instrumentation. Although detailed values of this size limit would require information about the grain composition, this result would suggest that only small grains are entrained in the SNe-driven wind.

The radial gradients of the NUV and optical colours in the super-wind region support the hypothesis that the emission in the wind cone is driven by scattering from dust grains entrained in the ejecta.

Chapter 4

Variations of the dust properties of M82 with galacto-centric distance

4.1 Introduction

Extinction is defined as the wavelength dependence of the reduction in light between the source and the observer. In astronomy this is due to the scattering and/or absorption of this light by dust grains. The extinction law provides us with information on the overall properties of the dust grains in the interstellar medium (Draine, 2011). For observations of other galaxies, we can consider the dust in the Milky Way (MW) as a foreground dust screen between these galaxies and the observer. The MW extinction law was found by comparing the light emitted from stars of similar spectral type, at different distances. However, this extinction law has significant scatter (Fitzpatrick & Massa, 1990).

It is found that dust scattering depends on wavelength as $\propto \lambda^{-x}$ where $x = 4$ for air molecules in our atmosphere, $x = 1.5$ for the Milky Way (Fitzpatrick, 1999b) and for M82, (Hutton et al., 2014) it is found it to be $x = 1.53$. The smaller (larger) the grain size the steeper (shallower) the law and hence the higher (lower) the value of x. One classical parameter of this smooth wavelength dependence is the ratio of total-to-selective extinction R_V. In this Chapter we measure R_V for M82 with respect to galacto-centric distance and include in this smooth extinction law a feature of increased extinction at $2175\mathring{A}$ (Stecher, 1969) (variable B), hereafter known as the "dust bump". Fig.4.1 shows how this variable changes the dust law and how it relates to a MW type profile when $B = 1$ (Fitzpatrick, 1999b) and starburst galaxy type profile when $B = 0$ (Calzetti, 2001b). What type of dust grain causes this "dust bump" is still under discussion. It has been found in some studies that the MW (in NUV) shows this feature (Fitzpatrick & Massa, 1986b) but star-bursting galaxies do not (Calzetti, 2001b) .

We can not assume that the intergalactic dust acts as a foreground screen because the dust distribution is mixed with the underlying stellar populations, we refer to this integrated effect of dust in the interstellar medium (ISM) as attenuation. However, galaxies with the same extinction (hence dust properties) can have different attenuation profiles and the "dust bump" (and lack of) can therefore be due to either the dust component causing this bump or the existence of different stellar populations yielding different dust properties (Panuzzo et al., 2007).

In this Chapter we focus on the dust attenuation in the nearby star-burst galaxy M82 (details of this galaxy can be found in Chapter 1). In Hutton et al. (2014) we found that in NUV the central regions of M82 fitted best with a dust law containing this "dust bump" contrary to the belief that star-burst galaxies don't have this bump. This Chapter extends this analysis to probe the strength of the "dust bump" in M82 and the dust attenuation properties in general.

The recent supernova SN2014J in M82 went off after the date of our observed data and so we are fortunate to be able to gain an insight into the dust properties in the region of the supernova before the explosion. We compare our values of R_V and E(B-V) with those published soon after the incident (Amanullah et al., 2014).

This chapter is based on the paper Hutton et al. (2015). The structure is as follows: We introduce the Chapter in §4.1, then discuss the data in §4.2. We model the attenuation law in §4.3 and then try to constrain the dust parameters in §4.4. We compare the observations to simulated photometric data in §4.5. §4.6 discusses the radial profiles of the dust parameters. Then in §4.7 we discuss the results in the previous section. The next section (§4.8) investigates the region around SN2014J and in the final section §4.9, we refer to other studies of attenuation in different galaxies. Then the conclusions.

4.2 Data

As this Chapter follows on from the previous chapter where we present a correlation in the dust profile with galacto-centric distance of M82, we use the same

data, but extend the analysis to quantify the "dust dump" and other attenuation parameters. As we focus on attenuation and the "dust bump" we do not use the 8 μm and Hα photometry this time, but use the same dataset for the FUV, NUV and optical passbands. The NUV images were taken from the UVOT instrument onboard the *Swift* telescope between 2008 and 2012 i.e. before SN2014J. To recap, the UVOT provides us with three NUV passbands, UVW2, UVM2, UVW1 (10.2, 13.9, 8.7 kiloseconds exposure time respectively) with the significance here being that the UVM2 filter straddles the 2175Å dust bump. The FUV photometry came from GALEX and the optical photometry from the SDSS DR8 archives. More details about these instruments and the data reduction we adopted can be found in Chapter 2.

There are however two updates to the data used in Chapter 3 and Hutton et al. (2014). Firstly in Hutton et al. (2014) we use E(B-V)=0.140 mag for the dust attenuation from Schlafly & Finkbeiner (2011) as stated in the NED database [1] whereas in this chapter we use an updated value of E(B-V)=0.054 *mag* (Dalcanton et al., 2009) hence reducing the effects of the foreground Milky Way reddening towards M82. Changing this value affects the corrections we make to our observed photometry and therefore the corresponding dust models. However our results are comparable to those found in Chapter 3. We also use a more recent estimate to M82 of 3.33 Mpc (Foley et al., 2014) in contrast to 3.5 Mpc (Dalcanton et al., 2009) used previously. This distance only affects the mapping of distances for our 5 arcsec apertures which are now 160 pc in diameter.

[1] https://ned.ipac.caltech.edu/

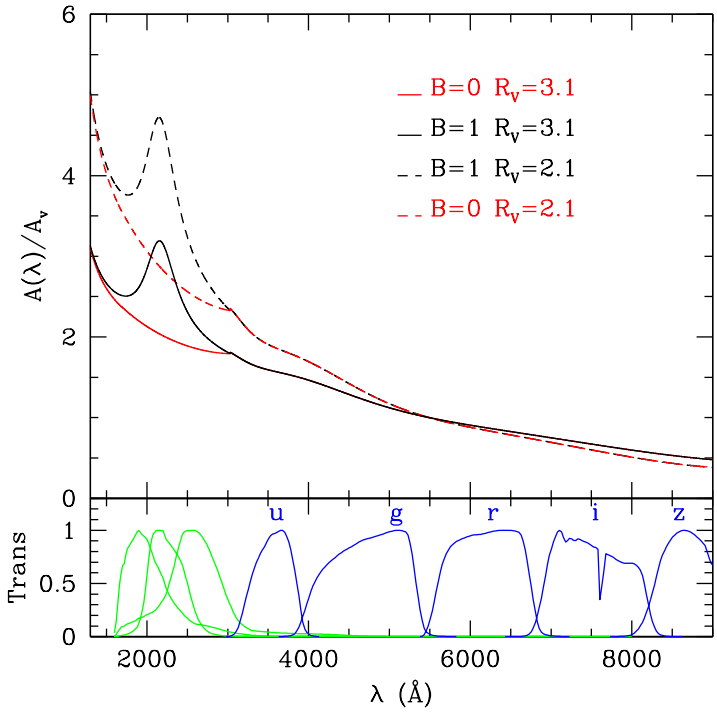

Figure 4.1: This plot shows how changing the strength of 2175Å dust bump, B and R_V changes the attenuation curve. We use an attenuation law by Conroy et al. (2010a). The green filter transmission curves are UVW2, UVM2 and UVW1 respectively and the blue are the optical SDSS filter curves as labelled. Only NUV are required to map the bump but optical are needed too for the total dust attenuation to be fully explored.

4.3 Modelling The Attenuation Law

In chapter 3 we show that the central regions of M82 reflect a dust law with a prominent 2175Å bump rather than a smooth profile without the bump. We use a stellar population synthesis (SPS) model as in the previous chapter but instead of including a standard MW type law (Fitzpatrick) or a standard starburst law (Calzetti) we use a law (Conroy et al., 2010a) with a variable B representing the

dust bump strength. This attenuation law allows us to investigate the strength of the UV bump in the central regions of M82 (R<5 kpc). Fig.4.1 shows that for B=1, the attenuation shows a standard Milky Way type law, and when $B = 0$ we get a Calzetti type law, using the standard value of total to selective extinction R_V=3.1. Any value of B between 0 and 1 indicates that there exists some degree of a 2175Å bump.

R_V and B are intrinsic to the effective dust attenuation law whereas E(B-V) can be considered as a normalising factor reflecting the amount of dust present. Fig.4.1 shows how R_V varies in both UV and optical, and a higher value of R_V results in a flatter attenuation law. Larger dust grains will yield higher values of R_V. Since a proper determination of R_V requires a wide spectral window, unlike for B we use both UV and optical photometry to constrain this parameter. Optical photometry is insensitive to the presence of the bump and therefore will "wash-out" the constraining power of the model. The GALEX FUV waveband provides coverage of the shorter wavelength blue-ward of the bump.

We focus on the central part of M82 as we are interested in the effects of starburst on dust. We do not include the reflected light outside of the disc plane in the galactic wind as presented in the previous chapter, as this reflected light is due to dust entrained in the wind. Also, the power law found in Hutton et al. (2014) describing the absorption/scattering process $\lambda \propto \lambda^{-1.53}$ relates to the dust in this super-wind and not the dust causing the attenuation in the main body of the galaxy.

Table 4.1: Parameter range of the grid of simple stellar population models used to derive the effective dust-related properties. Each model is defined by the star formation rate, $\psi(t)$.

Single Burst (SSP): $\psi(t) \propto \delta(t - t_0)$			
Observable	Parameter	Range	Steps
Age	$\log(t_0/\mathrm{Gyr})$	$-2 \cdots + 0.9$	32
Metallicity	$\log Z/Z_\odot$	$-1.5 \cdots + 0.3$	8
Total to selective extinction ratio	R_v	$0.5 \cdots 4.5$	32
NUV Bump Strength	B	$0 \cdots 1.3$	32
Colour excess	E_{B-V}	$0 \cdots 1.5$	32
		Number of models	$8,388,608$

4.4 Constraining the Dust Values

4.4.1 χ^2-based Method

As well as the strength of the "dust bump" B we constrain the dust attenuation parameter R_V and colour excess E(B-V). Now we use the same stellar population synthesis (SPS) technique adopted for M82 in our previous chapter, but this time using a larger grid comprising of 8,388,608 simple stellar populations (SSPs). Each SSP has a single age and metallicity and uses a standard IMF (Chabrier, 2003b). We marginalise R_V, B and E(B-V) in order to constrain these parameters for each of our photometric apertures.

We use a χ^2-based likelihood as a probability distribution function $P \propto e^{-\Delta\chi^2/2}$

from which we derive the 68% confidence limit errors for this distribution. $\Delta\chi^2$ is defined as χ^2 - ${\chi^2}_{min}$ and χ^2 is defined in the equation below.

$$\chi^2(\pi_i) \equiv \sum_j \frac{(C_j^{\rm OBS} - C_j^{\rm MODEL}(\pi_i))^2}{\sigma^2(C_j)} \tag{4.1}$$

where the $C_j^{\rm OBS}$ and $C_j^{\rm MODEL}$ represents the aperture colours for our observations and model respectively. The colours are: FUV-UVW2, UVW2-UVW1, UVW2-UVW1, $u-g$, $g-r$, $g-i$, $g-z$. $\sigma^2(C_j)$ are the observational errors for the observed colours. The likelihood for each parameter π_i is calculated using a probability distribution:

$$\langle \pi_i \rangle = \frac{\int d\pi_1 \cdots d\pi_5 P(\pi)\pi_i}{\int d\pi_1 \cdots d\pi_5 P(\pi)} \tag{4.2}$$

These priors are the parameters stated in Table.4.1 and are considered "flat" as they have equal weighting i.e. the priors only inform the analysis about the allowed range of the parameters.

4.4.2 Star Formation History

First we demonstrate that the choice of star formation history (SFH) does not affect the outcome of our modelling significantly by finding for M82 the variance in the likelihood value of B using a single star-burst (1SSP), a double star-burst (2SSP) and an exponential decay (EXP) SFH. Fig.4.2 shows that the difference in the B value is insignificant when changing the SFH contained in the SPS model.

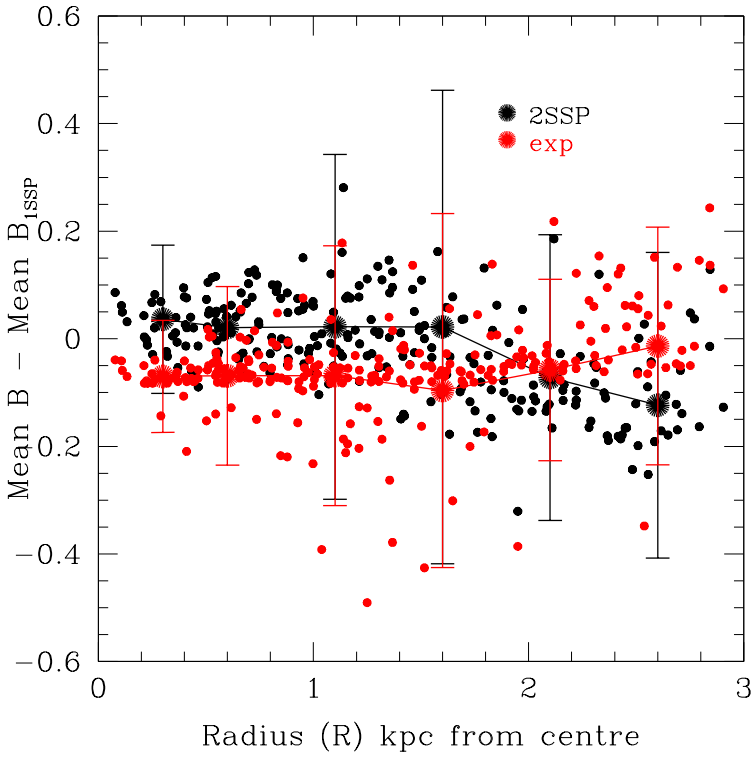

Figure 4.2: The variance in the B dust bump value at each aperture point for M82 using the single burst (1SSP), double burst (2SSP) and exponential decay (EXP) is very small hence confirming that the SFH does not affect the dust attenuation profile over the λ range of the NUV dust "Bump" significantly. The red filled circles are the (Mean B_{1SSP} - Mean B_{EXP}) SFH scenario and the black filled circles are for the (Mean B_{1SSP} - Mean B_{2SSP}) scenario. Binned at galacto-centric radial distances.

4.5 Calibration with Simulated Data

In order to prove that the method that derives the dust properties from photometry is robust and does not include any significant systematic, we apply the same methodology to a set of simulated data. Using the simulated measurements and the same grid of stellar population synthesis models we marginalise the dust parameters R_V, E(B-V) and B as we did for our observed galaxy data points. Fig.4.3 shows a direct comparison between the input (observed) and output (simulated) parameters

Table 4.2: Corrections to the data, derived from simulations. Col. 1 gives the parameter (π), cols. 2 and 3 are the slope and intercept of the correction.

$\pi_{TRUE} = \alpha\ \pi_{OBS} + \beta$		
π	α	β
R_v	1.030203	-0.292036
B	1.032269	-0.111693
E(B-V)	1.027146	-0.104647

including a 1:1 reference line. Each data point represents a set of 1,000 simulations where the adopted star formation history is a simple stellar population (1SSP, top); an exponentially decaying star formation rate (EXP, middle) or a two-burst scenario (2SSP, bottom). The large black filled circles and corresponding error bars are median and RMS values respectively, binned with respect to the input parameter at a constant number of data points per bin. The resulting corrections to the data can be seen in Table.4.2 derived from our simulations. Col.1 gives the parameter (π) and col.2 and 3 are the slope and intercept of the correction respectively. The difference between the observed and simulated data expressed as a fraction of the uncertainty can be seen along with the trend of the retrieved dust parameters with the age and metallicity derived from the same likelihood function in equation 4.2. They show there is no significant bias in the dust parameters with respect to the underlying stellar populations.

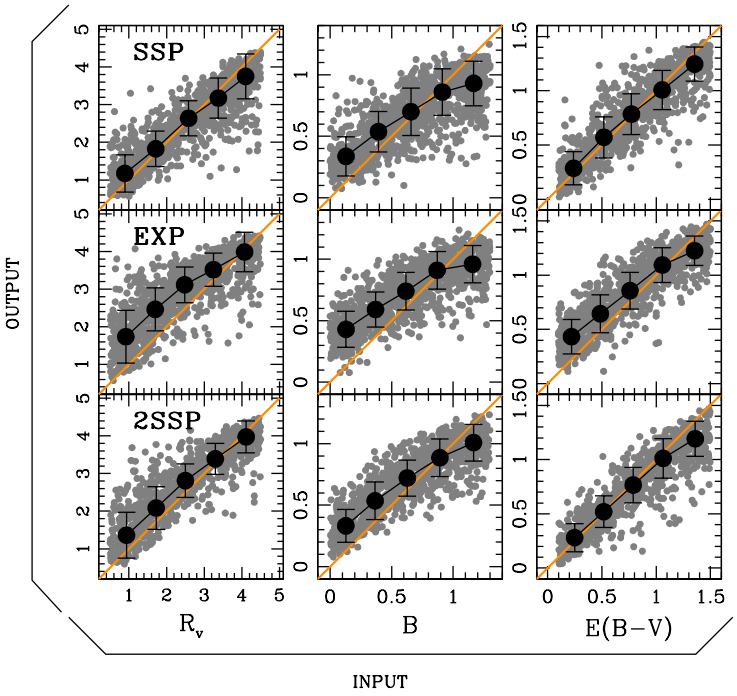

Figure 4.3: (Hutton et al., 2015) The direct comparison between the input (observed) and output (simulated) parameters. Each data point represents a set of 1,000 simulations where the adopted star formation history is a simple stellar population (1SSP, top); an exponentially decaying star formation rate (EXP, middle) or a two-burst scenario (2SSP, bottom). The grey filled circles are the individual results, whereas the large black filled circles and error bars are median and RMS values, binned at galacto-centric distance. The solid black line is the uncorrected (observed) trend and the red line is the 1:1 line.

4.6 Radial profiles of B, R_V and E(B-V)

We have shown that we do not add bias to our modelling by using a single starburst star formation history (1SSP) and we have also calibrated our data using a simulated galaxy. We now constrain our mean B, R_V and E(B-V) values at galacto-centric distances and plot our data points with the simulated data corrections. We show the corrected and the uncorrected data by finding the mean values at galacto-centric distances in order to see the profile of these parameters more

clearly.

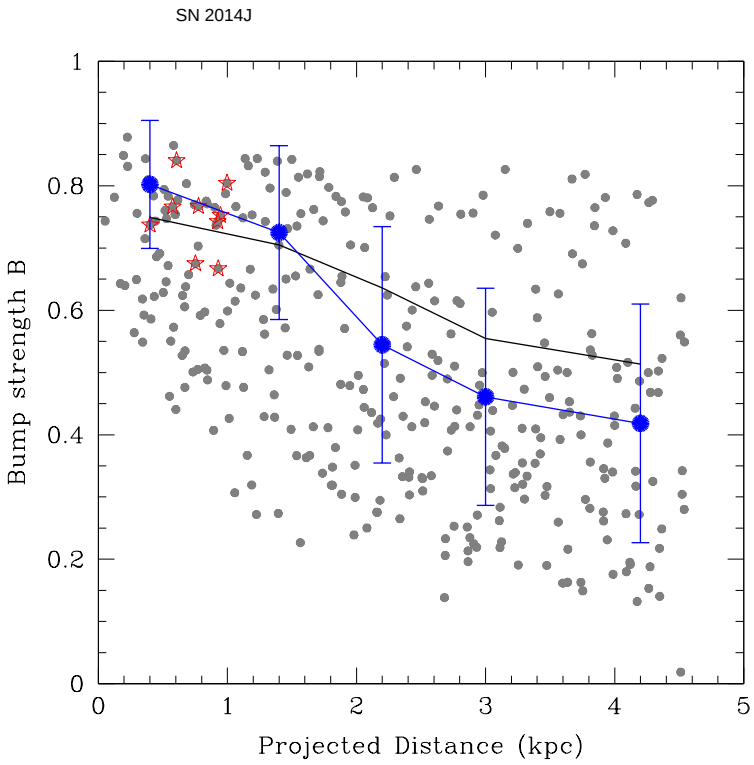

Figure 4.4: The strength of 2175Å dust bump B shown at galacto-centric distances for M82 using the FUV and NUV wavebands only. B decreases with radial distance. The red stars are the measurements within 30 arcsec (i.e. 480pc) of the position of SN2014J. The blue dots and error bars are the median and root mean square values of the data, binned at radial distance. The black line shows the same result if the retrieved parameters are not calibrated with respect to the simulations (see Table 4.2).

4.7 The Attenuation Law of M82

The radial profile of the three extinction related parameters B (NUV Bump strength), E(B-V) (colour excess) and R_V (total-to-selective extinction ratio) can be seen in Fig.4.4, Fig.4.5 and Fig.4.6 respectively for M82.

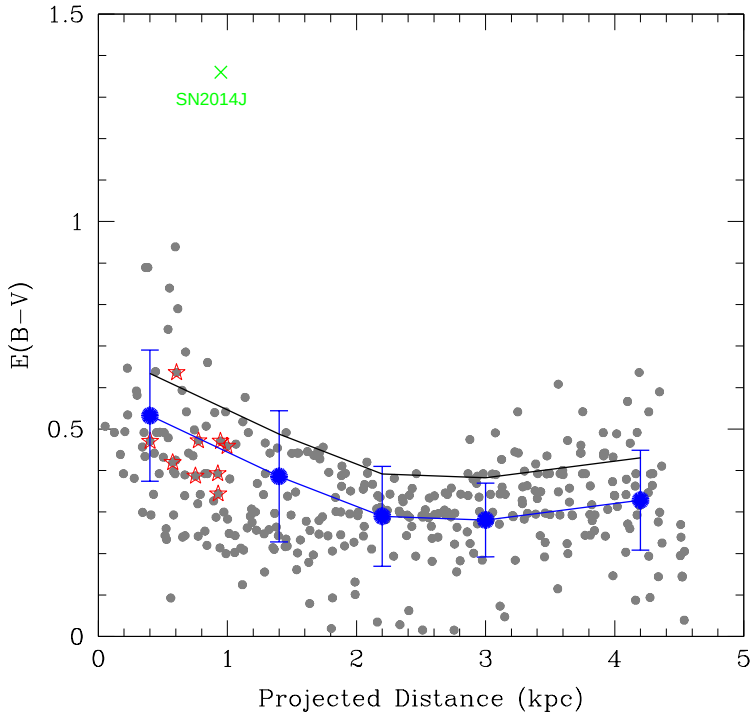

Figure 4.5: The blue filled circles are the colour excess E(B-V) (amount of dust) binned at galacto-centric distances for M82 for FUV, NUV and Optical wavebands. E(B-V) decreases towards the outer regions of the galaxy, suggesting a higher dust content close to the central, star-bursting nucleus. The green cross corresponds to the measurement in the region of SN2014J after the event (Amanullah et al., 2014). The rest of the symbols are the same as in Fig.4.4

Note that in all three figures there is a significant trend with radial distance. In the central regions of the galaxy the profile shows $B \approx 1$ and $R_V \approx 3.1$ which is the standard values of the Milky Way (i.e. a Fitzpatrick dust law). Note that variations of the dust parameters could be due to projection effects of the outer areas and the star-bursting nucleus. As we move out from the central regions, it can be seen that the B value reduces significantly as does the R_V value although we never find measurements compatible with a weak or non-existent bump. Also the colour excess E(B-V) varies with galacto-centric distance but this trend is more closely related to metallicity and star formation history. However in the previous

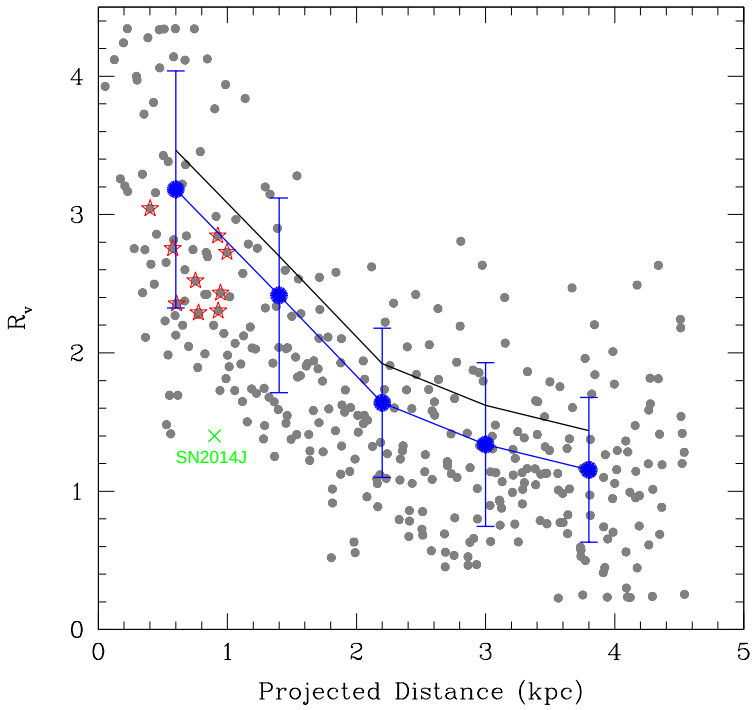

Figure 4.6: The blue filled circles are the ratio of total-to-selective extinction R_V binned at galacto-centric distances for M82 for FUV, NUV and optical photometry. R_V decreases radially outwards. The difference in R_V between the central region and the outskirts suggests a significantly different type of dust. The green cross corresponds to the measurement in the region of SN2014J after the event (Amanullah et al., 2014). The rest of the symbols are the same as in Fig.4.4.

section we show that there is no bias caused by the inherent radial trend in age and metallicity found in galaxies. Therefore these trends are intrinsic radial variations of these effective dust parameters.

Fig.4.7 shows how the three dust parameters correlate. The range of values do compare with the average estimates for samples of nearby galaxies from Conroy et al. (2010a) of B=0.8 and R_V=2.0 and also from Burgarella et al. (2005) for B=0.5 to 0.6, which are all weaker than the Milky Way standard. There is a

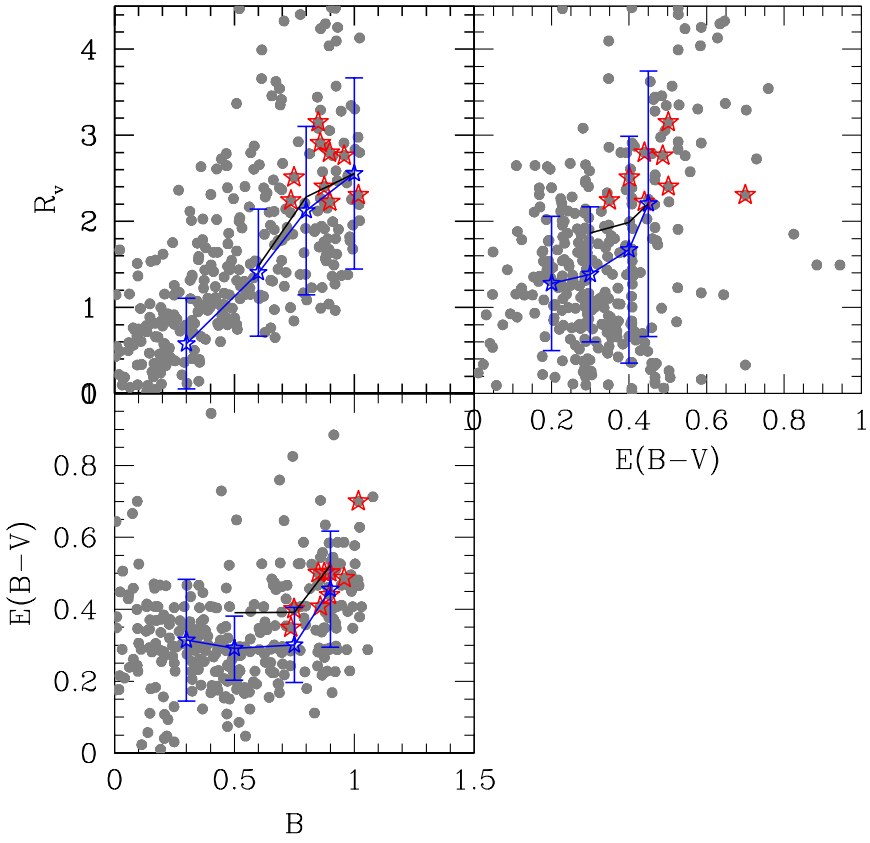

Figure 4.7: The correlation between the dust attenuation parameters: B shown in the left panel; R_V in the right panel with the colour excess E(B-V) in the top right panel, for each photometric data point for M82. The symbols are the same as in Fig.4.4

strong trend between the total-selective extinction value (R_V) and the dust "bump" strength B (top left panel) implying that the overall size of the dust grain (larger grains mean higher R_V) increases with increasing value of B. Although changes in the age-dependent extinction of the stellar/dust components can cause changes in the attenuation law our study of M82 would suggest that the variations are indeed due to the intrinsic extinction law. The bottom left panel shows that the regions with the highest reddening i.e. E(B-V)>0.5 (higher dust content) have the highest bump strength B, but the low dust content regions have a broad range of B values.

Finally (top right panel) shows a trend for regions of higher reddening towards higher R_V values i.e. bigger dust grains.

4.8 Probing the ISM around SN2014J in the pre-supernova phase

The data set we use is ideal for exploring the region around the recent SN2014J before the event. The red stars in Fig.4.4, Fig.4.5 and Fig.4.6 show the data points at distances within 480pc (30 arcsec) from where the SN2014J was (Amanullah et al., 2014). Here we can see that the R_V values are higher than $R_V = 1.4 \pm 0.1$ (Amanullah et al., 2014) however it has been found that in general environments that favour Type Ia SNe tend to have lower R_V (Burns et al., 2014), but this dispersion is quite large (Amanullah et al., 2015). These studies, based on photometric measurements of the supernova, may have a systematic because of the assumption of a well-defined template for the colours of similar types of supernova.

Taking all this into account we can not show that after the supernova the dust properties in this region are compatible with the dust properties before the event. However using our results we can say that pre-SN2014J the region around it shows similar dust properties to the Milky Way. Therefore post-SN2014J the observations should be explained by a combination both from dust in the ISM surrounding the supernova and the contribution from the interstellar disc (Foley et al., 2014) or by a significant change in the ISM towards the observed region.

4.9 Are the M82 dust properties different than other galaxies?

The trends with the attenuation law (steeper law hence lower R_V) in the central regions of M82 shown in this Chapter do not fit with recent results for the MW, M31 and Andromeda galaxy (Nataf et al., 2013), (Nishiyama et al., 2009) and (Dong et al., 2014) respectively. i.e. $R_V \approx$ 2.5 (using optical & NIR) in the inner MW galaxy towards the galactic bulge : $R_V \approx$1.56 to 2.01 (using 5.8μm & 3.6μm from *SST/IRAC*) in the galactic centre of M31: $R_V \approx$ 2.4 - 2.5 (using mid UV to NIR) for extinction clumps in the Andromeda galaxy. The difference could be because M82 is a strong starburst galaxy and therefore this starburst will affect the properties of its dusty ISM. Also its edge-on orientation provides us with a complex interpretation of the results towards small projected galacto-centric radii.

Also we find a correlation with R_V and the bump strength B but Kriek & Conroy (2013) suggest an opposite trend in high redshift galaxies and Fitzpatrick & Massa (2007) don't find a trend at all in the MW. However we have a large scatter therefore it is still unclear if this correlation is to be expected.

We have shown that there is no bias when we correlate the dust parameters using our methodology and it also needs to be pointed out that we explore the internal variations within the same galaxy rather than showing trends among galaxies (Kriek & Conroy, 2013).

4.10 Conclusion

We continue our investigation from the previous chapter (Hutton et al., 2014) by analysing further the dust attenuation in M82. We confirm our previous finding that the central region of M82 favours a Fitzpatrick type attenuation law (containing a 2175 Å dust bump) rather than a Calzetti type law (no bump) and we quantify the strength of the dust bump B and the total-to-selective attenuation ratio R_V at galacto-centric distances. We also constrain the colour excess E(B-V) to estimate the amount of dust in M82. We assume that dust only contributes as a foreground screen (one-zone model). However, changing the geometry of the dust distribution can cause variations in the dust parameters presented here (Witt & Gordon, 2000).

We find a significant B gradient with projected galacto-centric distance (see Fig.4.4). In the central regions we show a strong bump ($B \approx 1$) i.e. a Fitzpatrick law and as we go away from the centre, where there is less dust, we see a declining B value and steeper R_V which is characteristic of a smaller dust grain size distribution, effectively tending towards the standard attenuation law of the SMC (Pei, 1992). This change in the B value indicates a change in the dust properties (Gordon et al., 1997), although an age dependent law can produce similar effects (Panuzzo et al., 2007). Older stellar populations would make the observed colours redder in the outer regions which would manifest in a higher amount of dust content i.e.E(B-V) however we do not see this, in fact in Fig.4.5 you see the opposite trend. We also prove that the underlying stellar populations can be factored out by using simulated data, therefore allowing us to constrain the NUV bump and R_V.

As our data was taken before the recent type Ia supernova SN2014J in M82 we are able to probe the properties of the dust in the ISM around the supernova before the event and we find a standard dust component with $R_V \approx 3$ and $B \approx 1$. Therefore the recent measurement with lower values of R_V reflect either the presence of a circum-stellar component or a significant change in the dust properties before and after the supernova around the supernova position.

Chapter 5

Investigation of the dust "Bump" in nearby Galaxies.

5.1 Introduction

Whilst studying the stellar populations and dust in M82 we find something we did not expect; the Milky Way Fitzpatrick dust model (Fitzpatrick, 1999b) fitted better than the star-burst Calzetti dust model (Calzetti, 2001b) especially in M82s central regions. In this last Chapter we quantify the strength of the 2175$\mathring{A}$ dust bump for 6 nearby galaxies. The dust bump appears in the Fitzpatrick dust model but not in the Calzetti model and is one of the fundamental differences between the two laws. We investigate whether the trends we see in the previous chapter for M82s attenuation parameters are unique to M82. M82 is different from the other galaxies in our survey because it has a strong galactic wind and has also had a recent interaction with M81 causing a starburst due to tidal effects.

The additional galaxies we study in this Chapter are nearby "normal" galaxies M81, M51, M77, M100 and M101. These galaxies are grand-design spirals and appear face-on therefore simplifying projection effects. They are not starburst galaxies, having instead star formation rates similar to the Milky Way. More detail about these galaxies can be found in Chapter 1.

Kriek & Conroy (2013) shows that the MW and Calzetti dust laws provide poor fits with UV wavelengths for nearly all SEDs for galaxies $0.5<z<2.0$ and they found that there is a strong correlation with the dust slope and UV bump strength, with the stronger bumps having steeper dust laws. It was also found that galaxies that have higher star formation rates have weaker bumps and shallower dust curves. A variation with inclination was also detected as would be expected as the line of sight would transverse a higher column density than in a face-on galaxy. It was hypothesised that these observed correlations may reflect the distribution of grain sizes (Kriek & Conroy, 2013). Hutton et al. (2015) show that M82 best fits a Fitzpatrick dust profile with a dust bump strength varying at galacto-centric distances. Similarly Hoversten et al. (2011) found that M81 and Holmberg IX (tidal dwarf) are also best fit by a MW dust extinction law with a prominent 2175 Åbump.

5.2 The Data

We use the same data as in Chapter 2 but now we extend it to the galaxies in our survey. We chose our galaxies because they are "nearby" and hence allow us to observe them at high spatial resolution and they also have the required archived

photometry in UV and the optical. We use NUV and optical photometry only.

We use NUV from the UVOT instrument onboard the *Swift* telescope. The UVOT provides us with three NUV passbands, UVW2, UVM2, UVW1 with the significance here being the UVM2 filter as it straddles the 2175$\mathring{A}$ dust bump. The optical photometry is from the SDSS DR8 archives with wavebands *u,g,r,i,z*. The colours we use in our modelling are W2-M2, W2-W1, u-g, g-r, g-i, g-z. We reduce the photometry in the same way as we did for M82, hence convolving the optical to match the NUV PSF. The corresponding FITS images for our galaxies can been seen in the RGB images in Fig.5.1. The green is the optical filter *g*, red is optical filter *z* and the blue is the UV filter *UVW2*. They are all bright in the optical with some spots of UV (massive stars) showing through the diffuse optical light especially in the spiral arms of M100 and reflected light in M82s galactic wind (Hutton et al., 2014).

5.3 Attenuation Law

As previously we use our optical and UV photometry with stellar population synthesis (SPS) adopting the Charlot and Bruzual model (Bruzual & Charlot, 2003) with a well chosen dust law to discover more about the dust in nearby galaxies. We again use Conroy's dust law (Conroy et al., 2010a) which contains the extra variable B to define the strength of the 2175$\mathring{A}$ dust "bump" B and adopt the same process to constrain the dust attenuation parameters for our galaxies. We marginalise the other *nuisance* parameters (metallicity & age) and for B we also marginalise R_V

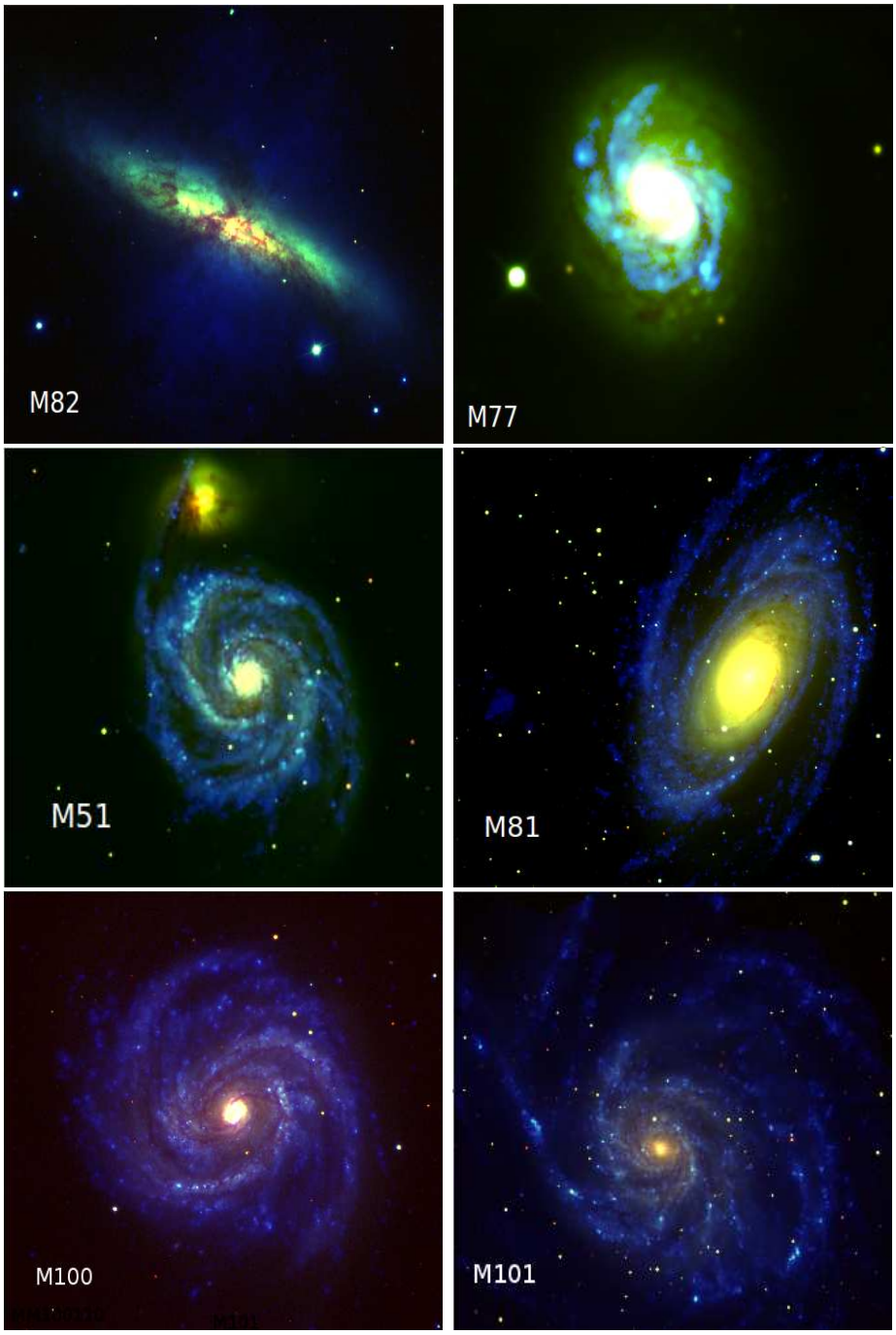

Figure 5.1: RGB images of our galaxies taken from our .fits files. The green is the optical filter *g*, red is optical filter *z* and the blue is the UV filter *UVW2*. As you can see they are all bright in the optical with extremely bright centres and some spots of UV (brighter stars) showing through the diffuse optical light. For M82 you can see the UV light reflected by dust in its super-wind.

(total-to-selective extinction variable) and E(B-V) colour excess; for R_V we also marginalise B and E(B-V); for E(B-V) we also marginalise R_V and B. We calculate these values at galacto-centric distances for all our galaxies. Note that in Chapter 4 we showed through simulations that these nuisance parameters can be marginalised obtaining unbiased estimates of B, R_V and E(B-V)

5.4 2175$\AA$ dust bump B radial profile.

We restrict the analysis to NUV photometry to calculate B as the dust bump we are observing occurs at 2175$\AA$ hence only the UV bands straddle this feature and therefore the optical wavelengths would only serve to "wash out" the effects of the bump in our models. As before we calculate the best fit B values and we bin these radially and the mean values of these bins are plotted with their corresponding error bars (red filled circles) together with the best fit B values (grey filled circles) for each aperture. In order to perform a consistent comparison of the dust properties in these galaxies and M82, we follow the same methodology as in Chapter 4, but this time we do not apply the corrections with respect to the simulations, as those took into account the FUV data from GALEX. Fig.5.2 shows the resulting radial trends for B for each of our galaxies with galaxy data points and mean binned values plotted.

Fig.5.3 shows how B varies in each of the galaxies by comparing the trend with the mean binned values. The left panel shows how M82 and M77 vary and the right panel shows how the remaining galaxies vary. We can see that M82 and M77 galaxy

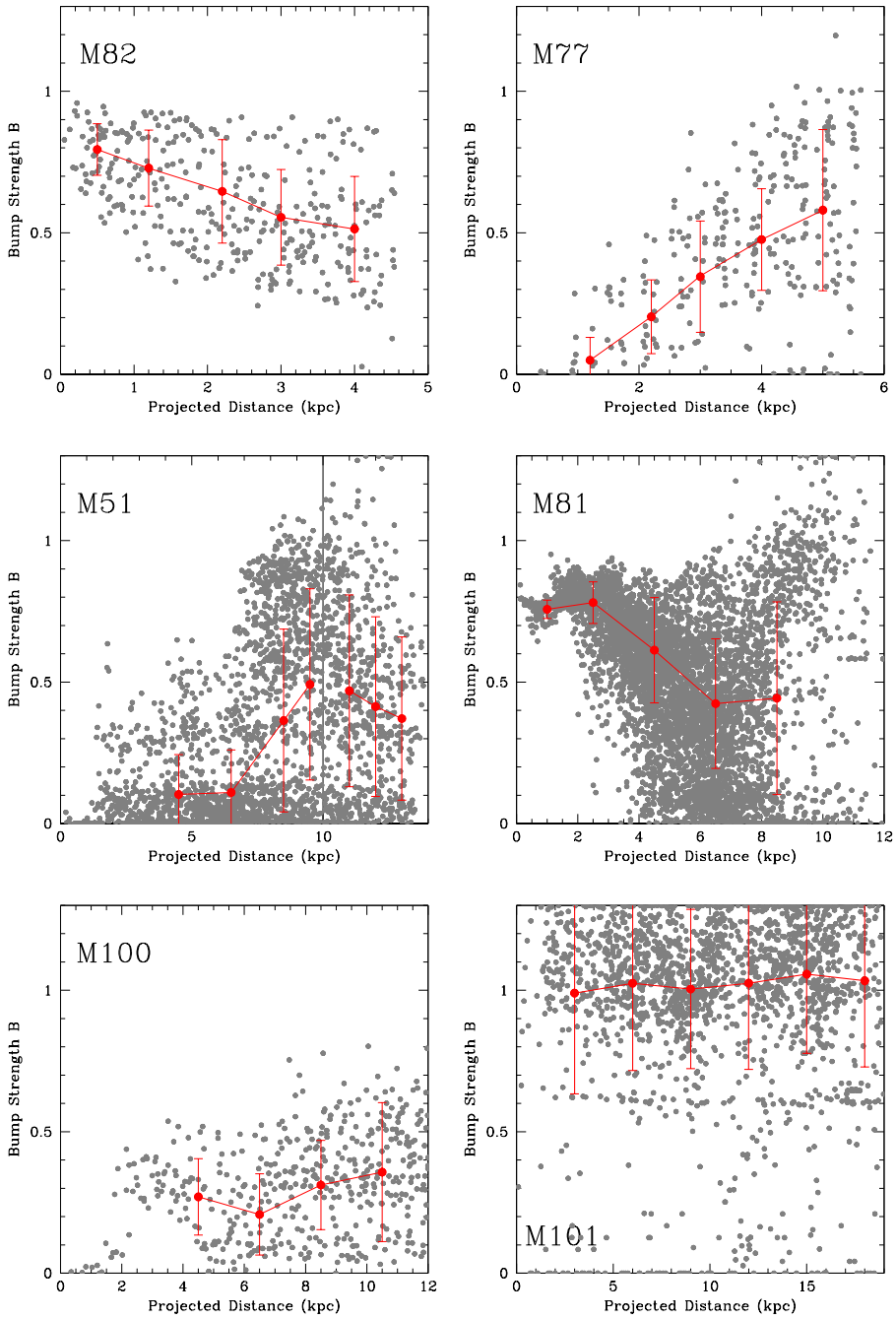

Figure 5.2: These plots show the strength of the 2175$\mathring{A}$ dust bump (mean B value) at projected galacto-centric distances (binned) for each galaxy. We use just UV photometry. The best fit B values are grey filled circles and the corresponding mean binned values are the larger red filled circles with error bars.

profiles behave almost as opposites to each other. In M82 the B value decreases radially from ≈0.7 to ≈0.5 whereas M77 increases from almost a Calzetti profile B=0 to ≈0.7 implying that the range (chemical composition and shape) of dust particles may be different in each galaxy but both galaxies show a radial change in dust. We also expect the dustier star forming regions to attenuate light differently to the regions with lower star formation rates. However comparing the remaining galaxy profiles we can see that B generally increases or remains static between the galactic centre and the outer part of the galaxy for all galaxies except M82 and M100.

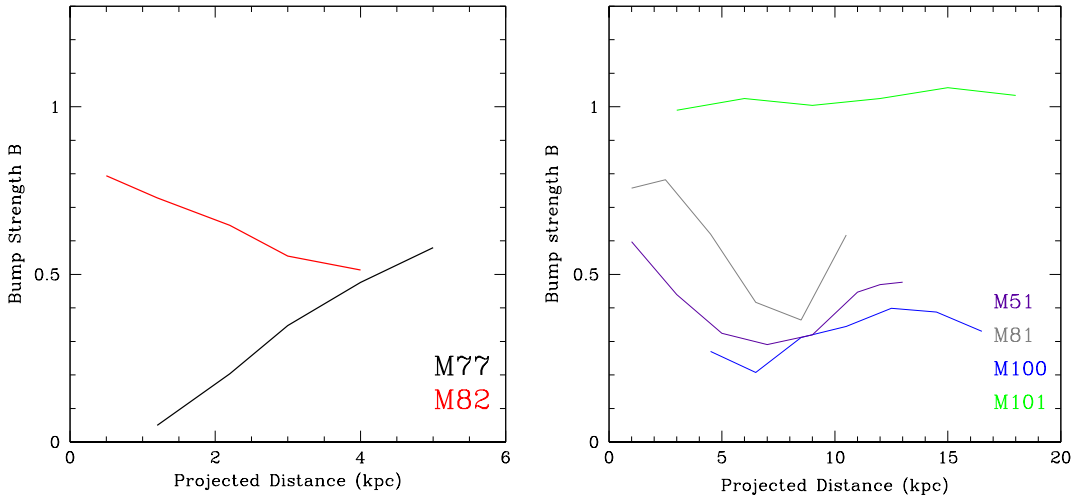

Figure 5.3: The left panel shows how B varies in M82 and M77 at the same projected galacto-centric distances plotting just the profile line. The right panel shows how B varies in the other galaxies at same galacto-centric distances. Using same photometry as Fig.5.2 but only plotting the line through each mean point.

5.5 R_V radial profile

R_V is the total to selective extinction and as we do for B we show how the radial profiles for this attenuation parameter differ for our six galaxies. However we use both the UV and optical data this time to calculate R_V as the attenuation is effective throughout these wavebands. We calculate the mean value of R_V in the same way except we marginalise over B instead of R_V and again we do not adjust our values using simulated data. The radial trends we have seen for R_V in the central regions of M82 do not fit with recents results for the MW (Nataf et al., 2013), M31 (Nishiyama et al., 2009) and the Andromeda galaxy (Dong et al., 2014). So it will be interesting to see if M82 is unique in the sample of galaxies we have chosen.

Fig.5.4 and Fig.5.5 show how the mean values of R_V vary, presented in the same way as the previous plots for B. M82's profile behaves differently to the rest of the galaxies whose profiles tend to rise and then fall whereas M82's just has an almost linear decline. This indicates that the size in the dust grain changes with radial distance.

5.6 Colour excess E(B-V) radial profiles

E(B-V) is the colour excess. Once the attenuation law is fixed (by fixing the parameters R_V and B), E(B-V) can be considered a proxy of the amount of dust. We calculate the mean best fit values for E(B-V) at radial distances for our six galaxies as we have done for B and R_V. We use both the UV and optical data to calculate E(B-V) as this parameter is effective over these wavebands. We do not

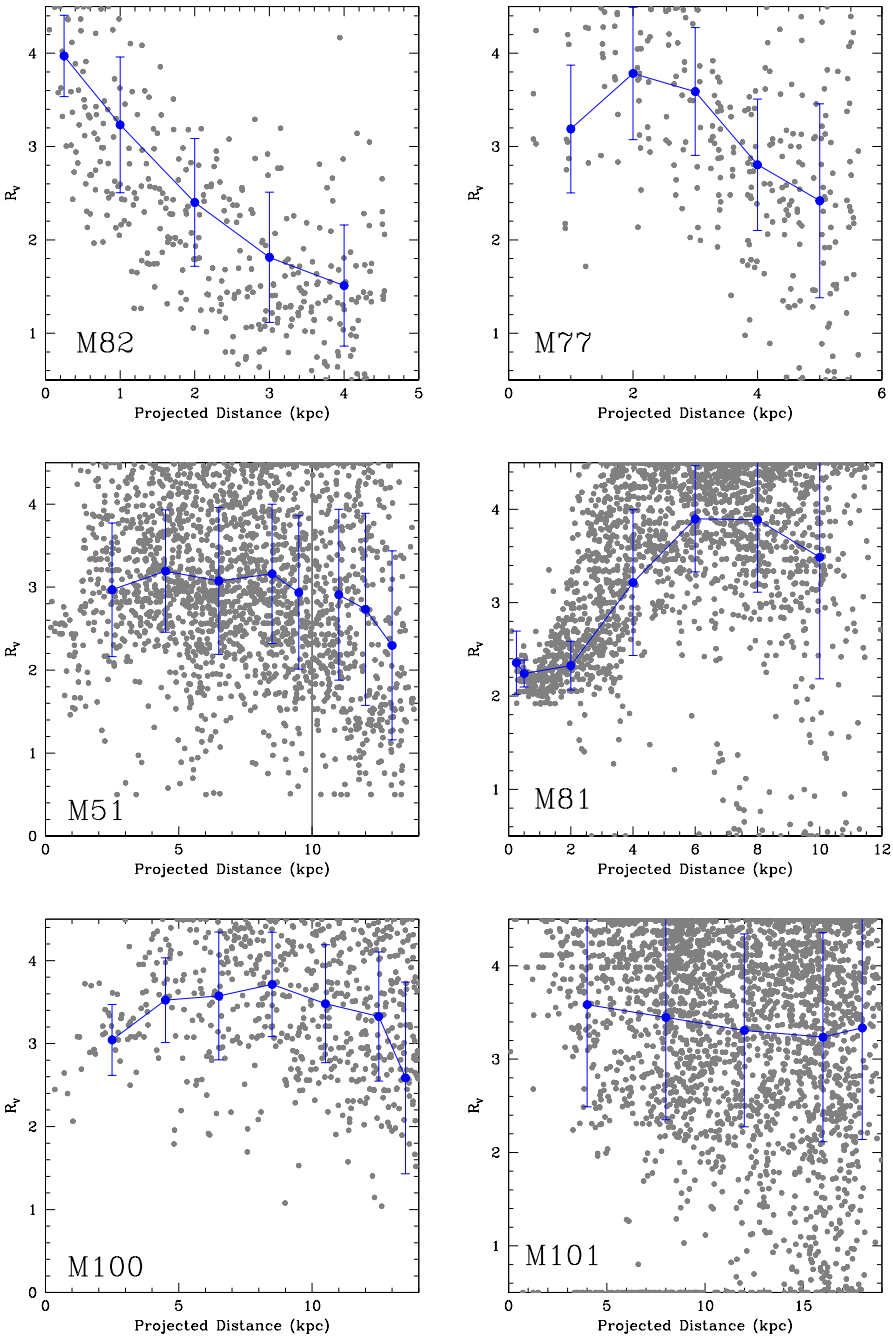

Figure 5.4: These plots show how R_V varies at galacto-centric distances by galaxy. The black vertical line for M51 at 10kpc shows the separation point between the galaxy and the tidal dwarf M51b. The best fit R_V values are grey filled circles and the corresponding mean binned values are the larger blue filled circles with error bars. We use both UV and optical photometry.

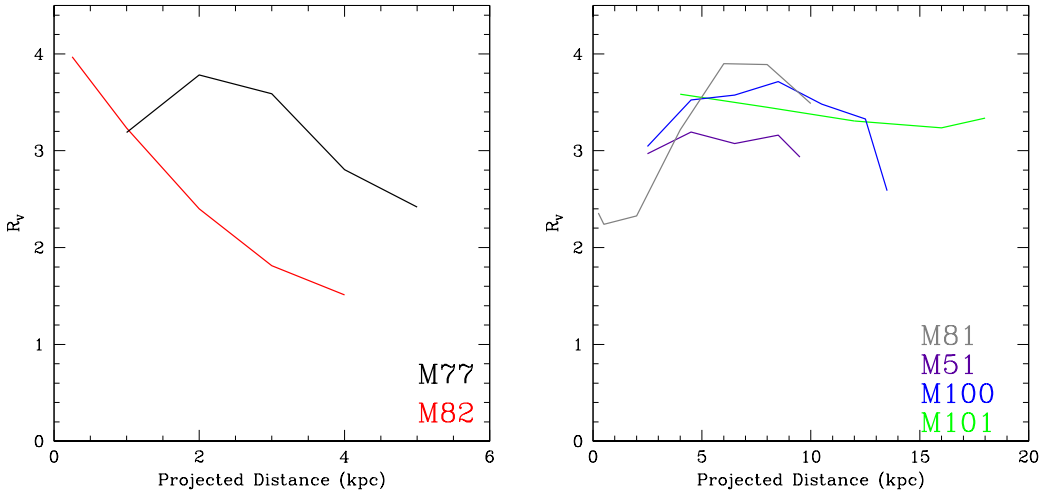

Figure 5.5: The left panel shows how the attenuation parameter R_V varies for M82 and M77 at the same projected galacto-centric distances plotting just the profile line. The right panel shows how the remaining galaxies vary. Colour coding is the same as in Fig. 5.3.

adjust our values using simulated data. Fig.5.6 and Fig.5.7 show the corresponding radial profiles. These plots show that all the galaxies behave similarly at radial distances for E(B-V) possibly reflecting a radial trend between dust content and metallicity.

5.7 Relationship between R_V, E(B-V) & B

Finally we investigate the relationship between all three parameters for each galaxy (Fig.5.8). When calculating the mean values for M51 we use only the photometry at radial distances R<10kpc so as not include the M51b dwarf galaxy photometry in our data. We have included for reference only the points >10kpc as light grey filled circles. In general we would not expect to see a correlation between the B bump, colour excess E(B-V) and R_V as they all measure different aspects of the dust attenuation and quantity as they represent different aspects of the dust. R_V

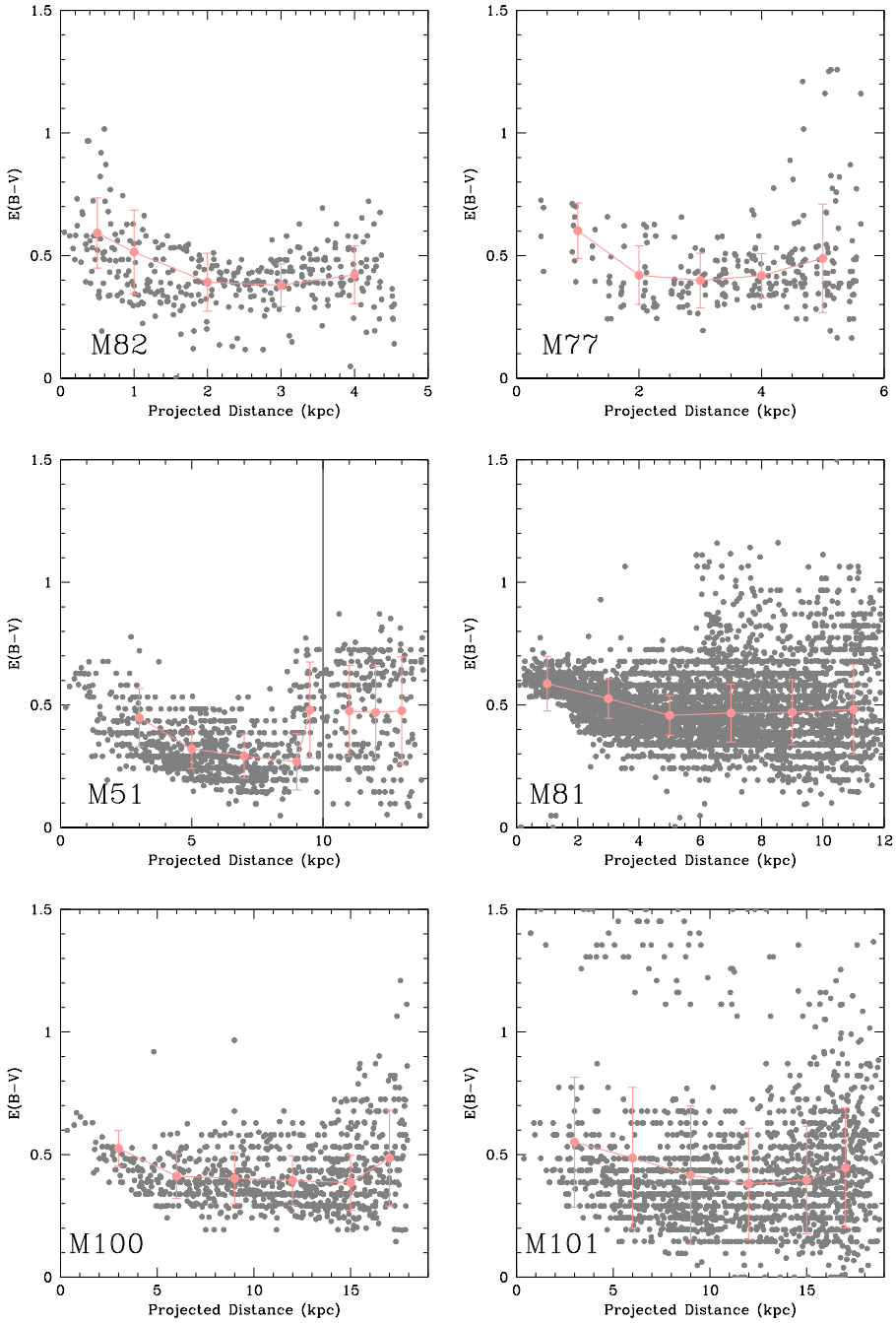

Figure 5.6: These plots show how E(B-V) varies at galacto-centric distances for each galaxy. The black vertical line for M51 at 10kpc shows the separation point between the galaxy and its tidal dwarf M51b. The best fit E(B-V) values are grey filled circles and the corresponding mean binned values are the larger blue filled circles with error bars. We use both UV and optical photometry.

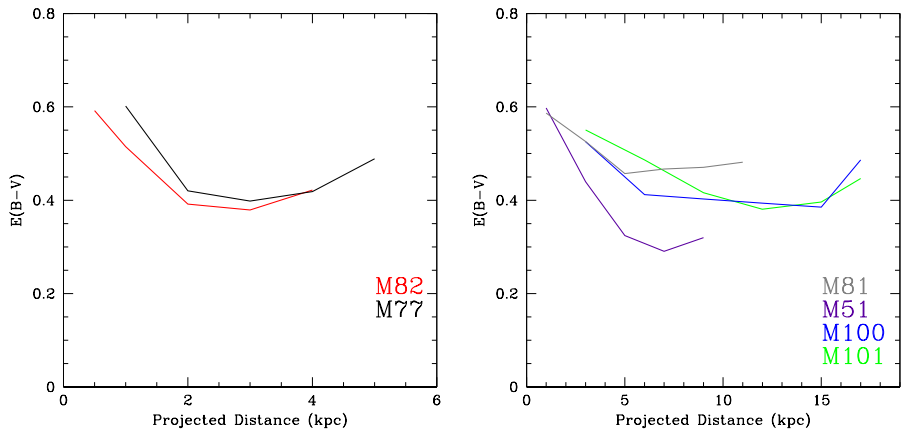

Figure 5.7: The left panel shows how the colour excess (amount of dust) E(B-V) in M82 varies with M77 at the same projected galacto-centric distances plotting just the profile line. The right panel shows how the rest of the galaxies vary. Colour coding is the same as in Fig.5.3.

can indicate a varying grain type and size, E(B-V) the quantity of dust and B the strength of the 2175$\mathring{A}$ dust bump which is possibly related to the presence of graphite or PAH-related dust.

It can be seen that indeed M82 (blue line) does behave in a unique fashion in the plots R_V vs B and R_V vs E(B-V). M82 stands out from the group with M101 also giving a different trend with respect to the other four galaxies in this study.

5.8 Conclusions

We can see that in general dust attenuation does behave differently in M82 than in the other five galaxies we study. The attenuation profile for B decreases with increasing radial distance for M82 where in general it increases or is flat in the other galaxies (apart from M81). Therefore the other galaxies tend towards a more MW type profile as we move further out from their centre and M82 shows a more MW type profile as we move towards its centre (M101 displays a MW profile throughout).

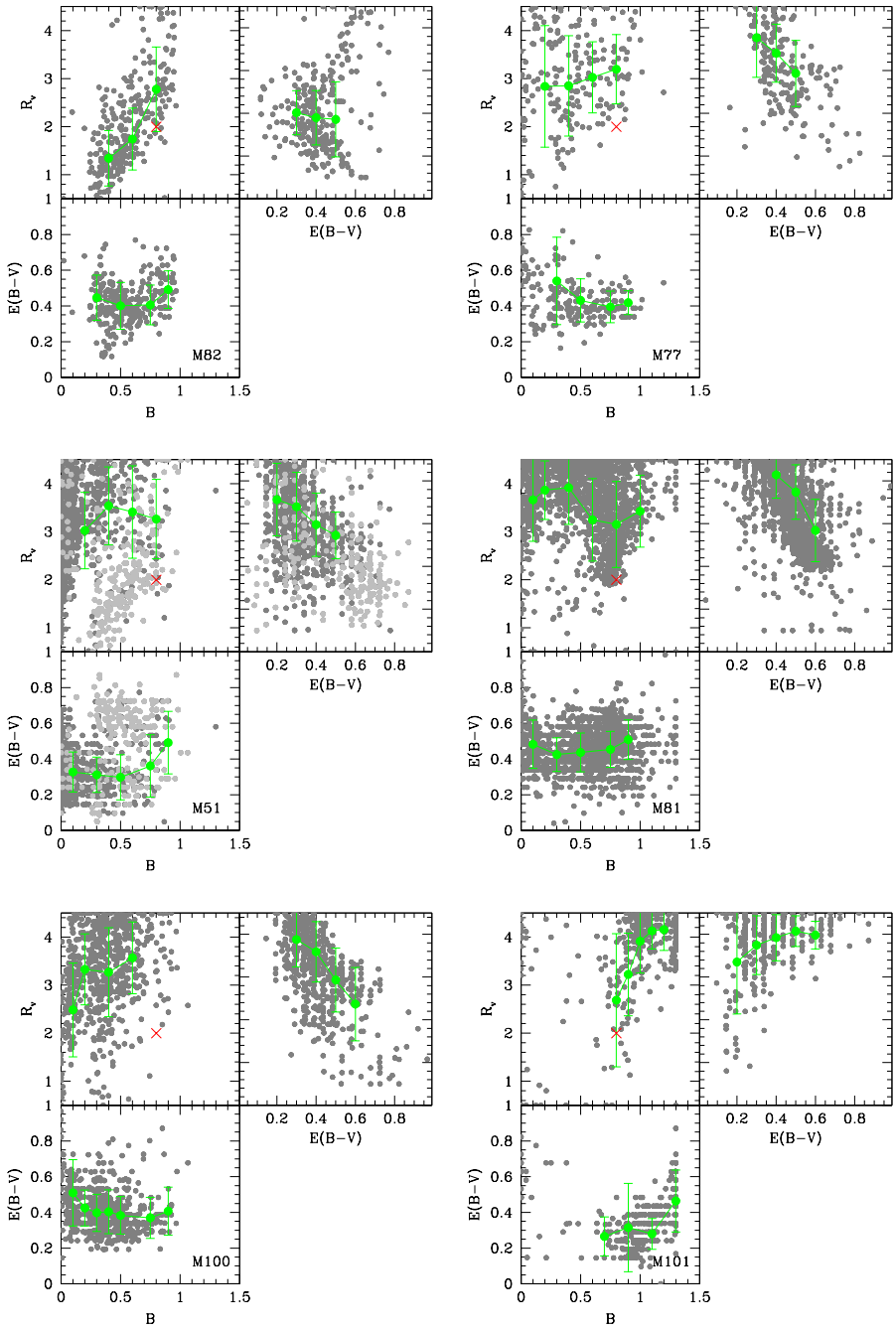

Figure 5.8: Plots to show how B, R_V and E(B-V) vary with each other for each aperture in our galaxies using the same data as shown in our previous figures. The best fit values are dark grey filled circles and the corresponding mean binned values are the larger green filled circles with error bars. For M51 those points >10kpc are not included in our calculation of the mean values. Data points <10kpc are shown as dark grey filled circles

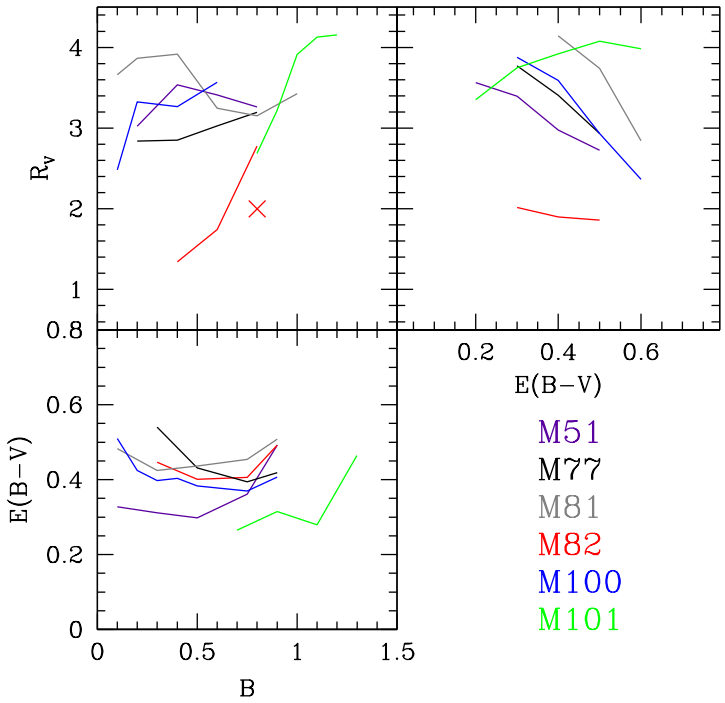

Figure 5.9: Here can see more clearly how B, R_V and E(B-V) vary with each other for M82 and M77 at the same projected galacto-centric distances as we have just plotted the profile lines. Colour coding is the same as in Fig.5.3.

M82 shows a linear decline in R_V as we move further from its centre but the other galaxies show an initial increase followed by a decrease (apart from M81, where R_V increases with increasing radial distance). This result shows the change in the size of the dust grain behaves differently for M82 at radial distances than for the other galaxies.

Colour excess E(B-V) behaves similarly for all galaxies implying there may be more dust in the galaxy centre than in the outer regions. This could be due to all galaxies having a radial decrease in metallicity.

The methodology we adopt in this chapter has also been proven successful with high redshift galaxies (Kriek & Conroy, 2013) which shows a dust bump strength for these galaxies of B=0.25 (i.e. ≈25% of the MW bump). Finding the attenuation profiles of these higher redshift galaxies allows us to probe the evolution effects of dust. Conroy et al. (2010a) find as best fit an average SMC extinction curve with R_V≈2.0 and a bump strength of 80% in a sample of low-redshift, disk-dominated star-forming galaxies. In our case, apart from M82 all our best fit R_V values are higher than 2.0. Note that we make resolved measurements within a set of nearby galaxies, whereas Conroy et al. (2010a) consider integrated measurements.

We conclude that the attenuation law related to dust absorption and scattering has a complex dependence on the different processes leading to the formation of galaxies. Local details of these processes can affect the resulting dust law. In our sample of nearby galaxies, the radial dependence of the dust-related parameters has a large amount of variation, with the colour excess being the only one with a clearer connection with the radial decrease of metallicity. The values of R_V are mostly high (around 3), i.e. close to the value for a Milky-Way law. M82 is the only galaxy that shows a significant radial decrease, with low values of R_V(≈1) in the outer regions. As regards to correlations between these parameters, different trends are seen in different galaxies. More work needs to be done to explore in detail whether differences in the star formation histories can play a significant role in shaping the attenuation law.

Chapter 6

Conclusions

6.1 Dust & Stellar Populations of M82

6.1.1 Modelling the Dust Law

There is still a lot we do not know about how galaxies form and evolve but studying star formation histories provides us with a test-bed to delve further. To see the stellar light we need to disentangle it from the dust that surrounds it, so understanding how dust behaves in a galaxy is key to unlocking the mysteries of galaxy evolution. Therefore we need to remove the effect dust has on the galactic light we want to study. Knowledge of the types, amount and distribution of dust is paramount to this study.

M82 is a well studied galaxy however using the UV/Optical Telescope (UVOT) on board the *Swift* observatory we are able to access photometry not available elsewhere. UVOT has three broadband UV filters and the middle UV filter (UVM2) straddles the 2175Å dust bump. However when using the standard starburst dust

model from (Calzetti, 2001b) we found that it did not fit with M82 especially in its central regions. We were surprised to see that the Milky Way (MW) (Fitzpatrick, 1999b) model containing the 2175Å dust bump fitted better. Therefore we decided to investigate this further.

6.1.2 B, R_V and E(B-V)

We use the Conroy et al. (2010a) dust law in our stellar population synthesis (SPS) analysis. This law contains a variable B that defines the strength of the dust bump as well as the usual R_V (total-to-selective extinction ratio) and also E(B-V) (dust content) parameters. We find the χ^2-based best fit values of these variables for M82. We know that the value of R_V depends on the size of the dust particle with respect to the wavelength of the incident light. For instance, if the dust grains are very small with respect to the wavelength (i.e. below 0.5μm for optical light) we are in the Rayleigh regime, where light scatters proportional to λ^{-4}, i.e. preferentially scattering more the bluer light. In this case, the steep dependence translates into a small value of R_V. In contrast, when the dust particles are larger than the wavelength, there is no significant dependence with wavelength (Mie scattering), resulting in a high value of R_V. The B value depends on a specific component of dust (possibly graphite or PAH-based) of the dust particle and E(B-V) depends on the amount of dust. We find that R_V and B are correlated, less so for E(B-V), which is similar to what previous research has shown. We also find that our best fit values for M82 are comparable to other published values except in the area around supernova SN2014J after the event.

6.1.3 SN2014J

As our photometry was taken before SN2014J, we are able to compare the pre-supernova environment we find from our study with published data taken after the event. We find that E(B-V) was lower before the supernova event which is to be expected as the supernova event could affect the amount of dust. From our data we also find that R_V was lower in the area before the supernova which implies larger dust grains in existence before the event. However there may be possible systematic differences that could cause the different results between the two methods (ours and recent SN2014J data).

6.1.4 Stellar Populations

Our stellar population analysis of M82 reveals a very young core ($\approx$100 Myr), large extinction (E(B-V)$\approx$0.5 mag) at projected galacto-centric distances R$<$1 kpc. In the outer regions, the galaxy has an overall homogeneous distribution of older stellar populations ($\approx$ 0.7–1 Gyr) with lower, but significant colour excess (E(B-V)$\approx$ 0.2 mag). Again these findings are in line with previous literature, including the evidence of M82s recent interaction with its neighbouring galaxy M81.

We find that the energy balance between the observed Infrared ($\lambda > 8\mu$m) emission and the UV/optical ($\lambda < 1\mu$m) energy absorbed by dust suggests that the starburst is not heavily dust-enshrouded. Therefore we can assume that we are observing all the light from the young stellar populations either in the form of UV or dust attenuated Infrared and model accordingly.

Table 6.1: Some attributes of the galaxies studied in this thesis[1].

Messier No.	Type	Inclination (deg)	Distance Mod (mag)
M82	Scd	76.9	27.79
M81	Sab	62.7	27.78
M100	SABc	23.4	31.01
M101	SABc	16.0	29.26
M51	Sbc	32.6	29.37
M77	Sb	24.1	30.02

We find that the radial gradients of the NUV and optical colours in the super-wind region support the hypothesis by Hoopes et al. (2005) that the emission in the wind cone is driven by scattering from dust grains entrained in the ejecta.

6.2 M82 Compared to Other Nearby Galaxies

M82 has a strong dust bump with B decreasing from $\approx$1 to $\approx$0.3 with galacto-centric distance, but is M82 unique or can we see similar patterns with other nearby galaxies? M82 is an unusual nearby galaxy in that it has: a galactic wind (also edge-on so it can be seen), recent tidal interactions with a nearby galaxy and a starburst with star formation rate around 10M$\odot$/yr.

The galaxies we study in this thesis are shown in Table.6.1. We test our data points (uncorrected) for M82 using a simulated galaxy (corrected) and show that

there is only a small variance between the corrected and uncorrected data. We also demonstrate that the outcome of our SPS analysis is not greatly affected when we change the star formation history (SFH) and therefore adopt a single burst model. We use the same SPS approach we adopted for M82 for all our galaxies. We find that the radial profiles for B and R_V for M82 are indeed unique as the same correlation could not be strongly identified with the other galaxies. However the radial profile for E(B-V) for M82 is also seen in all the other galaxies in our study. We know that the average R_V value for the Milky Way is 3.1 as R_V varies by sight-line and also B=1.

6.3 Future Work

Using a larger sample of nearby galaxies with UVOT and SDSS photometry we could increase the number of E(B-V) radial profiles to see if they all behave in the same way as we have found with our smaller sample. We could also compare the radial profiles of these galaxies for R_V and B to see if M82s steep linear decline at galacto-centric distances is unique.

Increasing our galaxy sample further we could explore the survey catalogues for galaxies further away i.e. as point sources, whilst still using UVOT and SDSS. For example increasing the sample size of our galaxies would allow us to obtain a more conclusive view on whether the 2175Å dust bump indeed exists, albeit with varying strengths, in all galaxies. So we can ask under what circumstances do galaxies produce the dust attenuation bump.

Then increasing our sample still further we could use the UV and optical (rest frame) photometry of higher redshift galaxies. For example for galaxies with redshift z>1.3 we could use SHARDS "Survey for High-z Absorption Red and Dead Sources" (Pérez-González et al., 2013) as it probes the rest-frame UV spectral range (210-350 nm) of galaxies at this redshift. The SHARDS dataset covers the wavelength range between 500nm and 950nm with continuous passbands.

6.4 Publications

Part of this thesis is based on refereed publications: Chapter 3 is based on Hutton et al. (2014); Chapter 4 is based on Hutton et al. (2015).

Bibliography

Aihara H. et al., 2011, ApJS, 195, 26

Amanullah R. et al., 2014, ApJL, 788, L21

Amanullah R. et al., 2015, ArXiv e-prints

Bell E. F., 2003, ApJ, 586, 794

Bigiel F., Leroy A., Walter F., 2011, in IAU Symposium, Vol. 270, Computational Star Formation, Alves J., Elmegreen B. G., Girart J. M., Trimble V., eds., pp. 327–334

Bigiel F., Leroy A., Walter F., Brinks E., de Blok W. J. G., Madore B., Thornley M. D., 2008, AJ, 136, 2846

Bradley J. et al., 2005, Science, 307, 244

Breeveld A. A. et al., 2010, MNRAS, 406, 1687

Breeveld A. A., Landsman W., Holland S. T., Roming P., Kuin N. P. M., Page M. J., 2011, 1358, 373

Bruzual G., Charlot S., 2003, MNRAS, 344, 1000

Burgarella D., Buat V., Iglesias-Páramo J., 2005, MNRAS, 360, 1413

Burns C. R. et al., 2014, ApJ, 789, 32

Calzetti D., 2001a, New A Rev., 45, 601

Calzetti D., 2001b, New A Rev., 45, 601

Chabrier G., 2003a, PASP, 115, 763

Chabrier G., 2003b, PASP, 115, 763

Conroy C., Schiminovich D., Blanton M. R., 2010a, ApJ, 718, 184

Conroy C., Schiminovich D., Blanton M. R., 2010b, ApJ, 718, 184

Dalcanton J. J. et al., 2009, ApJS, 183, 67

de La Rosa I. G., La Barbera F., Ferreras I., de Carvalho R. R., 2011, MNRAS, 418, L74

Doane J. S., Mathews W. G., 1993, ApJ, 419, 573

Dong H. et al., 2014, ApJ, 785, 136

Draine B. T., 2011, Physics of the Interstellar and Intergalactic Medium

Duley W. W., Seahra S., 1998, ApJ, 507, 874

Fitzpatrick E. L., 1999a, PASP, 111, 63

Fitzpatrick E. L., 1999b, PASP, 111, 63

Fitzpatrick E. L., Massa D., 1986a, ApJ, 307, 286

Fitzpatrick E. L., Massa D., 1986b, ApJ, 307, 286

Fitzpatrick E. L., Massa D., 1990, ApJS, 72, 163

Fitzpatrick E. L., Massa D., 2007, ApJ, 663, 320

Foley R. J. et al., 2014, MNRAS, 443, 2887

Fruchter A. S., Hook R. N., 2002, PASP, 114, 144

Gehrels N., Swift, 2004, 36, 116

Gil de Paz A. et al., 2007, ApJS, 173, 185

Gordon K. D., Calzetti D., Witt A. N., 1997, ApJ, 487, 625

Greco J. P., Martini P., Thompson T. A., 2012, ApJ, 757, 24

Hatziminaoglou E. et al., 2010, A&A, 518, L33

Heckman T. M., Armus L., Miley G. K., 1990, ApJS, 74, 833

Hoopes C. G. et al., 2005, ApJL, 619, L99

Hoversten E. A., Glazebrook K., 2008, ApJ, 675, 163

Hoversten E. A. et al., 2011, AJ, 141, 205

Humphreys R. M., Strecker D. W., Ney E. P., 1972, ApJ, 172, 75

Hutton S., Ferreras I., Wu K., Kuin P., Breeveld A., Yershov V., Cropper M., Page M., 2014, MNRAS, 440, 150

Hutton S., Ferreras I., Yershov V., 2015, ArXiv e-prints

Kennicutt, Jr. R. C., 1998a, ARA&A, 36, 189

Kennicutt, Jr. R. C., 1998b, ApJ, 498, 541

Kennicutt, Jr. R. C. et al., 2003, PASP, 115, 928

Kobulnicky H. A., Johnson K. E., 1999, ApJ, 527, 154

Kriek M., Conroy C., 2013, ApJL, 775, L16

Kroupa P., 2001, MNRAS, 322, 231

Larkin J. E., Graham J. R., Matthews K., Soifer B. T., Beckwith S., Herbst T. M., Quillen A. C., 1994, ApJ, 420, 159

Lee J. C. et al., 2009, ApJ, 706, 599

Lehnert M. D., Heckman T. M., 1996, ApJ, 472, 546

Lehnert M. D., Heckman T. M., Weaver K. A., 1999, ApJ, 523, 575

Lonsdale C. et al., 2004, ApJS, 154, 54

Lynds C. R., Sandage A. R., 1963, AJ, 68, 284

Mac Low M.-M., Ferrara A., 1999, ApJ, 513, 142

Madau P., Pozzetti L., Dickinson M., 1998, ApJ, 498, 106

Nataf D. M. et al., 2013, ApJ, 769, 88

Nishiyama S., Tamura M., Hatano H., Kato D., Tanabé T., Sugitani K., Nagata T., 2009, ApJ, 696, 1407

Page M. et al., 2015, ArXiv e-prints

Panuzzo P., Granato G. L., Buat V., Inoue A. K., Silva L., Iglesias-Páramo J., Bressan A., 2007, MNRAS, 375, 640

Pei Y. C., 1992, ApJ, 395, 130

Pérez-González P. G. et al., 2013, ApJ, 762, 46

Pickles A. J., 1998, VizieR Online Data Catalog, 611, 863

Poole T. S. et al., 2008, MNRAS, 383, 627

Rieke G. H., Loken K., Rieke M. J., Tamblyn P., 1993, ApJ, 412, 99

Rodríguez-Merino L. H., Rosa-González D., Mayya Y. D., 2011, ApJ, 726, 51

Roming P. W. A. et al., 2005, Space Sci. Rev., 120, 95

Salpeter E. E., 1955, ApJ, 121, 161

Schlafly E. F., Finkbeiner D. P., 2011, ApJ, 737, 103

Schlegel D. J., Finkbeiner D. P., Davis M., 1998, ApJ, 500, 525

Schmidt M., 1959, ApJ, 129, 243

Schultz G. V., Wiemer W., 1975, A&A, 43, 133

Stecher T. P., 1965, ApJ, 142, 1683

Stecher T. P., 1969, ApJL, 157, L125

Steinmetz M., Navarro J. F., 2002, New A, 7, 155

Strickland D. K., Heckman T. M., Colbert E. J. M., Hoopes C. G., Weaver K. A., 2004, ApJ, 606, 829

Strutt J. W., 1871, Nature, 4, 142

Telesco C. M., Joy M., Dietz K., Decher R., Campins H., 1991, ApJ, 369, 135

Toomre A., Toomre J., 1972, ApJ, 178, 623

Tremonti C. A. et al., 2004, ApJ, 613, 898

Veilleux S., Cecil G., Bland-Hawthorn J., 2005, ARA&A, 43, 769

Witt A. N., Gordon K. D., 2000, ApJ, 528, 799

Yun M. S., Ho P. T. P., Lo K. Y., 1994, Nature, 372, 530